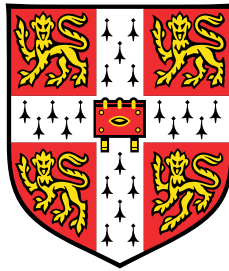


# Magnetotransport Effects in Three Dimensional Nanocircuits



**Fanfan Meng**

Department of Physics  
University of Cambridge

This dissertation is submitted for the degree of  
*Doctor of Philosophy*

Downing College

September 2021





## **Declaration**

I hereby declare that except where specific reference is made to the work of others, the contents of this dissertation are original and have not been submitted in whole or in part for consideration for any other degree or qualification in this, or any other university. This dissertation is my own work and contains nothing which is the outcome of work done in collaboration with others, except as specified in the text and Acknowledgements. This dissertation contains fewer than 65,000 words including appendices, bibliography, footnotes, tables and equations and has fewer than 150 figures.

Fanfan Meng  
September 2021



# **Magnetotransport Effects in Three Dimensional Nanocircuits**

Fanfan Meng

Extending spintronics to the third dimension is regarded as one of the promising alternatives to meet the ever increasing demands for new functionalities and more energy-efficient computing technologies. In comparison to 2D computing devices, 3D structures can not only offer higher density and better device connectivity, leading to proposals such as using 3D racetracks for high density memory, but also provide access to 3D geometrical effects such as chirality and curvature, which may lead to new physics. However, significant advances in both the fabrication of 3D spintronic devices and our fundamental understanding of the influence of 3D geometries on magnetotransport which is known as the first generation of spintronics, are required before we can fully realise the promise of 3D spintronics.

In this thesis, we present new fabrication methods for the realisation of two types of 3D nanomagnetic circuits. The first one directly integrates a complicated 3D ferromagnetic cobalt nanostructure into a circuit by employing recent developments in a 3D nanoprinting technique (Focused electron beam induced deposition), allowing exploration of complex 3D geometrical effects on magnetotransport signals. The second one incorporates multi-layered magnetic thin film materials on top of 3D non-magnetic nanostructures via physical vapour deposition, paving the path for the use of high-quality spintronic materials in 3D devices.

After these key advances in nanofabrication, we experimentally studied the magnetotransport properties of these systems under external fields applied along multiple directions, in order to understand the underlying spin states present in these systems as well as the magnetotransport signals they generate. These were complemented with several computational tools to interpret the complex magnetotransport signals measured from 3D structures. We discovered that the three dimensionality directly affects the magnetotransport signals in several ways, including deviations from the usual angular dependence of well-known effects. Specifically, we observed an angular dependent magnon magnetoresistance which had not been reported so far in planar systems. We also observed key features in magnetoelectrical signals during magnetisation reversal that originated from curling magnetic configurations that are characteristic of 3D structures. The fabrication and characterisation methodologies developed are easily adaptable to other geometries and materials, and these findings mark the first step towards exploring new spintronic effects emerging in three dimensions and in the long run, the realisation of 3D devices.



I would like to dedicate this thesis to my loving parents Shenmei Wang and Qingge Meng



## Acknowledgements

First and foremost, I would like to thank my supervisor, Dr. Amalio Fernandez Pacheco, for giving me the opportunity to begin a new adventure as a PhD student, to carry out exciting work on 3D nanomagnets, and most importantly, to enjoy doing research. I will always be grateful for all of your support and advice, not only with my research but also with my personal growth. I would also like to thank Dr Claire Donnelly, for her daily guidance on the development of the research work, writing and presentation training, as well as her warm encouragement throughout my PhD, especially during the difficult time of the pandemic lockdown. I would like to thank both of my supervisors again for their patient guidance, enthusiastic encouragement, helpful critiques, and passion for research, which have enabled me to complete this project while also preparing me to explore further as a researcher.

I would like to express my great gratitude to Prof. Russell P. Cowburn, Prof. Stuart Holmes, and Prof. Crispin H. W. Barnes for kindly providing me with the experimental resources needed to complete this work. I am also grateful to all of our group members for fostering such a pleasant working atmosphere and close collaboration. Many thanks to Luka, Delalo, Alex, Preeti, Aurelio, John, and Miguel for your help and incredible contributions during the exciting weekly group meetings that took place almost every Monday over the past four years. Thanks also to Jung-wei, Emma, Lucy, Zhuocong, Peter, and Jieyi for your patience in teaching me how to use various pieces of equipment. I would also like to extend my thanks to all the staff at the Wolfson Electron Microscopy Suite, the Kelvin Nanocharacterisation Centre, and the Cambridge Nanoscience Centre for the technical support. I also appreciate the advice from Dr. Claas Abert and Dr. Dieter Suess in micromagnetic simulations. I would also like to thank my labmates Jake, Holly, Mike, Tarun, and Jeroen for the fascinating stories you shared at lunchtime, as well as the dairy, gluten, and nut free cakes we had together. Thanks for being around and making Cavendish feel enjoyable.

I am grateful to China Scholarship Council for funding my PhD for the first three years, as well as Downing College, Ultra-precision Centre for Doctoral Training, Cambridge Philosophical Society, IEEE Magnetics Society, and Dr Claire Donnelly for providing additional

support during the final year of my PhD and for completing the writing of this thesis.

Last but not the least, a special thank you is reserved for Zhuocong, my best friend, whose company has kept life in Cambridge bright for the past few years. I can not thank my parents enough for their unwavering love and support for me to explore all the different things I want to try.



# Table of contents

<b>List of figures</b>	<b>xiii</b>
<b>Nomenclature</b>	<b>xxi</b>
<b>1 Introduction</b>	<b>3</b>
<b>2 Introductory Methods</b>	<b>11</b>
2.1 Ferromagnetism in nanomagnets . . . . .	11
2.1.1 The origin of ferromagnetism . . . . .	11
2.1.2 Energetics of a ferromagnet . . . . .	12
2.1.3 Magnetic domains and domain walls . . . . .	14
2.1.4 Magnetic simulations . . . . .	16
2.2 Magnetotransport effects . . . . .	19
2.2.1 Anisotropic magnetoresistance . . . . .	20
2.2.2 Anomalous Hall effect . . . . .	21
2.2.3 Magnon magnetoresistance . . . . .	22
2.3 Experimental methods . . . . .	25
2.3.1 Focused electron beam induced deposition . . . . .	25
2.3.2 Magnetotransport measurements . . . . .	28
2.3.3 MOKE Magnetometry . . . . .	31
<b>3 Magnetotransport Properties of a 3D Cobalt Nanobridge under High Magnetic Fields</b>	<b>35</b>
3.1 Direct fabrication of a 3D nanomagnetic circuit . . . . .	39
3.1.1 Design of the geometry to be studied . . . . .	39
3.1.2 Fabrication process . . . . .	40
3.2 Magnetotransport (MT) measurements . . . . .	48
3.3 Quantitative understanding of magnetotransport results at high fields . . . . .	52
3.3.1 Multi-macrospin approximation . . . . .	54

3.3.2	MT signals simulation using finite element method . . . . .	59
3.3.3	Interpretation of magnetotransport measurements at high fields . . .	62
3.4	Chapter Summary . . . . .	68
<b>4</b>	<b>Magnetisation reversal processes in a 3D cobalt nanobridge</b>	<b>69</b>
4.1	Magnetisation reversal process in $x$ -direction . . . . .	71
4.1.1	Analysis of the experimental MT hysteresis loops . . . . .	72
4.1.2	Micromagnetic and finite element modelling . . . . .	77
4.2	Magnetisation reversal process in $z$ -direction . . . . .	85
4.2.1	Analysis of the experiment MT loops . . . . .	87
4.3	Chapter Summary . . . . .	91
<b>5</b>	<b>3D Nanomagnetic Systems with Multilayered Materials</b>	<b>93</b>
5.1	3D nano-ramp with multilayered materials . . . . .	96
5.1.1	Sample fabrication . . . . .	96
5.1.2	Dark-field MOKE setup and the corresponding characterisation methodology . . . . .	97
5.2	3D nanomagnetic circuit with multilayered materials . . . . .	100
5.2.1	Fabrication process . . . . .	101
5.2.2	Electrical insulation verification of the FIB milled trench and the non-magnetic 3D scaffold. . . . .	106
5.2.3	Magnetotransport characterisation of the 3D device . . . . .	108
5.3	Chapter Summary . . . . .	116
<b>6</b>	<b>Conclusions and Outlook</b>	<b>117</b>
	<b>References</b>	<b>121</b>

# List of figures

1.1	<i>(a) Vertical magnetic racetrack memory in which information is encoded in domain walls and can be moved and stored in the vertical direction. (b) Interconnected nanowire network for the realisation of 3D spin ice systems. Figures are reproduced from [18] and [19], respectively under CC4 Attribution licenses. . . . .</i>	4
1.2	<i>Examples of 3D nanomagnetic circuits that have been realised. (a) Fast current-driven domain wall velocities observed in cylindrical nanowires. (b) Chiral anisotropic magnetoresistance observed in single helices. (c) A compact MR sensor based on roll-up nanomembranes. Figures are reproduced from [26], [44] and [35], respectively under CC4 Attribution licenses. . . . .</i>	7
2.1	<i>(a) Schematic representation of a magnetic wire with two domains pointing in opposite directions (red and blue arrows) and a domain wall (dotted line). (b) Top view of the magnetic texture of a transverse DW and (c) a vortex DW. Figure is reproduced from [51] under CC4 Attribution licenses. . . . .</i>	15
2.2	<i>(a) Schematic of a transverse-vortex wall (TVW). (b) Schematic of a Bloch-point wall (BPW). Figure is reproduced from [50] under CC4 Attribution licenses. . . . .</i>	15
2.3	<i>Two types of magnetic simulations used in this thesis. (a) Micromagnetic simulation. (b) Macrospin simulation. . . . .</i>	16
2.4	<i><b>Anisotropic magnetoresistance:</b> variation in resistance induced by different degrees of scattering of spin-orbit coupled carriers. Figure is reproduced from [61]. . . . .</i>	20
2.5	<i><b>Anomalous Hall effect:</b> electrons with opposite spins are deflected in different directions due to the spin-orbit coupling mediated scattering mechanisms. Figure is reproduced from [61]. . . . .</i>	22

2.6	<b>Magnon magnetoresistance:</b> <i>reduced resistance due to the suppression of spin waves by an applied magnetic field.</i> Figures are reproduced from [61].	23
2.7	(a) <i>A schematic FEBID process: precursor molecules adsorb, desorb, and diffuse at the surface and are dissociated under electron beam irradiation.</i> Figure is reproduced from [77] under CC4 Attribution licenses. (b) <i>View of a SEM chamber, with the position of electron beam, ion beam and GIS shown.</i>	26
2.8	<i>Chemical structures of the two metal-organic gases used in this thesis. (a) <math>\text{Co}_2(\text{CO})_8</math>. (b) <math>(\text{CH}_3)_3\text{Pt}(\text{CpCH}_3)</math>.</i> Figure is reproduced from [74] under CC4 Attribution licenses.	27
2.9	<i>Picture of Magnetotransport measurement setup used. The positions of the sample probe, sample holder and electromagnets are labelled.</i>	29
2.10	<i>Schematic of the magnetotransport measurement setup, illustrating the scheme of the lock-in detection technique.</i>	30
2.11	<i>Schematic diagram of MOKE measurement geometries for p-polarised incident light.</i> Figure is reproduced from [85] under CC4 Attribution licenses.	31
2.12	<i>Schematic of the MOKE + MT setup used in this thesis to simultaneously measure magnetotransport and optical signals of samples</i>	32
2.13	(a) <i>A chip carrier socket wired to a connector box.</i> (b) <i>A sample placed at the centre of quadrupole magnets and electrical measurement setup.</i> (c) <i>Picture of the MOKE setup.</i>	33
3.1	<i>A rendering of the CAD design of the nanobridge investigated in the experiment. Reproduced from [61].</i>	40
3.2	<i>Direct integration of a ferromagnetic 3D nanobridge in a microelectronic circuit. (a) preparation of a clean silicon dioxide substrate. (b) patterning of electrical contacts. (c) milling of trenches by focused ion beam. (d) 3D-nanoprinting of the bridge via focused electron beam induced deposition. (e) Four-probe magneto-transport measurement configuration, where the voltage across the pink region is measured. Reproduced from [61].</i>	41
3.3	<i>Electrical contacts. (a) Large electrical contacts for wire bonding. (b) Small electrical contacts for connecting the 3D nanobridge. The 3D nanobridge is deposited within the blue square.</i>	42
3.4	<i>FIB milling. (a) The size of the halo is estimated for the bridge to be deposited. (b) Lengths of the FIB milled trenches (c) FIB cleaning of the contacts</i>	43

3.5	Workflow of the algorithm to deposit a 3D nanobridge by FEBID. (a) Calibration of growth rate. (b) Geometry importation to the algorithm. (c) Generation of beam position and dwell time from the algorithm. . . . .	44
3.6	Correction for gas flux anisotropy. (a) Position of the gas injection system (GIS). Red arrows mark the direction of precursor flux. (b) Bridge built without gas anisotropy correction (c) Red circle: normalised scaling factor with respect to the direction of GIS ( $\phi_0 = 45^\circ, \alpha = 0.05$ ), Blue circle: unit circle for comparison. (d) Bridge built with gas anisotropy correction. . . .	45
3.7	SEM images of a resulting nanomagnetic circuit. (a) Side view of the fabricated nanomagnetic circuit. Image tilt of $45^\circ$ . (b) Top view of the fabricated nanomagnetic circuit. (c) Top view of a broken bridge fabricated under the same conditions. Reproduced from [61]. . . . .	47
3.8	Magnetotransport measurements. (a) Four-probe magnetotransport measurement configuration, where the region between sidelegs was probed. (b) The simulation of the current density in the probed region of the 3D nanobridge with the colour indicating the z component of the current density. (c) Magnetoelectrical signals expected in a ferromagnetic structure and their field symmetries and angular dependencies [60]. . . . .	48
3.9	Magnetotransport measurements. (a) The schematic shows how the field is applied relative to the 3D nanobridge, $\theta$ is the angle between the applied field and the substrate. (b) MT hysteresis loops obtained from -4 T to 4 T and 4 T to -4 T for each field angle $\theta$ from $0^\circ$ to $90^\circ$ . (c) Odd-in-field signal, $R_{odd}$ . (d) Even-in-field signal, $R_{even}$ . Reproduced from [61]. . . . .	49
3.10	The setup of the MT simulation tool. (a) The probed region of the structure is considered to be made up three independent nanowires. (b) Multi-macrospin model made up with three single-domain nanowires. (c) The FEM mesh of the bridge used to simulate MT signals. Reproduced from [61]. . . . .	52
3.11	Macrospin model. The applied field $\vec{H}_a$ , the demagnetising field $\vec{H}_d$ and the effective field $\vec{H}$ are considered for a nanowire in the local coordinate system.	54
3.12	Magnum.fe simulations of the demagnetising field $\vec{H}_d$ for $\vec{H}_a$ applied in different directions. (a) The grey arrows indicate the direction of $\vec{H}_d$ (note that the lengths of the arrows do not represent the magnitude of the demagnetising field) and the blue-red colour scale indicates the x-component of the $\vec{H}_d$ . (b)-(d) The averaged magnitude of $\vec{H}_d$ , from the simulation for the three sections marked in <b>Figure 3.10</b> . . . . .	56

3.13	<i>Comparison of the averaged x, y, z components of the demagnetising field, <math>\vec{H}_d</math>, obtained from macrospin and micromagnetic simulations in (a) Section 1 (b) Section 2 (c) Section 3. For each section, the demagnetising field of micromagnetic simulations is given in red and used to identify the optimal demagnetising factor for the structure. . . . .</i>	58
3.14	<i>FEM simulation. (a) Boundary conditions. (b) Simulated electric potential distribution with a conductive layer underneath the bridge. (c) Simulated electric potential distribution for the bridge only. . . . .</i>	60
3.15	<i>(a) Comparison between the angular dependence of the odd part data and the AHE and OHE simulation. (b) Averaged magnetisation vectors, <math>\vec{m}_1(\theta)</math>, <math>\vec{m}_2(\theta)</math> and <math>\vec{m}_3(\theta)</math> for three sections for <math>\theta = 0^\circ</math> and <math>\theta = 90^\circ</math> and their components on the current normal directions. Reproduced from [61] . . .</i>	62
3.16	<i>Arrangements of voltage probes in different situations (a) 2D wire (b) 2D v-shape (c) 3D v-shape . . . . .</i>	63
3.17	<i>(a) Comparison between the angular dependence of the even part of the data and the AMR simulation. (b) Averaged magnetisation vectors, <math>\vec{m}_1(\theta)</math>, <math>\vec{m}_2(\theta)</math> and <math>\vec{m}_3(\theta)</math> for three sections at <math>\theta = 0^\circ</math> and <math>\theta = 90^\circ</math> and their components on the current direction. Reproduced from [61]. . . . .</i>	64
3.18	<i>(a) Simulation of the AMR and MMR effects (b) Applied field, <math>\vec{H}_a</math>, demagnetising field, <math>\vec{H}_d</math> and their vector sum <math>\vec{H}</math> for each section of the bridge. Reproduced from [61]. . . . .</i>	66
3.19	<i>Comparison between the sum of AMR and MMR simulations and the even data. Reproduced from [61]. . . . .</i>	67
4.1	<i>Schematic of applied field configuration with respect to the 3D nanobridge. Field is applied in the positive x-direction. . . . .</i>	71
4.2	<i>Magnetoresistance hysteresis loop (16 averages) for field applied in x-direction. (a) Full hysteresis loop between -2.5 T and 2.5 T (b) Zoom-in region between -0.1 T to +0.1 T. The right y-axis plots the relative change of resistance with respect to the maximum. . . . .</i>	72
4.3	<i>All 16 MT loops measured for field applied in the x-direction. The thicker line represents the average of the 16 cycles. (a) Forward sweeps. (b) Backward sweeps. . . . .</i>	74

4.4	<i>Analysis of different switching events for all 16 cycles. The left column are plots for forward sweeps (between +0.05 and -0.1 T) and the right column are plots for backward sweeps (between -0.05 and +0.1 T). (a)-(b) Two switching events are defined. (c)-(d) Distribution of switching fields of both events. Bin width = 1 mT, which is the precision of measurement for the applied field. (e)-(f) Distribution of the resistance change in both events. Bin width = 0.5 m<math>\Omega</math> (error in resistance measurement = <math>\pm 0.25</math> m<math>\Omega</math>). . . . .</i>	75
4.5	<i>Summary of the switching field and change of resistance for event 1 and 2. .</i>	76
4.6	<i>(a) Finite difference mesh used for micromagnetic simulation. (b) FEM mesh used to simulate MT signals. . . . .</i>	77
4.7	<i>Experiment and simulated MT results. The left column plots results for the full - 2.5 T to + 2.5 T field range. The right column plots a smaller range of fields near 0 T. (a) The experimental MT hysteresis loops. (b) The simulated MT hysteresis loops that considers all effects including AMR, AHE, and MMR. (c) The simulated contribution from different effects. . . . .</i>	80
4.8	<i>The simulated magnetic configurations of the states of interest. The arrows represent the direction of magnetisation and the colour represents the <math>m_z</math>. (a) The front view of the magnetisation states. (b) XY-cross-sectional view of the magnetic configurations. (c) XZ-cross-sectional view of the magnetic configurations. (d) YZ-cross-sectional view of the magnetic configurations. .</i>	81
4.9	<i>The global vortex state found in a Co nanowire. The image is reproduced from [121] under CC4 Attribution licenses. . . . .</i>	83
4.10	<i>Schematic of the applied field configuration with respect to the 3D nanobridge. Field is applied in the positive z-direction. . . . .</i>	85
4.11	<i>The average of 16 MT hysteresis loops for field applied in z-direction. (a) The full hysteresis loop between -2.5 T to 2.5 T. (b) Zoom-in region between -0.3 T to and 0.3 T. . . . .</i>	85
4.12	<i>An overview of all 16 <math>B_z</math> hysteresis loops in the range between <math>\pm 0.3</math> T. Two switching modes are identified for both (a)-(b) Forward sweeps and (c)-(d) Backward sweeps. The thicker line represents the average of each mode. The number of times each type of mode is observed with respect to the total 16 loops is included in brackets. . . . .</i>	86
4.13	<i>Comparison between the two switching modes for the forward sweeps. (a)-(b) Mode 1 in <math>\pm 2.5</math> T and <math>\pm 0.3</math> T range, respectively. (c)-(d) Mode 2 in <math>\pm 2.5</math> T and <math>\pm 0.3</math> T range, respectively. (e) Proposed states for mode 1. (f) Proposed states for mode 2. . . . .</i>	88

4.14	<i>The comparison between the two switching modes in the backward sweeps. (a)-(b) Mode 1 in <math>\pm 2.5</math> T and <math>\pm 0.3</math> T range, respectively. (c)-(d) Mode 2 in <math>\pm 2.5</math> T and <math>\pm 0.3</math> T range, respectively. . . . .</i>	90
5.1	<i>Sample fabrication. (a) A non-magnetic scaffold is 3D printed using FEBID, with its composition being a carbon-rich amorphous mixture of carbon and platinum [80]. (b) Magnetic multilayered thin films is sputtered onto the scaffold. For simplicity, only one layer is shown. . . . .</i>	96
5.2	<i>(a) Dark-field MOKE setup (b) Magnetic field configuration. The applied field (0 and <math>\pi</math> phase is shown in pink) consists of a low-frequency oscillating field along the x-axis, combined with a constant z-offset normal to it. The projections of the applied field on the nanoramp and substrate are shown in orange and green, respectively. . . . .</i>	97
5.3	<i>(a) SEM image of a nanomagnetic ramp after sputtering Ta/CoFeB/Ta (2/10/2 nm). The projection of applied field on the 3D nanoramp and the 2D thin film are labelled in orange and green respectively. (b) The schematic of magnetic materials used. (c) Subset of hysteresis loops for the 3D ramp (orange) and the 2D film (green) at different <math>H_z</math> offsets. (d) (<math>H_x</math>, <math>H_z</math>) diagram of switching fields for the nanoramp (orange) and the 2D film (green). . . .</i>	98
5.4	<i>Creating a 3D nanomagnetic circuit using the combination of a scaffold and PVD. (a) Create a non-magnetic scaffold. (b) Incorporate magnetic materials using PVD, magnetic thin films deposited will shunt current from the 3D structure. (c) The ideal 3D nanomagnetic circuit created using 'scaffold + PVD' method. Reproduced from [129]. . . . .</i>	100
5.5	<i>Fabrication process. (a) Preparation of a clean silicon substrate with 300 nm thermally oxidised silicon dioxide. (b) Patterning of Au contacts using optical-lithography and sputtering. (c) Milling of a trench between two contacts using focused ion beam. (d) Spin-coating and patterning of the double-layered resist. (e) FEBID 3D Pt-C scaffold (f) Sputter multilayered materials. (g) Lift-off resist. Reproduced from [129]. . . . .</i>	101
5.6	<i>The consequence of using FIB milling after the deposition of resist. (a) SEM image taken after FIB milling with resist around. (b) Optical microscopy image taken after metallisation: the region irradiated by FIB cannot be lifted off. . . . .</i>	102



5.7	<i>Comparison between using single- and double- layer resist. (a) Schematics of using single layer resist. (b)-(c) SEM images taken before and after metallisation when using single layer resist. (d) Schematics of using double-layer resist. (e)-(f) SEM images taken before and after metallisation when using double-layer resist. . . . .</i>	103
5.8	<i>FEBID process. (a) SEM image of the printed Pt-C scaffold (stage tilt at 30°). Inset is the CAD design of the bridge. (b) Top view of the printed Pt-C bridge. . . . .</i>	104
5.9	<i>3D nanomagnetic circuit. (a) Side view of the printed 3D nanomagnetic circuit (stage tilt equals to 30°). (b) Top view zoom-out of the printed 3D nanomagnetic circuit, showing the electrical pads, microwire bonds, and area (red square) where the bridge was fabricated. Current (<math>I^+</math>), ground (G) and voltage (V) pads for magnetotransport measurements are indicated. . .</i>	105
5.10	<i>Electrical insulation verification of the trench. (a) An optical microscopy image of the FIB test device (without 3D bridge). (b) I-V curve measured across the FIB milled trench. . . . .</i>	106
5.11	<i>Electrical insulation verification of the Pt-C scaffold. (a) I-V curves of 3 voltage sweeps applied across the Pt-C scaffold. (b) Differential resistivity calculated from the first sweep. (c)-(d) SEM images taken before and after applying a 10V voltage sweep. . . . .</i>	107
5.12	<i>(a) The schematic that shows the MOKE and MT measurement positions. (b) The schematic of the cross-section of the 3D device. . . . .</i>	108
5.13	<i>2D track section: (a) Normalised transverse Kerr (proportional to <math>M_y</math>). Error=<math>\pm 0.03</math>. (b) Normalised longitudinal Kerr (proportional to <math>M_y</math>). Error=<math>\pm 0.12</math>. (c)-(d) <math>M_y/M_s</math> and <math>M_x/M_s</math> results from Mumax3 simulation. . . . .</i>	109
5.14	<i>Magnetotransport results of the 2D track section. (a) Magnetoresistance measured across the 2D track section (V2-V1). Error=<math>\pm 2 \text{ m}\Omega</math>. (b) The simulated MT result based on the combination of Mumax3 and FEM simulation. (c) The FEM mesh used for the 2D track section. . . . .</i>	111

5.15	<i>3D bridge section: magnetotransport results and simulations. (a) Resistance measured across the 3D section (V3-V2). (b) FEM model of the 3D section that consists: 2D track, 3D bridge and 2D to 3D transition region. (c) Three magnetization states from the micromagnetic simulation for the combination of the 3D bridge and the transition region (<math>M_x/M_s</math> is plotted). (d) Simulation result of <math>M_x/M_s</math> for the nanowire section. (e) Simulation result of <math>M_x/M_s</math> for the transition section. (f) Simulated MT result based on the combination of Mumax3 and FEM simulation. . . . .</i>	113
5.16	<i>The SEM image of the 3D nanomagnet created where the imperfections caused by Pt-C are shown in white circles. . . . .</i>	114

# Nomenclature

## Acronyms / Abbreviations

2D	Two-dimensional
AC	Alternating current
AMR	Anisotropic magnetoresistance
CMOS	Complementary metal-oxide-semiconductor
DC	Direct current
DW	Domain wall
FDM	Finite difference method
FEED	Focused Electron Beam Induced Deposition
FEM	Finite element method
FIB	Focused Ion Beam
GIS	Gas injection system
GMR	Giant magnetoresistance
HDD	Hard disk drive
LLG	Landau-Lifshitz-Gilbert
MMR	Magnon magnetoresistance
MOKE	Magneto-optical Kerr effect
MR	Magnetoresistance

MRAM Magnetic Random Access Memory

MT Magnetotransport

PHE Planar Hall effect

PVD Physical vapour deposition

SEM Scanning electron microscopy

SOT Spin orbit torque

SRAM Static Random Access Memory

STT Spin transfer torque

TMR Tunnelling magnetoresistance

# Publications and International Conference Presentations

## First-author publications:

Fanfan Meng, Claire Donnelly, Class Abert, Luka Skoric, Stuart Holmes, Zhuocong Xiao, Jung-Wei Liao, Peter J. Newton, Crispin H.W. Barnes, Dédalo Sanz-Hernandez, Aurelio Hierro-Rodriguez, Dieter Suess, Russell P. Cowburn, and Amalio Fernández-Pacheco. (2021). Non-planar geometrical effects on the magnetoelectrical signal in a three-dimensional nano-magnetic circuit. *ACS nano*, 15(4), 6765-6773.

Fanfan Meng, Claire Donnelly, Luka Skoric, Aurelio Hierro-Rodriguez, Jung-Wei Liao, Amalio Fernández-Pacheco. (2021). Fabrication of a 3D Nanomagnetic Circuit with Multi-Layered Materials for Applications in Spintronics. *Micromachines*, 12(8), 859.

## Other publication:

Luka Skoric, Dédalo Sanz-Hernandez, Fanfan Meng, Claire Donnelly, Sara Merino-Aceituno, Amalio Fernández-Pacheco. (2019). Layer-by-layer growth of complex-shaped three-dimensional nanostructures with focused electron beams. *Nano letters*, 20(1), 184-191.

## Conference presentations:

Non-planar geometrical effects on the magnetoelectrical signal in a 3D nanomagnetic circuit. (JI-05) *INTERMAG* (2021). **Best Student Presentation Award.**

Creating 3D nanomagnetic circuits for spintronic applications. (R1-13) *Magnetism and Magnetic Materials (MMM)* (2020).



# Chapter 1

## Introduction

The fundamental study and exploitation of phenomena concerning the interplay between magnetism and electrical transport, especially in two dimensional (2D) magnetic nanostructures, have been instrumental in the digital revolution [1]. In 1991, anisotropic magnetoresistance (AMR), first discovered in ferromagnets by Lord Kelvin in 1857 [2], was used in hard disk drives (HDDs), allowing ferromagnetic thin films to replace electromagnets as reading components, and marked the beginning of a period of rapid increase in data storage density [3]. Giant magnetoresistance (GMR), discovered in artificial multilayered materials in 1988 [4, 5], replaced AMR heads in 1997 for its higher sensitivity and immediately doubled the storage density of HDDs every year. The decade since the first use of MR read heads (1992-2002), HDDs' storage density increased by roughly 400 times with a nearly 1000 times decrease in the cost per bit [6, 7]. This successful case of GMR transitioning fundamental science into impactful applications was awarded with the 2007 Nobel Prize in physics to Albert Fert and Peter Grünberg and kick-started the extensive research in 2D magnetic nanostructures, which is known as the field of nanomagnetism and spintronics [8].

Building upon the success in long-term data retention, there have been increased efforts to incorporate magnetic nanostructures not only in the storing but also towards the processing of information [8]. This shift is driven by the challenge of increasing power dissipation in electronic circuits due to leakage currents while scaling down the CMOS devices [9]. Unlike purely charge-based systems, information encoded in magnetisation states is generally nonvolatile, thus, reducing the power requirement for maintaining data [10]. This advantage is demonstrated by the commercialisation of nonvolatile magnetic random access memories (MRAMs) based on the discoveries of spin-transfer-torque (STT), spin-orbit-torque (SOT) and giant tunnelling magnetoresistance (TMR), which are used as a replacement of static RAM (SRAMs) [8, 11]. In addition to magnetic memory devices, there are numerous

spintronic concepts for realising digital Boolean logic functions that have been proposed based on dipolar interactions between nanomagnets [12], interaction between domain walls [13], interference of spin waves [14], *etc.* Beyond Boolean logic, fundamental research in spintronics is also exploring unconventional computing schemes such as neuromorphic computation using spin waves [15] or reservoir computing based on domain wall networks [16]. Although these advances have promised to reduce power dissipation to some extent, they have a major limitation that the operation of magnetic configurations is confined to 2D patterned planar single- or multilayered materials, hence their functionalities are intrinsically 2D. For spintronic devices to meet the ever-increasing demands for high-speed, high-density, and low power electronic components, one of the most promising future is to expand spintronics into three dimensions, where magnetic information could be transmitted, stored, processed in a more flexible and capable 3D space [17].

### Motivations for spintronics to go 3D

Three dimensional magnetic nanostructure could offer a number of advantages, the first noticeable of which is the increase in the density of storable information due to vertical stacking. Based on this benefit, there have been proposals for ultrahigh density, high-performance memory and logic devices such as the 3D magnetic racetrack memory (**Figure 1.1 a**) [18] and the magnetic ratchet [20] in which information is encoded in magnetic objects (such as

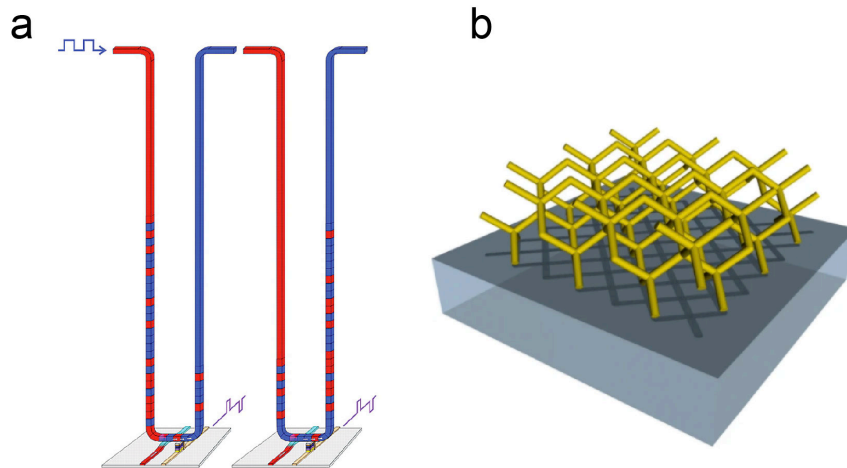


Fig. 1.1 **(a)** Vertical magnetic racetrack memory in which information is encoded in domain walls and can be moved and stored in the vertical direction. **(b)** Interconnected nanowire network for the realisation of 3D spin ice systems. Figures are reproduced from [18] and [19], respectively under CC4 Attribution licenses.



domain walls and solitons) and can be moved and stored out of the substrate plane.

Since 3D structures can be extended with an extra degree of freedom, in addition to the enhanced density, they also provide better device connectivity. One of the biggest obstacles preventing the realisation of a full spintronic computer is that magnetic information (domain walls or spin waves) can not be transferred between different planes as easily as charge signals do. As a result, the cascading and fan-out of logic gates, as well as the connection between logic and memory modules, require intermediate conversion to charge signals, resulting in a power consumption that outweighs the energy savings from using a magnetic system [8]. Hence, the development of magnetic interconnects based on 3D nanostructures that allows the use of magnetic signals exclusively will have a huge impact on the realisation of the all-spin computing hierarchy [10]. Moreover, 3D integration is also critical for the development of systems that go beyond conventional Boolean logic such as neuromorphic computing architectures in which 3D networks of magnetic nanowires (**Figure 1.1 b**) can mimic neurons and synapses in brains [19, 21].

As well as offering exciting prospects for devices with enhanced density and connectivity, the introduction of 3D geometrical effects such as curvature, chirality and topology opens the door to new magnetic phenomena [17, 22, 23]. These include predictions and observations of new spin textures [24, 25], exotic dynamic behaviours [26–28], as well as curvature-induced effects [23, 29, 30]. For example, a domain wall which contains a magnetic singularity (Bloch point) has been observed in cylindrical nanowires [24], nonreciprocal spin wave propagation has been observed in rolled-up nanomembranes [27], while magnetic chiral spin textures have been realised in double helices [31]. When the new physics discovered in 3D nanomagnets is combined with spintronics, there is a huge potential for new functionalities [17].

### **Current status of the research in 3D nanomagnetic circuits**

Creating 3D nanomagnets, as the first step towards the research in 3D spintronics, however, is not trivial. So far, 3D magnetic nanostructures used for experimental studies have been mainly achieved in four routes [17]. We first provide an overview of these four routes, including their benefits and drawbacks and then discuss their integratability with electronic circuits.

The first route uses a combination of 3D templates and chemical synthesis techniques such as electroplating, electroless deposition and atomic layer deposition. Anodised alumina

matrices are the most common templates, producing arrays of high-aspect ratio cylindrical nanowires [24, 26] that have led to the observation of new magnetic textures such as Bloch point domain walls [24]. Truly 3D templates can be achieved via different methods such as block-copolymers [32, 33]. In this way, 3D magnetic gyroid lattices have been realised, allowing for long-range ordered systems [33]. Although well suited to the fabrication of extended 3D nanoscale systems, the templates used limit the choices of geometries, and the lack of control over the thickness of the ferromagnetic films grown via chemical synthesis methods hinders the inclusion of functional interfaces [17]. The second route is to roll up planar thin films through strain engineering, which combines well-established top-down and bottom up techniques to fabricate nanotubes of almost arbitrary material combination with similar film and interface qualities as of planar architectures [25, 34, 35]. This method is commonly used in X-ray microscopy studies to retrieve spin textures in curved magnetic thin films [25]. Compared to the chemical synthesis route, this method could offer significantly better materials quality but is limited to only tubular geometries with diameters typically above 1  $\mu\text{m}$ . The third route employs a 3D nano-printing technique [36], known as focused electron beam induced deposition (FEBID), which allows prototyping of individual complex 3D structures [37], with tens of nanometre resolution made of polycrystalline or amorphous cobalt [38], iron or cobalt-iron alloys [39, 40]. Artificial double-helices which provide controlled magnetic chirality have been realised using this method [31]. This route provides significantly more flexibility in the choice of geometry; however, it is limited by the range of materials and cannot be used to create high quality materials and interfaces directly [36]. The last route involves the use of physical vapour deposition (PVD) on top of previously patterned non-magnetic 3D scaffolds. These scaffolds can be created in various ways including two-photon optical lithography [41, 19], self-assembly [42] and also FEBID [43]. This route has been used in the creation of a 3D nanomagnetic domain wall conduit [43] and also the realisation of a frustrated 3D nanowire lattice [19]. This route offers more flexibility in the choice of geometries and takes advantage of PVD which could offer high quality materials with more precise control. However, challenges are faced with regard to conformal and uniform deposition.

In addition to the fabrication of 3D nanomagnets, a second challenge to the realisation of 3D spintronic devices involves their integration into microelectronic circuits. Indeed, the experimental realisation of 3D nanomagnetic circuits has so far mainly achieved with the first two routes mentioned. For example, for the chemical deposition around 3D templates, magnetotransport studies have been achieved in cylindrical nanowires [26] (**Figure 1.2 a**) and single helices [44] (**Figure 1.2 b**) in which discoveries such as fast current driven domain

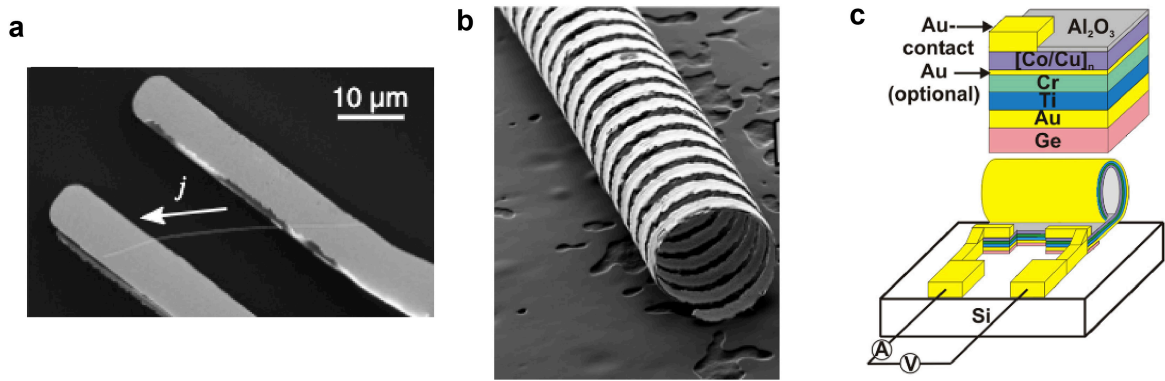


Fig. 1.2 *Examples of 3D nanomagnetic circuits that have been realised. (a) Fast current-driven domain wall velocities observed in cylindrical nanowires. (b) Chiral anisotropic magnetoresistance observed in single helices. (c) A compact MR sensor based on roll-up nanomembranes.* Figures are reproduced from [26], [44] and [35], respectively under CC4 Attribution licenses.

wall velocities and chiral anisotropic magnetoresistance have been made, respectively. To release these structures from their templates and electrically contact them into electrical circuits, sophisticated micro-manipulation methods were involved. For the second route, since the nanomembranes are first patterned using traditional top-down lithography, they generally have better on-chip integrability. For instance, a compact MR based sensor for in-flow detection of magnetic objects (**Figure 1.2 c**) has been realised using this method [34, 35]. Although prior to this report, there were no electrically-connected 3D nanomagnetic circuits implemented using the third route, the direct writing feature of 3D nanoprinting is very suitable for prototyping complex geometries directly on pre-patterned electrical contacts, on the premise that a certain degree of control in both geometries and materials is achieved for the 3D nanoprinting technique used. The last route which uses physical vapour deposition on top of non-magnetic scaffolds has not been used in the creation of 3D spintronic devices due to the fact that with standard PVD techniques, the material is deposited everywhere on a substrate, meaning without additional non-trivial fabrication steps, current is shunted from the 3D structure and instead runs through the continuous thin film deposited around it.

These first results comprising 3D nanomagnetic circuits, despite being obtained from relatively limited geometries and materials by only exploiting the first two fabrication routes, have already demonstrated the potential for new physics and technological impact of this vibrant field.

### Aim and thesis outline

In this thesis, these three main challenges are addressed: the first is the integration of 3D nanomagnets with more complicated geometries and high quality magnetic materials in microelectronic circuits; the second is the development of suitable magnetotransport characterisation strategies to electrically probe 3D structures; and finally the understanding of the complex characterisation results from 3D structures. The content of the thesis is as follows:

- **Chapter 2** presents the key theoretical and experimental tools used throughout the thesis. For the theoretical background, an introduction to the origins of ferromagnetism, the energetics of a ferromagnet and magnetic simulations is given, followed by an overview of the magnetotransport effects involved in this work. For the experimental section, we introduce focused electron beam induced deposition, a 3D nano-printing tool used in our investigation to create 3D nanomagnets with complex geometries. We also summarise the principal components of the magnetotransport and magneto-optical setups used to characterise 3D nanomagnetic circuits. The underlying theory for these techniques is also included.
- **Chapter 3** presents a general method for the integration of 3D ferromagnetic nanostructures with complex geometries into microelectronic circuits via 3D nanoprinting, exemplified by the realisation of a circuit containing a 3D cobalt nanobridge. The influence of the 3D geometry on the behaviour of intrinsic magnetotransport properties such as the anisotropic magnetoresistance and anomalous Hall effects is understood by a thorough angular dependence study as a function of high external magnetic fields, in combination with a simulation tool that combines macrospin and finite element modelling.
- **Chapter 4** investigates the magnetisation reversal processes of the same 3D cobalt nanobridge, but this time at low magnetic field values, and identifies the type of 3D spin states involved in this reversal depending on the field direction. This is done via a combination of magnetotransport measurements, and includes the stochastic analysis of the reversal processes, as well as micromagnetic and finite element modelling.
- **Chapter 5** shows the development of a fabrication process for the realisation of 3D nanomagnetic circuits that combines not only complicated geometries but also high quality multilayered materials using 3D nanoprinting, physical vapour deposition and various planar lithographic techniques. This method is applied for the creation of a 3D nanomagnetic circuit that integrates a Ta/CoFeB/Ta multilayer onto a 3D nanobridge.

The reversal processes of such a device are studied through the use of magnetotransport and magneto-optical measurements, in combination with micromagnetic and finite element modelling. The results obtained demonstrated the suitability of this approach to create this type of functional 3D devices.

- **Chapter 6** concludes this thesis with a summary of each chapter and an outlook for future works.



# Chapter 2

## Introductory Methods

### 2.1 Ferromagnetism in nanomagnets

In order to analyse 3D magnetic nanostructures and their behaviour and influence on electrical signals under applied magnetic fields, first a brief overview of some of the fundamental ideas of magnetism is provided, including the origin of magnetism, which is a quantum mechanical property of materials, as well as micromagnetics, which is based on a continuum description and deals with magnetic structures on sub-micrometer length scales by considering various energy terms in a ferromagnet. Then we show some typical magnetic configurations in magnetic nanowires that are the result of competition between different energy terms considered in micromagnetics, followed by an introduction to two types of magnetic simulations: micromagnetic and macrospin simulations that are used in this thesis to assist the understanding of magnetic configurations in both 2D and 3D nanostructures.

#### 2.1.1 The origin of ferromagnetism

Magnetism has its origin in the magnetic moment of the atoms produced by the angular momenta of their constituent electrons. Each electron contributes two types of angular momentum: an orbital momentum associated with its orbital motion around the nucleus, and a spin momentum intrinsic to its nature [45]. According to the Pauli exclusion principle and Hund's rule [45, 46], atoms with fully occupied orbitals have a net magnetic moment equal to zero as in each shell electrons are paired, *i.e.*, the opposite spins of the two electrons in the same orbital cancel out their momentum. Atoms with 'partially filled shells' have unpaired electrons, resulting in a non-zero magnetic moment and this moment is contributed mostly by the spin.

In 1928, Heisenberg proposed that two neighbouring atoms with unpaired electrons of spins  $\vec{S}_i$  and  $\vec{S}_j$  interact with an energy [46]:

$$E_{ex} = -2J_{ij} \sum_{ij} \vec{S}_i \cdot \vec{S}_j, \quad (2.1)$$

where  $J_{ij}$  is the exchange constant. If  $J_{ij} > 0$ ,  $E_{ex}$  is at minimum when the spins are parallel, resulting in ferromagnetic coupling. Since the exchange interaction is short-range, the value  $J$  is the largest for nearest-neighbour spins. This tendency to align the nearest-neighbour spins causes parallel alignment of the entire system and result in ferromagnetism [45]. The only three pure elemental ferromagnets at room temperature are the  $3d$  metals Fe, Ni and Co. If  $J_{ij} < 0$ , the lowest energy state results from antiparallel spins, resulting in antiferromagnetism. In this work, we focus on traditional ferromagnetic materials such as Co and its alloys with nanoscale dimensions.

### 2.1.2 Energetics of a ferromagnet

In a ferromagnetic system, there are several sources of energy, and the competition between these various energies is the origin of the complexity of the distributions of magnetisation. These energies will be discussed in the context of micromagnetism in this section. The quantum exchange interaction explains the origin of ferromagnetism, but not macroscopic magnetisation processes such as the characteristics of a hysteresis loop. Hence, a continuum description known as micromagnetism was developed where the magnetisation that describes the density of the magnetic moments is treated as a classical vector field,  $\vec{M} = \vec{M}(\vec{r}) = M_s \vec{m}(\vec{r})$ , that varies continuously as a function of the space variable  $\vec{r}$ , rather than a discrete spin lattice as in the quantum approach [47]. Two assumptions for this description are that the directions of neighbouring spins only change by small angles between lattice sites due to strong exchange interaction, and the norm saturation magnetisation,  $M_s$ , of the magnetisation vector is constant and uniform in any homogeneous material [45].

The configuration of the magnetisation vector field for a given situation depends on competition between different energy terms and can be obtained by the minimisation of the total energy of the system given by [45]:

$$E_{tot} = E_{ex} + E_a + E_d + E_Z, \quad (2.2)$$

where  $E_{ex}$  is due to exchange interaction,  $E_a$  due to magnetocrystalline anisotropy,  $E_d$  due to demagnetising fields,  $E_Z$  associated with the response of the materials to the application of



an external magnetic field. Other energy terms related to applied stress and magnetostriction are not considered in this work for simplicity, and our results can be explained without these additional energy contribution.

**The exchange energy** tends to keep neighbouring magnetic moments parallel to each other. The energy cost of a change in the direction of magnetisation is [45]:

$$E_{ex} = A \int_V [(\nabla m_x)^2 + (\nabla m_y)^2 + (\nabla m_z)^2] dV, \quad (2.3)$$

where  $A = A(T)$  is the temperature dependent exchange stiffness constant in (J/m) and  $\vec{m}_{x,y,z} = \vec{M}_{x,y,z}/M_s$  are the normalised magnetisation vectors in each direction. If the temperature is raised and the thermal energy per moment equals this exchange energy, the magnetic ordering is destroyed. This occurs at the Curie temperature ( $T_c$ ) which is directly related to the exchange energy as  $A(0) \approx k_B T_c / \alpha_L$  and, where  $\alpha_L$  is the lattice constant of the material.

**The magnetocrystalline anisotropy energy** describes the preference for the magnetisation to be oriented along certain crystallographic directions. The preferred directions are called the easy axes. This energy depends on the direction of the magnetisation relative to the easy axes for the material. For the case of uniaxial anisotropy [48]:

$$E_a = \int_V K_1 \sin^2(\theta) d^3r \quad (2.4)$$

with  $K_1$  is the uniaxial anisotropy constant in (J/m<sup>3</sup>) and  $\theta$  is the angle between  $\vec{m}$  and the easy axis direction.

**The demagnetising or magnetostatic energy** is a consequence of the magnetic field generated by the magnetic body itself to fulfil Gauss's law,

$$\nabla \cdot \vec{B} = 0 \quad (2.5)$$

where  $\vec{B} = \mu_0(\vec{H} + \vec{M})$ , or equivalently:

$$\nabla \cdot \vec{H} = -\nabla \cdot \vec{M} \quad (2.6)$$

In analogy with electrostatics,  $-\nabla \cdot \vec{M}$  (the sinks and sources of magnetisation) act as 'magnetic charges' for the generation of  $\vec{H}$  fields. These  $\vec{H}$  fields oppose the magnetisation inside the material and is therefore known as 'demagnetising field',  $\vec{H}_d$ . The demagnetising

energy is given by [48]:

$$E_d = -\frac{\mu_0}{2} \int_V \vec{M} \cdot \vec{H}_d dV \quad (2.7)$$

The demagnetising energy always favours systems with the lowest magnetic charges, or equivalently, magnetisation profiles where  $\vec{M}$  does not cross any surfaces and no volume gradient exists. Thus the minimisation of demagnetising energy usually induces the formation of flux-closed magnetic domain patterns that leave no magnetic charges at the surface. As this energy is dependent on the sample geometry, it is often referred as ‘shape anisotropy’. The magnetostatic energy term is important, particularly for 3D nanomagnets, as it enables us to control magnetisation configuration by exploiting different geometries, whereas other energy terms such as exchange energy and magnetocrystalline anisotropy are intrinsic to the materials.

**The Zeeman energy** is the potential energy of a magnetic moment in a field. This energy is minimised when the magnetisation of a ferromagnet aligns parallel to the applied field and is given by [45]:

$$E_z = -\mu_0 \int_V \vec{M} \cdot \vec{H}_{app} dV \quad (2.8)$$

which favours the alignment of  $\vec{M}$  along the applied external field.

### 2.1.3 Magnetic domains and domain walls

Ferromagnetic domains are small regions in ferromagnetic materials within which all the magnetic moments are aligned parallel to each other. As mentioned in the previous section, the domain forms as a result of total energy minimisation and the interfaces between domains in which the spontaneous magnetisation has different directions are known as domain walls (DWs) [45]. Over the last decade, domain walls have attracted much attention due to their ‘particle-like’ nature, which makes them ideal candidates for the transport, storage and processing of magnetic information [13, 18, 49]. The magnetisation distribution in a domain wall can be very rich and here we consider the typical types of DWs found in nanowires as examples. Magnetic nanowires are also subject to extensive investigation for their potential use as DW conduits for memory and sensing applications [50].

In the case of 2D nanowires (**Figure 2.1 a**) with negligible magnetocrystalline anisotropy, magnetic textures arising from the competition between exchange energy and demagnetising energy are predicted to be transverse walls (**Figure 2.1 b**) or vortex walls (**Figure 2.1 c**)

which depends on the sizes of the nanowires. In a vortex wall, magnetisation curls in the plane of the film around a central vortex core where the magnetisation points out of the plane. A transverse wall occurs when the small width of the nanowire makes the exchange cost of a circulating magnetisation larger than the demagnetising cost of a transverse magnetisation distribution.

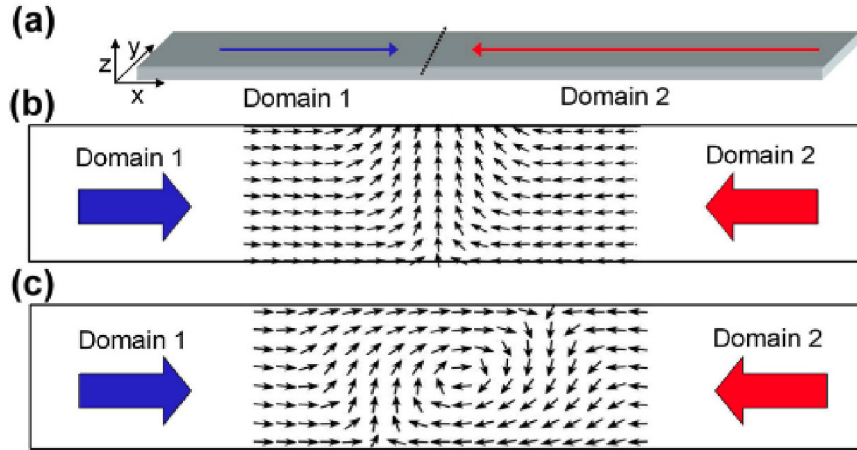


Fig. 2.1 (a) Schematic representation of a magnetic wire with two domains pointing in opposite directions (red and blue arrows) and a domain wall (dotted line). (b) Top view of the magnetic texture of a transverse DW and (c) a vortex DW. Figure is reproduced from [51] under CC4 Attribution licenses.

If we extrude the 2D nanowire into 3D, the extra degree of freedom gives a more complex panorama of DW types [50]. For example, the magnetisation has freedom to curl around both the thickness and the wire axes and a domain wall can show features of both transverse and vortex walls simultaneously and hence known as transverse-vortex wall (**Figure 2.2 a**). Another interesting example is the case of a Bloch-point wall [24] which is characterised by an axial vortex where its axis is parallel to the wire and its magnetisation vector is topologically forced to vanish at a central singularity (**Figure 2.2 b**). Its existence was first

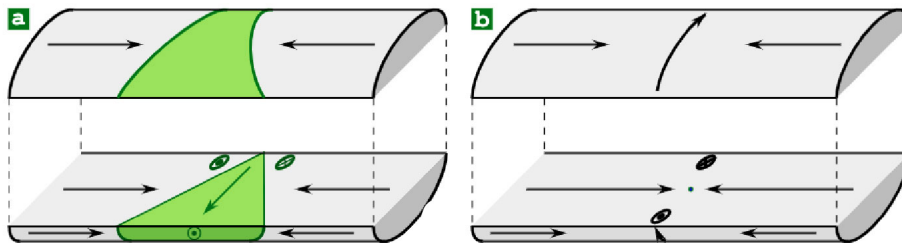


Fig. 2.2 (a) Schematic of a transverse-vortex wall (TVW). (b) Schematic of a Bloch-point wall (BPW). Figure is reproduced from [50] under CC4 Attribution licenses.

predicted by means of micromagnetic simulations [52] and then observed to be stable in cylindrical nanowires [24].

### 2.1.4 Magnetic simulations

Magnetic simulations are useful tools for improving our understanding of nanomagnetic systems, especially 3D systems, where the magnetic configurations are inherently more complicated than 2D systems due to higher degrees of freedom. In this thesis, two types of simulations are involved. The first one is micromagnetic simulations, which solve the phenomenological Landau-Lifshitz-Gilbert (LLG) equation [53, 54] numerically by discretising a simulated system into small unit cells (**Figure 2.3 a**) which can be a cube or tetrahedra depending on whether the finite difference (FD) or finite element (FE) method is used. In chapters 4 and 5, micromagnetic simulations are used to identify magnetic states during the reversal processes of 3D nanomagnetic systems. The second type is the macrospin simulation, which assumes that all magnetic moments in a simulated system have the same direction and is also known as the single-domain approximation (**Figure 2.3 b**). Macrospin modelling is used in chapter 3 in a high-field angular dependence study of a 3D cobalt nanobridge. The introduction of both simulations is given below.

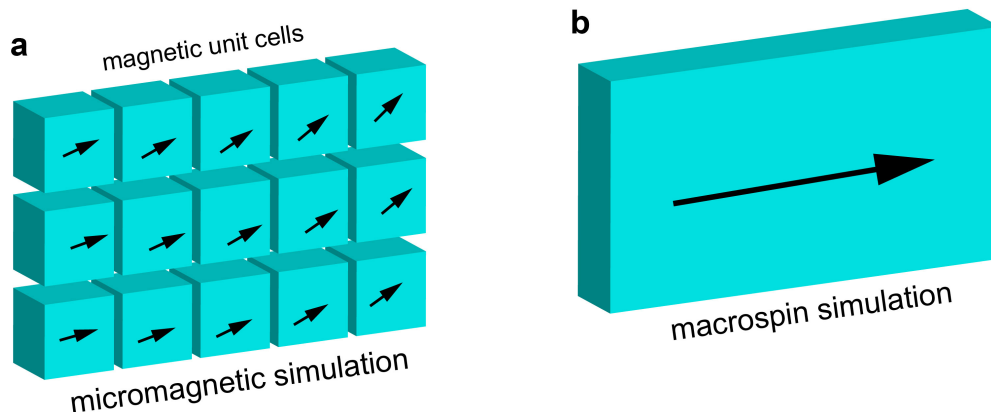


Fig. 2.3 *Two types of magnetic simulations used in this thesis. (a) Micromagnetic simulation. (b) Macrospin simulation.*

#### Micromagnetic simulation

Magnetic configurations in nanostructures, as seen in the previous section, can be extremely complex, particularly in the 3D nanomagnets investigated in this thesis. Hence, micromagnetic simulations implemented from the fundamental equations of micromagnetic theory that

describe the spatial and temporal evolution of the magnetisation vector field are essential for gaining a deep understanding of experimental observations as well as promoting research towards new effects in 3D nanomagnets.

In 1935, Landau and Lifshitz [53] showed that the existence of domains is a consequence of energy minimisation and the total energy can be obtained by summing up all the energy terms mentioned above:

$$E_{tot} = \int_V A[(\nabla m_x)^2 + (\nabla m_y)^2 + (\nabla m_z)^2] + \frac{E_a}{V} - \mu_0 \vec{M} \left( \frac{1}{2} \vec{H}_d + \vec{H}_{app} \right) dV \quad (2.9)$$

To derive how a micromagnetic equilibrium is reached, the concept of effective field,  $\vec{H}_{eff}$ , is introduced which is the summation of the external field, exchange field, demagnetising field and magnetocrystalline anisotropy field acting on  $\vec{M}$ :

$$\vec{H}_{eff} = -\frac{1}{\mu_0 V} \frac{\partial E_{total}}{\partial \vec{M}} = \vec{H}_{ex} + \vec{H}_k + \vec{H}_d + \vec{H}_{app} \quad (2.10)$$

Magnetic states in a ferromagnetic material can be simulated by integrating the Landau-Lifshitz-Gilbert (LLG) equation [53, 54], which defines the time evolution of the magnetisation under the effective field,  $\vec{H}_{eff}$ , where  $\gamma$  and  $\alpha$  are the gyromagnetic ratio and the phenomenological damping coefficient, respectively.

$$\frac{d\vec{M}}{dt} = \gamma \frac{1}{1 + \alpha^2} \left( \vec{m} \times \vec{H}_{eff} + \alpha \left( \vec{m} \times \left( \vec{m} \times \vec{B}_{eff} \right) \right) \right) \quad (2.11)$$

$\vec{H}_{eff}$  exerts a torque on the magnetisation vector of each ‘magnetic unit cell’ and induces a precession movement, which is described by the first term in the largest parentheses in Equation 2.11. The magnetisation is reoriented toward the effective field following a damping process as described by the second term. The lateral size of the ‘magnetic unit cell’ (mesh size) should be less than the characteristic exchange-dipolar length  $l_{ex} = \sqrt{2A/\mu_0 M_s^2}$  of the magnetic material with negligible magnetocrystalline anisotropy.

There are several micromagnetic simulation packages available to solve the LLG equation numerically and the two packages used in this work are MuMax3 [55] and Magnum.fe [56]. MuMax3 employs a finite-difference methods (FDM) that discretize space in a cubic lattice of voxels, while Magnum.fe uses a finite-element method (FEM) that discretizes the space with no fixed length. The FEM can adapt to complex geometries with high accuracy and, therefore, is better suited for simulating 3D shapes, especially if curved surfaces are involved.

On the other hand, FDM generally has higher speed and is easier to use and implement [57]. The details of the simulation setup will be given in the corresponding results chapters.

### Macrospin simulation

Macrospin simulation is also known as ‘single-domain’ approximation, as the magnetisation in a sample can be assumed to be uniform [58]. This approximation can be applied in cases such as ferromagnetic nanoparticles with lateral sizes equal to few times the exchange length or samples under high fields where the Zeeman energy dominates over all other energies. Here, since the magnetisation is uniform, the exchange energy is zero and the demagnetising field is uniform and there exists a demagnetisation tensor  $\tilde{N}$  such that

$$\vec{H}_d = -\tilde{N}\vec{M}. \quad (2.12)$$

$\tilde{N}$  is generally given by a function of the dimensions of the magnetic sample, and can be expressed in the basis of the principal axes:

$$\tilde{N} = \begin{pmatrix} N_x & 0 & 0 \\ 0 & N_y & 0 \\ 0 & 0 & N_z \end{pmatrix} \quad (2.13)$$

Instead of using the complicated formula, the mean demagnetising field and magnetostatic energy can be calculated easily with the equivalent demagnetising tensor. Hence, an analytical expressions of the total energy can be obtained as:

$$E_{tot} = \frac{1}{2}\mu_0 M_s^2 V (N_x m_x^2 + N_y m_y^2 + N_z m_z^2) - \mu_0 M_s V \vec{m} \cdot \vec{H}_a \quad (2.14)$$

Since we use this macrospin model only in an high-field study, the magnetocrystalline energy is ignored. The details of the application of macrospin simulation in a high-field study of 3D nanomagnets will be given in chapter 3.

## 2.2 Magnetotransport effects

Matthiessen's empirical rule states that the total electrical resistivity of a crystalline metallic specimen has several contributions [59, 60]:

$$\rho(T) = \rho_{imp} + \rho_{e-e}(T) + \rho_{ph}(T) + \rho_{mag}(B, T), \quad (2.15)$$

where  $\rho_{imp}$  is the residual resistivity due to impurities,  $\rho_{e-e}$  is due to the electron-electron interactions and  $\rho_{ph}$  is the electron-phonon scattering. These first three terms are weakly dependent on an applied magnetic field, and in this section, we focus on  $\rho_{mag}$  which is the resistivity originating from magnetism and how it can be used to investigate 3D magnetic structures.

The component of  $E_i$  of the electric field inside a conductor are related to the current density  $J_j$  through

$$E_i = \sum_j \rho_{ij} J_j, \quad (2.16)$$

where the  $\rho_{ij}$  coefficients form the resistivity tensor. In the case of an isotropic ferromagnet, generally, the resistivity tensor have the following components as shown in **Equation 2.17**. Because of the 3D vector nature of both the current and magnetisation in 3D nanomagnets, a vector expression is used for ease of interpretation.

$$\vec{E} = \underbrace{\rho_{\perp}(B)\vec{J}}_{\text{Lorentz MR}} + \underbrace{[\rho_{\parallel}(B) - \rho_{\perp}(B)](\vec{m} \cdot \vec{J})\vec{m}}_{\text{Anisotropic MR}} + \underbrace{\rho_H(B)\vec{m} \times \vec{J}}_{\text{Hall effects}}, \quad (2.17)$$

where  $\vec{J}$  is the current vector,  $\vec{m}$  is a unit vector in the magnetisation direction,  $\vec{B}$  is the total induction  $\mu_0(\vec{H}_a + \vec{H}_d + \vec{M})$ ,  $\vec{H}_a$  is the external field, and  $\vec{H}_d$  is the demagnetising field.  $\rho_{\parallel}$  and  $\rho_{\perp}(B)$  are the resistivity for  $\vec{J}$  parallel and perpendicular to  $\vec{m}$ , respectively and  $\rho_H$  is the Hall resistivity.

The first term represents the Lorentz MR which is a result of the curving of the carrier trajectory by the Lorentz force. This is a very small effect in most metals and hence is not considered [60]. The second and third term take account of the anisotropic magnetoresistance (AMR) and the Hall effects, respectively. In this section, we will introduce the AMR and Hall effects in detail, and an additional magnon magnetoresistance which is also observed in our 3D nanomagnets. These effects form the resistivity tensor and will be used in the finite

element modelling of the magnetotransport measurements in 3D nanomagnetic systems, and will be introduced in detail in **chapter 3, section 3**.

### 2.2.1 Anisotropic magnetoresistance

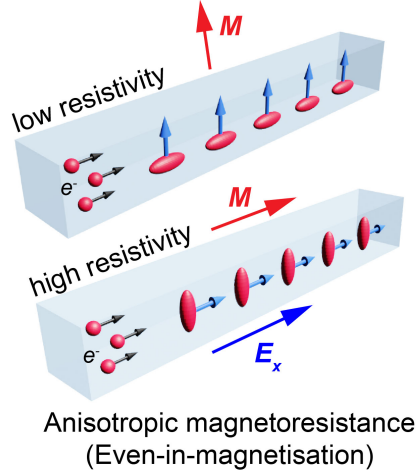


Fig. 2.4 **Anisotropic magnetoresistance:** variation in resistance induced by different degrees of scattering of spin-orbit coupled carriers. Figure is reproduced from [61].

In a metallic ferromagnet, the variation of resistivity in the presence of external magnetic field typically exhibits the AMR effect in which the resistance depends on the angle between the current direction and magnetisation directions [62]. The AMR effect arises from the spin-orbit coupling *i.e.*, the orientation of the electron orbitals in a ferromagnetic material is coupled to the direction of the magnetisation. For some metals, such as cobalt, this results in a greater scattering cross-section for a transport electron when the direction of the current is parallel to the magnetisation as shown in **Figure 2.4**, hence increasing the resistivity [63, 62]. The AMR effect can be described phenomenologically as [60]:

$$\vec{E}_{\text{AMR}} = (\rho_{\parallel} - \rho_{\perp})(\vec{m} \cdot \vec{J}) \vec{m}, \quad (2.18)$$

where  $\vec{E}_{\text{AMR}}$  is the change in electric field induced by AMR effect,  $\vec{J}$  is the current density vector,  $\vec{m}$  is a unit vector in the magnetisation direction, and  $\rho_{\parallel}$  and  $\rho_{\perp}$  are the resistivities for  $\vec{J}$  parallel and perpendicular to  $\vec{m}$ , respectively.

From Equation 2.18, we see the induced electric field depends on the angle between the magnetisation and the direction of the current and it will not change with the reversed magnetisation. The component of  $\vec{E}_{\text{AMR}}$  on the current direction is usually known as the



AMR, while the component on the direction perpendicular to the current direction is known as the planar Hall effect (PHE). This is a misnomer, as was already pointed out by Jan *et al.*, since PHE is just the complementary manifestation of the same resistivity anisotropy and is an even-in-field effect which has nothing to do with the Hall effect [64].

AMR is widely used for magnetic sensors such as the first generation of MR read heads in hard disk drives [8]. Since AMR is sensitive to magnetisation, it has also been used to investigate magnetisation reversal processes in nanostructures such as nanowires [65]. It can also detect the presence of a DW as the local variation of the magnetisation within the DW will deviate from the current direction, resulting in a change in resistance [66]. The AMR can be sensitive to the details of the DW structures as well. In particular, it can distinguish vortex and transverse walls in a nanowire [67] as they reveal a different component of the magnetisation that is parallel to the current. However, AMR measurements are not sensitive to the position of a DW, they can only detect the presence or absence of a DW in between the electrical contacts.

### 2.2.2 Anomalous Hall effect

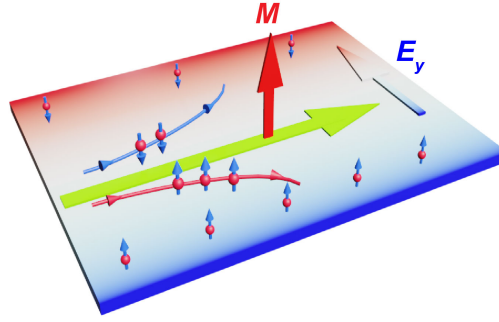
In ferromagnets, the Hall resistivity  $\rho_H$  in **Equation 2.17** consists of two contributions, the ordinary and anomalous Hall effect proportional to the total induction  $\vec{B}$  and the magnetisation  $\vec{m}$ , respectively. The Hall effect is thus described as [60]:

$$\vec{E}_H = \underbrace{R_{\text{OHE}} \vec{B} \times \vec{J}}_{\text{ordinary Hall effect}} + \underbrace{\rho_{\text{AHE}} \vec{m} \times \vec{J}}_{\text{anomalous Hall effect}}, \quad (2.19)$$

where  $R_{\text{OHE}}$  is the ordinary Hall coefficient ( $R_{\text{OHE}} = \rho_{\text{OHE}}/B$ ),  $\vec{B}$  is the total induction ( $\vec{B} = \mu_0(\vec{H} + \vec{M})$ ),  $\vec{J}$  is the current density vector,  $\vec{m}$  is a unit vector in the magnetisation direction, and  $\rho_{\text{AHE}}$  is the anomalous Hall resistivity.

The ordinary Hall effect (OHE), existing in any conductor, is associated with the Lorentz force acting on moving charges. It is determined by the component of the total effective field that is normal to the current plane [60]. The anomalous Hall effect (AHE) is a much larger effect in ferromagnets than the OHE and it depends on the out-of-current-plane component of magnetisation. This effect is attributed to asymmetric spin-orbit scattering. As shown in **Figure 2.5**, electrons with opposite spins are deflected in different directions due to spin-orbit coupling mediated intrinsic and extrinsic (skew-scattering and side-jump) scattering related mechanisms [68]. Both OHE and AHE are odd-in-field or magnetisation effects. Their

induced transverse electric field changes sign with the reversal of field or magnetisation. Experimentally, when increasing an out-of-current-plane applied field,  $\vec{E}_H$  changes rapidly at first primarily due to the AHE as a result of the alignment of the magnetisation, and then tends to vary in proportion to the applied field due to the OHE only.



Anomalous Hall effect  
(Odd-in-magnetisation)

Fig. 2.5 **Anomalous Hall effect:** electrons with opposite spins are deflected in different directions due to the spin-orbit coupling mediated scattering mechanisms. Figure is reproduced from [61].

AHE has been extensively used as a technique to detect magnetisation reversal in nanostructures with perpendicular magnetisation and by using a Hall cross geometry, it is also commonly used to study DW motion [69]. Since AHE usually provides a large signal, it allows the detection of DW motion on a scale as small as 10 nm within the Hall cross [70]. However, AHE only points out the position of a DW within a Hall cross, which limits the flexibility of the device geometries.

### 2.2.3 Magnon magnetoresistance

A magnon is the quasi-particle associated with spin-waves, *i.e.*, a small disturbance in local magnetic ordering that can propagate in a magnetic material in the form of a wave [71]. The dispersion relation of magnons has a quadratic form, with an energy gap proportional to the effective magnetic field felt by the magnons [59]:

$$E(k) = Dk^2 + g\mu_B B, \quad (2.20)$$

where  $D$ ,  $\mu_B$  and  $g$  are the material-dependent spin wave stiffness constant, the Bohr magneton and the Landé factor, respectively. When the magnetisation and the applied field are parallel,

an increase of the applied field induces a shift of the dispersion curve towards higher energies, and consequently a decrease of the magnon population. This phenomenon can be described as the spin lattice becomes more rigid under increasing applied field [72].

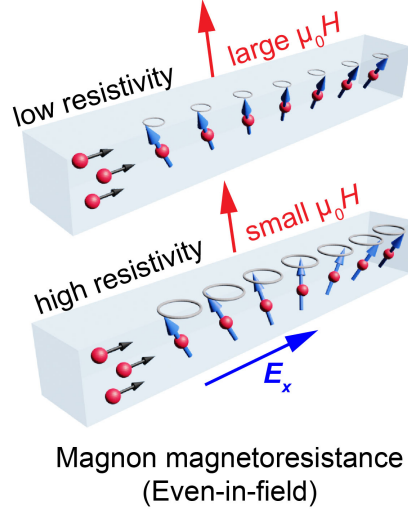


Fig. 2.6 **Magnon magnetoresistance:** reduced resistance due to the suppression of spin waves by an applied magnetic field. Figures are reproduced from [61].

In 2002, Raquet *et al.* showed that the resistivity of 3d ferromagnets decreased almost linearly with the applied field up to 30 T. As shown in **Figure 2.6**, this is explained by the progressive suppression of spin disorder caused by spin waves under an increasing field strength, which results in a drop of resistance due to a reduction in the electron-magnon scattering. For a constant temperature, this negative change of resistivity that almost decreases linearly with increasing field is known as magnon magnetoresistance (MMR) and can be described by [59]:

$$\Delta\rho_{mmr}(T,B) \approx \rho(T,B) - \rho(T,0) \propto \frac{BT}{D(T)^2} \ln\left(\frac{\mu_{Bohr}B}{k_B T}\right), \quad (2.21)$$

where  $T$  is the temperature,  $D(T)$  is the temperature dependent magnon stiffness,  $\mu_{Bohr}$  is the Bohr magneton,  $k_B$  is the Boltzmann constant, and  $B$  is the projection of the total effective field,  $\vec{B} = \mu_0(\vec{H} + \vec{M})$ , on the direction of the magnetisation, *i.e.*, the magnitude of the total effective field, acting to suppress the magnitude of spin-waves present in the system. Here  $\vec{H}$  is the vector sum of the applied field  $\vec{H}_a$ , demagnetising field  $\vec{H}_d$ , and anisotropy field  $\vec{H}_k$ ,  $\vec{H} = \vec{H}_a + \vec{H}_d + \vec{H}_k$ , and  $\vec{M}$  is the magnetisation.

MMR depends on the total effective field and hence contains of information on different aspects of the system such as magnetisation and demagnetising field distribution along the

sample under study. By carefully designing the materials and geometry of a system, MMR has been for instance used to detect the magnetisation reversal and domain wall position in FePt nanowires with strong perpendicular anisotropy [72, 73].

## 2.3 Experimental methods

In this section, the experimental methods used to create and characterise 3D nanomagnetic circuits are presented. For the fabrication of samples, we discuss a 3D nano-printing tool, focused electron beam induced deposition (FEBID). In addition to FEBID, other 2D nanofabrication techniques were used, including various lithographic and thin film deposition techniques. We will introduce how these methods are used in the fabrication of 3D circuits in the following chapters. The working principles of these techniques are not discussed here as they are standard techniques that are widely used in the field of nanotechnology. For more information about these lithography and thin film deposition methods, the reader can consult these references [74–76]. The magnetotransport measurement setup based on phase-sensitive detection is then introduced, followed by magneto-optical Kerr effect (MOKE) magnetometry.

### 2.3.1 Focused electron beam induced deposition

As an important tool in our study to create 3D nanomagnetic circuits, focused electron beam induced deposition (FEBID) is a direct writing method to create true 3D nanostructures. It uses an electron beam to control chemical vapour deposition at the nanometre scale. The FEBID process is illustrated in **Figure 2.7 a**. First, precursor molecules are injected and constantly replenished into the vacuum chamber of a Scanning Electron Microscope (SEM) (**Figure 2.7 b**) using a Gas Injection system (GIS). GIS is a fine needle that is typically inserted within 50  $\mu\text{m}$  of the desired deposition position. The use of GIS creates high pressure locally to enable the FEBID process and, at the same time, avoids contamination of the chamber and the SEM electron optics. Then, upon irradiation of the electron beam available from the SEM, precursor molecules previously adsorbed on a substrate surface are dissociated into both volatile and non-volatile parts [77]. Volatile parts will be removed under the vacuum system with the unused precursor molecules, while non-volatile parts stay on the substrate and form the solid deposit. By carefully controlling the time electron beam stays on each spot and the pitch of its movement, fabrication of 3D deposits can be achieved.

FEBID processes are governed by three main processes [77, 78]:

- The first is the substrate-precursor molecule interaction in which the diffusion, adsorption and desorption of precursor molecules on the substrate need to be considered. These processes can be influenced by GIS flux, the substrate material and temperature of the substrate, *etc.*

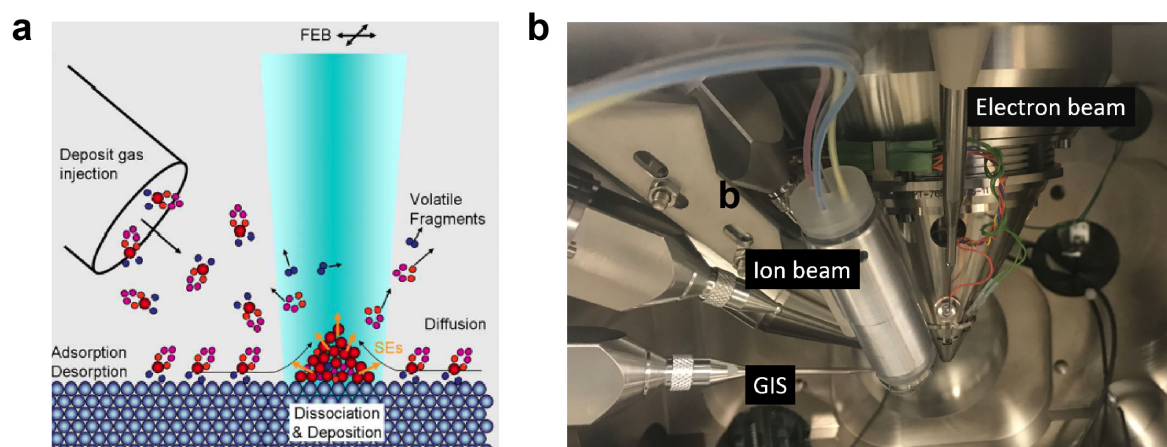


Fig. 2.7 (a) A schematic FEBID process: precursor molecules adsorb, desorb, and diffuse at the surface and are dissociated under electron beam irradiation. Figure is reproduced from [77] under CC4 Attribution licenses. (b) View of a SEM chamber, with the position of electron beam, ion beam and GIS shown.

- The second is the electron-substrate interaction, as not only primary electrons from the electron beam can interact with precursor molecules, but the secondary electrons (SEs) generated from the substrate also have enough energy and a much higher probability to dissociate the precursor molecules. As a result, although the electron beam can be focused to a spot size down to a few nanometres, the spatial resolution of FEBID can not reach this level and is determined by the interaction volume of the electron beam incident on the substrate. The accelerating voltage of electrons is one of the parameters that determines the spread of secondary electrons. High acceleration voltage is preferred when growing 3D structures because it generates fewer SEs near the surface and thus improves the spatial resolution of the deposition [79]. For all 3D growth in our experiments, the highest available accelerating voltage (30 kV) was used.
- The third is the electron-precursor molecule interaction in which electrons with sufficient energy (few eV) break the bonds in precursor molecules. For better control in the 3D nanoprinting, we prefer this process to happen in the ‘*electron-limited*’ regime, *i.e.*, the dissociation of molecules are limited by the number of electrons and is less dependent on the gas flux. Hence, relatively low beam currents were used in our experiments.

Typically, organo-metallic gas precursors are used for FEBID. In this thesis, dicobalt octacarbonyl  $[\text{Co}_2(\text{CO})_8]$  and methylcyclopentadienyl-trimethyl platinum  $[(\text{CH}_3)_3\text{Pt}(\text{CpCH}_3)]$  are involved. The decomposition of these precursors is very different, resulting in completely

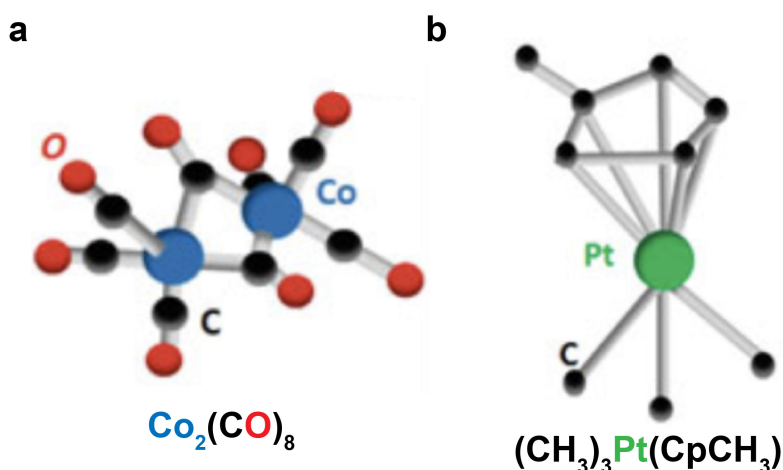


Fig. 2.8 Chemical structures of the two metal-organic gases used in this thesis. (a)  $\text{Co}_2(\text{CO})_8$ . (b)  $(\text{CH}_3)_3\text{Pt}(\text{CpCH}_3)$ . Figure is reproduced from [74] under CC4 Attribution licenses.

different physical properties. Using  $\text{Co}_2(\text{CO})_8$ , cobalt with purity up to 95 % can be achieved under certain deposition conditions [38]. This precursor is used to create a cobalt nanoridge directly as will be shown in chapter 3 and 4. On the other hand,  $(\text{CH}_3)_3\text{Pt}(\text{CpCH}_3)$  can only deliver deposits with Pt purity of around 15 %. This low purity comes from a carbonaceous matrix present in the deposits as a result of the incompletely decomposed precursor [80]. However, this precursor is very suitable for producing a non-magnetic scaffold to support multi-layered magnetic materials, as will be demonstrated in chapter 5.

FEBID growth relies on a vast number of parameters due to the complicated physical phenomena involved, as mentioned previously. For the practical application of FEBID in 3D nanoprinting, significant effort has been made towards developing and applying a FEBID growth model that enables to predict and understand experimental results with a reduced number of parameters [81, 82]. These advancements have improved FEBID growth from a trial-and-error approach to the systematic creation of electron beam instructions that include beam position and dwell time. In this thesis, we employ a framework developed by Skoric *et al.* that is based on the FEBID continuum model [82] that enables us to fabricate arbitrary 3D structures out of files created by standard CAD software, the same approach followed by standard 3D printers [37]. A detailed description of how this framework is used will be given in Chapter 3.

### 2.3.2 Magnetotransport measurements

#### Lock-in detection

Lock-in detection or phase sensitive detection is a powerful method to detect small signals in the presence of high noise and is prevalently used in different magnetotransport measurements [51, 83]. For an experiment excited at a fixed reference frequency, a lock-in amplifier can detect the response from the experiment at this reference frequency. Noise signals, at frequencies other than the reference frequency, are rejected and do not affect the measurement.

Typically, an experiment is excited at a reference frequency,  $\omega_r$ , then the response expected is :

$$V_{\text{sig}} \sin(\omega_r t + \theta_{\text{sig}}), \quad (2.22)$$

where  $V_{\text{sig}}$  is the signal amplitude,  $\omega_r$  is the signal frequency and  $\theta_{\text{sig}}$  is the signal's phase. The lock-in amplifier also generates its own internal reference signal and the internal reference can be written as

$$V_L \sin(\omega_L t + \theta_{\text{ref}}). \quad (2.23)$$

Then the lock in amplifier multiplies the signal and the lock-in reference using a multiplier (also known as phase-sensitive detector). The output is simply the product of two sine waves which is:

$$\begin{aligned} V_{\text{psd}} &= V_{\text{sig}} V_L \sin(\omega_r t + \theta_{\text{sig}}) \sin(\omega_r t + \theta_{\text{ref}}) \\ &= \frac{1}{2} V_{\text{sig}} V_L \cos([\omega_r - \omega_L]t + \theta_{\text{sig}} - \theta_{\text{ref}}) - \\ &\quad \frac{1}{2} V_{\text{sig}} V_L \cos([\omega_r + \omega_L]t + \theta_{\text{sig}} + \theta_{\text{ref}}). \end{aligned} \quad (2.24)$$

As given in Equation 2.24, the output can be written as the sum of two AC signals, with one at the difference frequency ( $\omega_r - \omega_L$ ) and the other at the sum frequency ( $\omega_r + \omega_L$ ). If we pass this output signal through a low pass filter, the AC signals can be removed. Moreover, if we set  $\omega_L = \omega_r$ , the difference frequency component will be a DC signal. In this case the filtered output will be:

$$V_{\text{psd}} = \frac{1}{2} V_{\text{sig}} V_L \cos(\theta_{\text{sig}} - \theta_{\text{ref}}) \quad (2.25)$$

This results in a nice DC signal proportional to the signal amplitude. Normally, noise signals at frequencies other than the reference frequency are rejected and do not affect the measurement.



### Magnetotransport measurement setup

Most of the magnetotransport (MT) measurements described in this thesis are done in a bath flow Helium cryostat as shown in **Figure 2.9**, except for the measurements described in chapter 5 which are done on a "MOKE + MT" setup. The fabricated sample is mounted on a chip carrier and placed in the sample holder at the end of the cryostat probe. This system can be configured up to 9 T fields in the direction along the probe using a superconducting magnet. The sample holder can rotate up to  $90^\circ$  in an axis perpendicular to the probe axis and hence the magnetic field varies out of the plane of the sample substrate.

After placing the sample in the cryostat, we now consider the electrical measurement setup as shown by the schematic in **Figure 2.10**. First, lock-in amplifier one provides an AC excitation voltage to the sample at a reference frequency  $\omega_r$  (see the pink line). Here,  $\omega_r$  is set to 33 Hz to avoid noise from the main power line. The series resistor  $R_c$  in the circuit serves to maintain a constant current and its resistance is chosen to be much larger than the measured sample. In our case, we used a  $R_c=10\text{ k}\Omega$  with the sample resistance of around few ohms. Hence, the lock in excitation and the series connector  $R_c$  can be seen as a

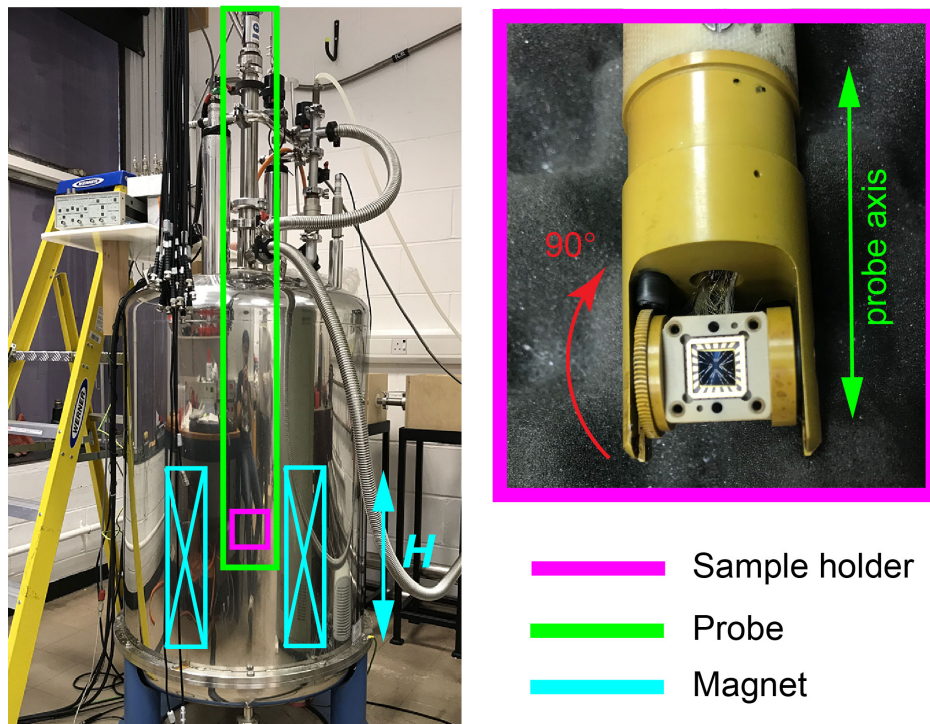
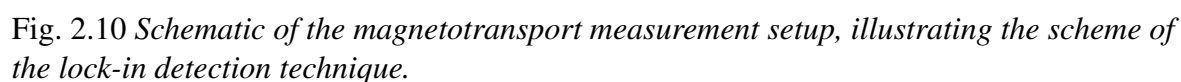


Fig. 2.9 Picture of Magnetotransport measurement setup used. The positions of the sample probe, sample holder and electromagnets are labelled.



voltage-controllable current source. Then, as shown by the green line, the voltage across the sample is first amplified by a pre-amplifier and then the signal that has the same frequency  $\omega_r$  is detected by the same lock-in. Here, a four-terminal sensing technique is used, so that the contact resistance as well as Galvanic potential in the connections between metals can be eliminated. The second lock-in amplifier is used to measure the voltage across the constant resistor  $R_c$  and hence monitor the current in the system and its internal reference frequency is synchronised with the first lock-in as shown by the red line. In summary, the first lock in amplifier excites the experiment and measures the voltage across the sample and the second lock in measures the current. Therefore, we can calculate the resistance of the sample under different applied fields.

### 2.3.3 MOKE Magnetometry

A magnetometry technique used in this thesis is a magneto-optic technique: the spatially resolved Magneto-Optical-Kerr-Effect (MOKE). MOKE is fundamentally related to the spin-polarised electronic band structure and the interaction between incident light and magnetisation in the material via spin-orbit coupling of electrons in the material [84]. The effect is manifested by the change of polarisation and/or intensity of incident polarised light when it is reflected from the surface of a magnetised medium and can be described as non-diagonal terms in the permittivity tensor dependent on the magnetisation vector as shown below [84]:

$$\tilde{\epsilon} = \epsilon \begin{pmatrix} 1 & -iQm_z & iQm_y \\ iQm_z & 1 & -iQm_x \\ -iQm_y & iQm_x & 1 \end{pmatrix}. \quad (2.26)$$

As shown in **Figure 2.11**, there are three configurations of MOKE, longitudinal, transverse and polar depending on the relative direction of the magnetisation to the optical plane. Longitudinal Kerr is sensitive to in-plane magnetisation that lies parallel to the optical plane. If a p-polarised light ( $E_x, 0, E_z$ ) incidents on a magnetic surface, from the permittivity tensor, we can see the longitudinal magnetisation  $m_x$  will create an  $E_y$  term with  $E_z$ , inducing a rotation and ellipticity in the reflected beam. In the transverse Kerr case,  $m_y$  only alters the magnitude of  $E_x$  and  $E_z$ , hence only the intensity of light has changed. Hence, for

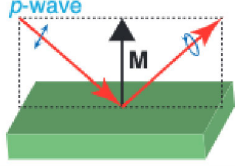
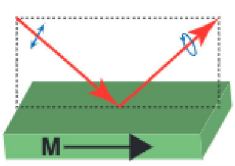
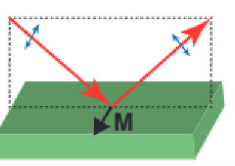
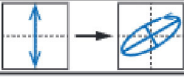
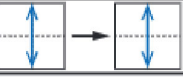
Name	(a) Polar	(b) Longitudinal	(c) Transverse
Geometry			
Detection	Out-of-plane	in-plane	in-plane
Polarization Variation	Rotation Ellipticity		None 
Measurement	Polarization Analysis		Intensity measurement

Fig. 2.11 Schematic diagram of MOKE measurement geometries for p-polarised incident light. Figure is reproduced from [85] under CC4 Attribution licenses.

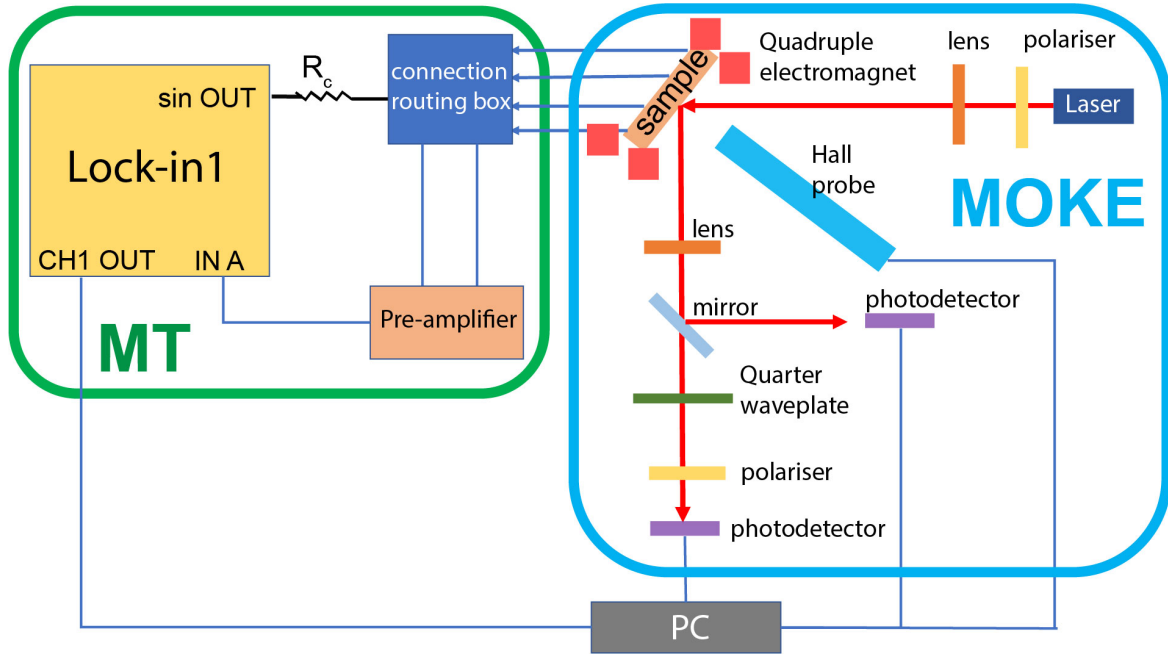


Fig. 2.12 Schematic of the MOKE + MT setup used in this thesis to simultaneously measure magnetotransport and optical signals of samples

an in-plane magnetic system, magnetic response of  $m_x$  could be found by measuring the rotation or ellipticity of the reflected beam and  $m_y$  could be measured through the intensity of the reflected beam. The longitudinal and transverse Kerr signals were measured for a multilayered 3D nanobridge as shown in chapter 5.

A spatially resolved MOKE with a laser spot size of  $5\ \mu\text{m}$  was used in our project. MOKE was originally developed for thin film analysis, but with the improvement in sensitivity, spatial resolution, and temporal resolution of MOKE equipment, it has been used to study the behaviour of nanostructures such as nanodot chains or nanowires and to image domain wall propagation in thin films [86]. A schematic of the set-up used is shown in the blue box in **Figure 2.12**. The Kerr measurement starts with a laser that is polarised linearly using a polariser set at  $0^\circ$ . The beam is focused onto the sample which is mounted at  $45^\circ$  to the optical axis. Part of the reflected beam is directed through a quarter wave plate which converts ellipticity into rotation. If the polarised light was perfect, the optimal signal would be obtained with the final polariser set at  $90^\circ$ . The intensity of reflected light is measured as well by a second photodetector to obtain information for transverse magnetisation.

In our group, this set up was extended to perform MOKE and MT characterisation simultaneously [87] by mounting a chip carrier socket on the MOKE sample holder and this chip carrier socket is wired to a connector box (**Figure 2.13 a**). This sample holder places the sample at the centre of the quadrupole magnets ((**Figure 2.13 b**)) in the MOKE system. The sample is connected in to electrical circuits via the connector box and the same four-probe lock in method as described before is applied to obtain the magnetotransport results.

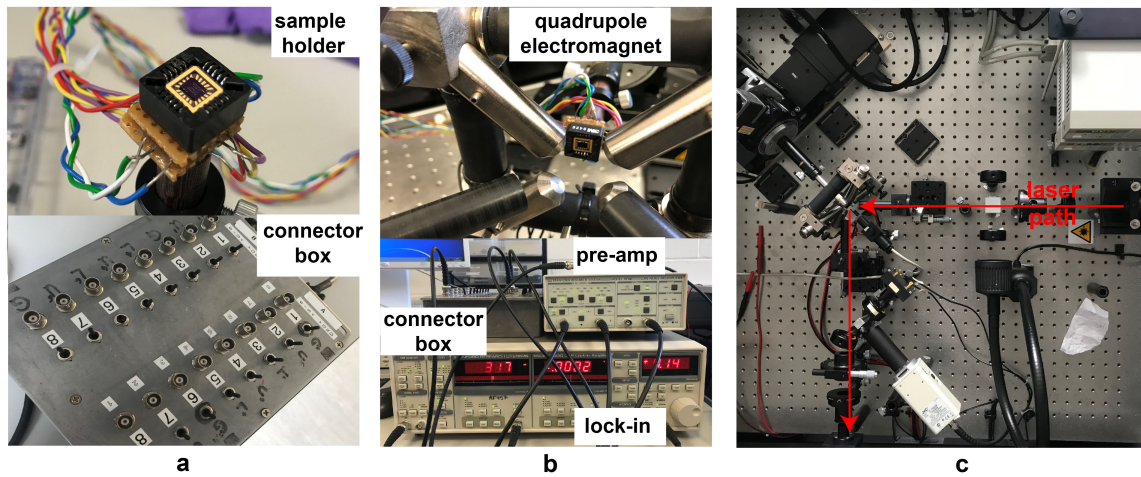
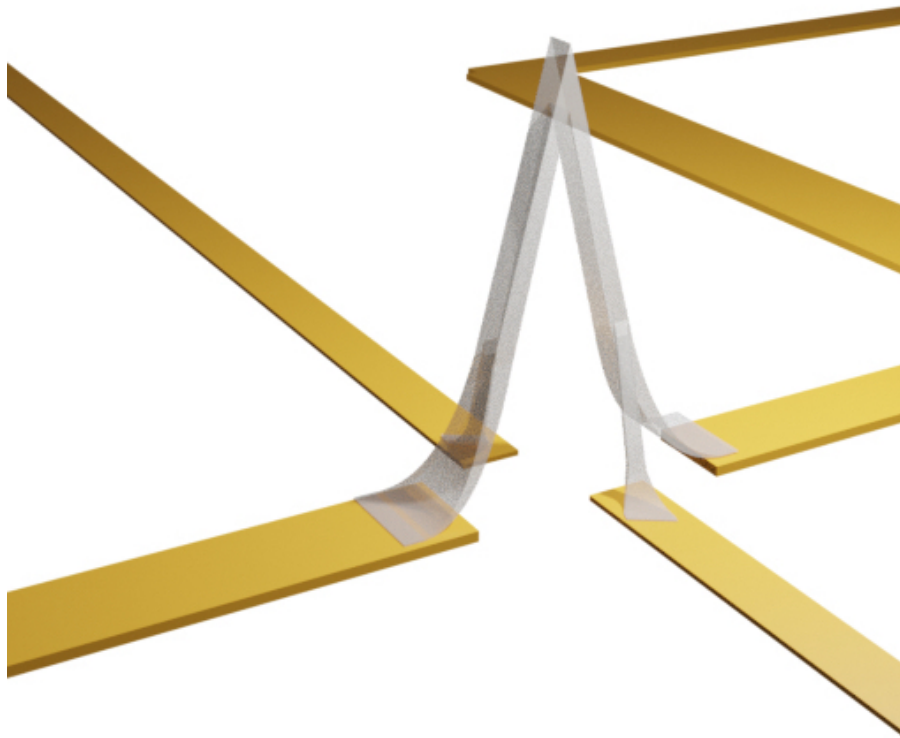


Fig. 2.13 (a) A chip carrier socket wired to a connector box. (b) A sample placed at the centre of quadrupole magnets and electrical measurement setup. (c) Picture of the MOKE setup.



## **Chapter 3**

# **Magnetotransport Properties of a 3D Cobalt Nanobridge under High Magnetic Fields**



## Published Material Included in This Chapter

A substantial part of the work presented in this chapter has been previously published in the following article:

**Meng, F.** et al. Non-Planar Geometrical Effects on the Magnetoelectrical Signal in a Three-Dimensional Nanomagnetic Circuit. *ACS Nano* 15, 6765–6773 (2021).

This is published under a Creative Commons Attribution (CC-BY) License. Being the result of my own original work, considerable parts of this article are reproduced in this thesis as allowed by this license.



## Contributions

This chapter is divided in to three sections, contributions from other colleagues are listed below:

### ■ Section 3.1. Direct Fabrication of a 3D Nanomagnetic Circuit

- Optical lithography process used for fabricating large electrical contacts are done in Durham Magneto Optics Ltd by Dr Jung-wei Liao.
- Electron beam lithography and electron beam evaporation for fabricating fine-size electrical contacts are done in Nanoscience Centre, University of Cambridge, with the help from Dr Zhuocong Xiao.
- The algorithm used to generate codes for computerized beam control for 3D nano-printing is developed by our group member Luka Skoric. The experimental work of 3D nano-printing was performed by myself in the Materials and Condensed Matter Physics group at the University of Glasgow.

### ■ Section 3.2. Magnetotransport measurements

- I would like to thank Dr Stuart Holmes who set up the helium bath flow cryostat and gave me the training for magneto-transport measurements, and also Dr Peter Newton who helped me to refill liquid helium every two weeks during the measurements.

### ■ Section 3.3. Understanding magnetotransport results at high fields

- The finite element method of micromagnetic simulations used to obtain demagnetising factors of the 3D structures were performed by Dr Claas Abert at University of Vienna.
- I would also like to thank Dr Claire Donnelly, Dr Amalio Fernandez Pacheco, and Dr Aurelio Hierro-Rodriguez for their advice on the development of the simulation methodology for understanding magnetoelectrical signals from 3D geometries.

All the results presented in this chapter are the result of my own work.

## Introduction

Before conceptual 3D spintronic applications such as the 3D racetrack memory [18] or neuromorphic networks [21] can be realised, a fundamental understanding of the influence of 3D geometries on magnetotransport properties is critical. However, due to significant challenges in the fabrication of 3D nanomagnets and their integration into 2D microelectronic circuits, the varieties of 3D geometries whose magnetotransport properties have been experimentally studied are quite limited, focusing primarily on cylindrical nanowires [26, 88]. Hence, to study the influence of more complex geometries and fully exploit the potential of 3D spintronics, new methods are needed.

In this chapter, we first present a fabrication method to directly integrate a complex 3D magnetic nanostructure into a microelectronic circuit based on focused electron beam induced deposition (FEBID), a 3D nano-printing technique. Recent advances in FEBID can deliver high purity ferromagnetic materials such as cobalt [38] while at the same time offering increased control over the geometry of the 3D structures [37, 81]. We demonstrate this method by fabricating a 3D nanomagnetic circuit based on a nanobridge geometry which is a basic element to interconnect the electrical and magnetic parts in a circuit and has also been proposed as one of the key building blocks in 3D spintronics [12].

After successfully establishing a 3D circuit based on a nanobridge, we characterise intrinsic magnetotransport effects such as anisotropic magnetoresistance and anomalous Hall effects in this circuit with a thorough angular dependence study under high external fields. To have a better quantitative understanding, we also developed a simulation tool that is based on both macrospin simulations and finite element modelling. We discovered that three dimensionality directly affects the magnetoelectrical signals in several ways, including deviations from the usual angular dependence of anomalous Hall effects and significant angular dependent magnon magnetoresistance not found in planar systems. These findings are important to the understanding of 3D spintronic systems and underpin future fundamental and device-based studies.

### 3.1 Direct fabrication of a 3D nanomagnetic circuit

To realise a 3D nanomagnetic circuit, two steps are required: first, create an arbitrary 3D shape with the required material properties, and then connect such a 3D magnetic nanostructure into 2D microelectronics circuits. However, in existing approaches, these two steps can not be integrated seamlessly, necessitating sophisticated micro-manipulation processes for the transfer and alignment of the 3D nanomagnets and contacts [26, 83, 89, 90]. This complicated process not only reduces the efficiency of creating a 3D circuit, but also limits the geometries that may be explored, which are mainly limited to cylindrical nanowires so far.

To overcome these issues, we employ focused electron beam induced deposition (FEBID), an additive fabrication technique with a spatial resolution of tens of nanometres [91–93]. Inspired by conventional 3D printers, recent developments in FEBID now make it possible to design beam scanning instructions of almost arbitrary 3D nanostructure geometries with varying curvatures and topologies, directly from standard 3D computer aided design (CAD) files [37]. In this way, with the appropriate use of precursor gases, 3D structures of high-quality ferromagnetic materials [38, 40] can be fabricated directly on almost any substrate [77]. These capabilities make FEBID an ideal technique for the prototyping of 3D circuits in a simpler way by the deposition of a 3D nanomagnets with desired geometry onto pre-patterned electrical contacts directly.

#### 3.1.1 Design of the geometry to be studied

First, we introduce the design of the geometry to be studied. The magnetic nanobridge is one of the critical building blocks in 3D spintronics. This type of device not only interconnects electrical and magnetic parts easily in a nanomagnetic circuit [12], but can also host magnetic domain walls (DWs) [94] and spin waves [71], allowing magnetic information to be transferred, processed and stored at a different plane. These abilities offer the possibility of non-traditional computing architectures in which the boundaries between interconnects, memory and logic are eliminated [17].

A rendering of the bridge design explored in this study is shown in **Figure 3.1**. Aside from the bridge, which serves as the main conduction channel, two side-legs are introduced to allow standard four-probe measurements. These side legs are arranged diagonally across the main channel so that both longitudinal and transverse magnetoelectrical signals can be measured together, therefore providing complementary information about the magnetic state of the device. This design promotes an efficient use of space on the substrate as only four

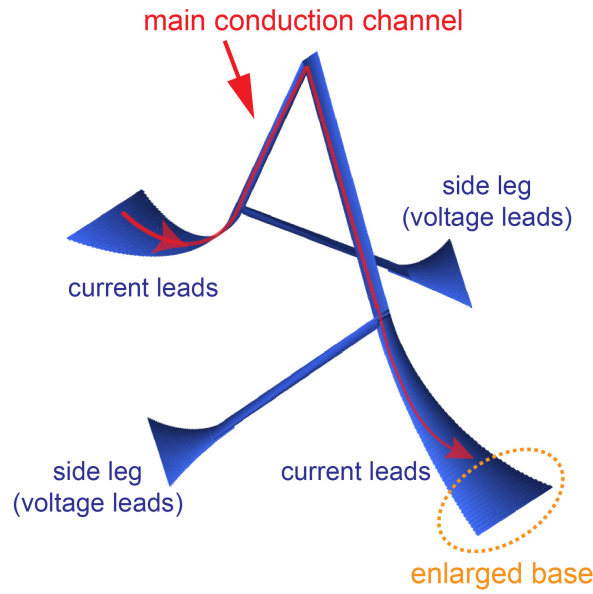


Fig. 3.1 A rendering of the CAD design of the nanobridge investigated in the experiment. Reproduced from [61].

planar pads are required to fully probe a high aspect ratio 3D nanostructure. It also increases the mechanical stability of the device, by having rotational-symmetric leads at both sides of the main bridge. The enlarged bases of the bridge used here are intended to improve both the bridge stability and electrical contact with the pads.

### 3.1.2 Fabrication process

The fabrication of a 3D nanomagnetic circuit is summarised by the schematic shown in **Figure 3.2**. To begin the process, gold contacts were patterned via various lithographic techniques on a silicon substrate with a 300 nm thick silicon dioxide layer (**Figure 3.2 a, b**). Prior to 3D nanoprinting, trenches were milled by focused ion beam to minimise the influence of parasitic deposits [77] on transport measurements (**Figure 3.2 c**). Then, the desired geometry (**Figure 3.1**) was directly printed on gold contacts via FEBID with a cobalt based precursor, and ready to be connected into an electrical circuit (**Figure 3.2 d, e**). Details of each step are given below.

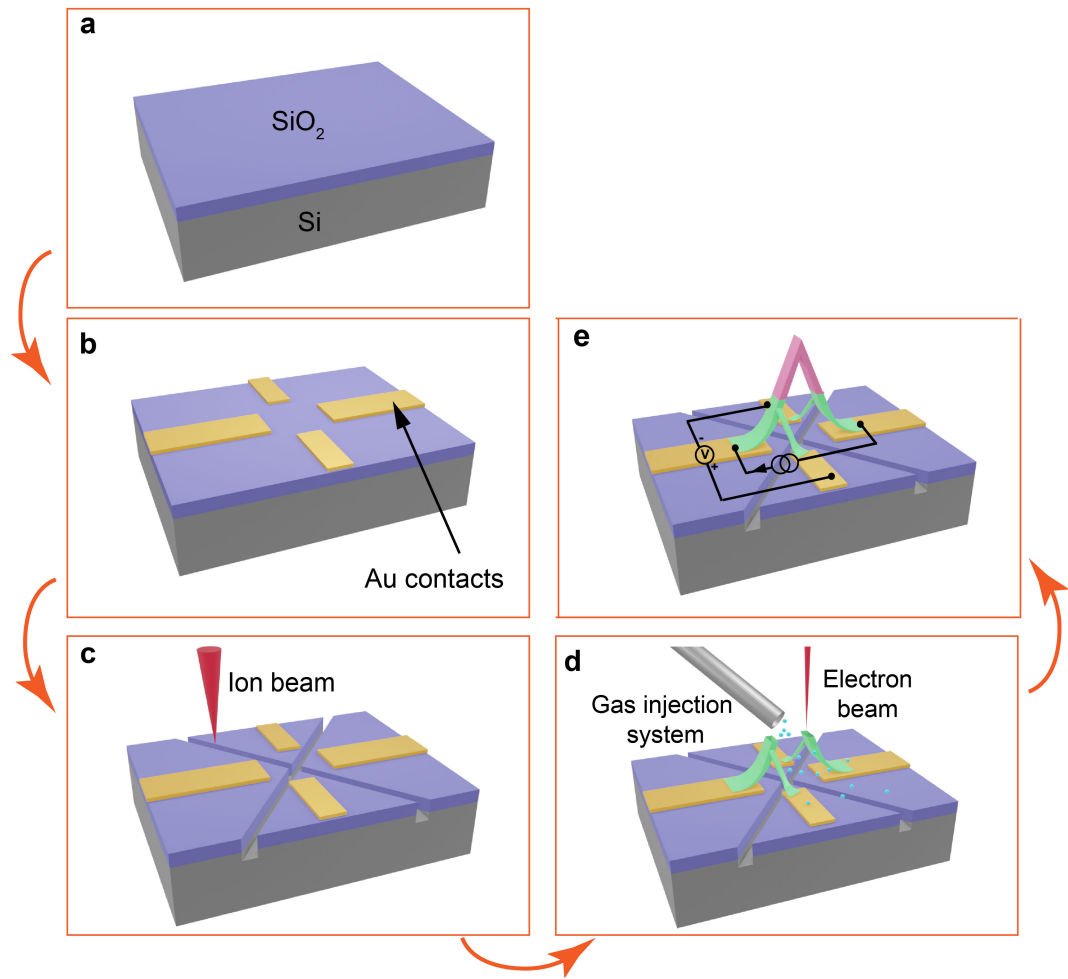


Fig. 3.2 *Direct integration of a ferromagnetic 3D nanobridge in a microelectronic circuit. (a) preparation of a clean silicon dioxide substrate. (b) patterning of electrical contacts. (c) milling of trenches by focused ion beam. (d) 3D-nanoprinting of the bridge via focused electron beam induced deposition. (e) Four-probe magneto-transport measurement configuration, where the voltage across the pink region is measured. Reproduced from [61].*

### Electrical contacts

Fabricating electrical contacts on a clean silicon dioxide substrate is the first step. The line widths of those contacts vary significantly, with wire bonding pads (**Figure 3.3 a**) being 200  $\mu\text{m}$  wide, and those connected to the nanobridge (**Figure 3.3 b**) with a width of 500 nm. Therefore, to improve fabrication efficiency, two processes are involved: optical lithography for big contacts and e-beam lithography for small contacts. Fabrication parameters used for both processes are summarised in **Table 3.1**.

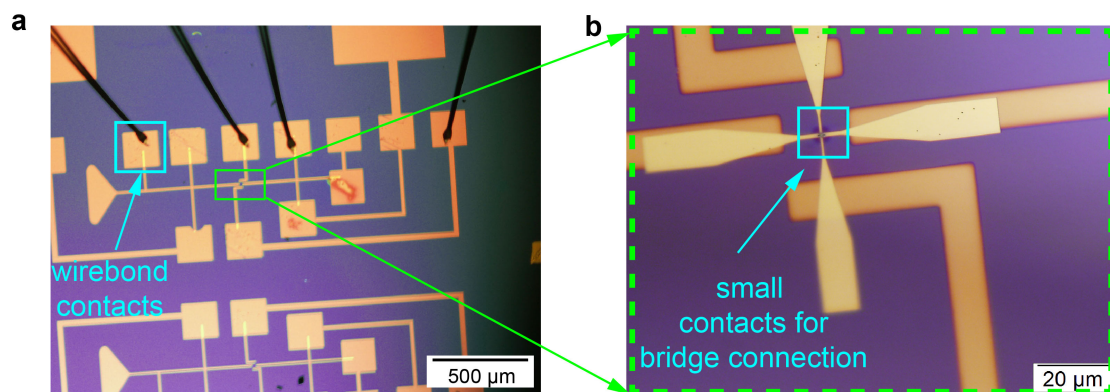


Fig. 3.3 *Electrical contacts. (a) Large electrical contacts for wire bonding. (b) Small electrical contacts for connecting the 3D nanobridge. The 3D nanobridge is deposited within the blue square.*

Fabrication of electrical contacts		
	big contacts	small contacts
<b>Methods</b>	optical lithography	e-beam lithography
<b>Equipment</b>	MicroWriter ML2	Crestec CABL-9000 C
<b>Beam</b>	laser beam, diameter 1 $\mu\text{m}$	electron beam, beam current 1 nA
<b>Resist</b>	AZ ECI 3027 (thickness:600 nm)	PMMA 950 A4 (thickness:100 nm)
<b>Developer</b>	AZ326	1:3 methyl isobutyl ketone (MIBK)/isopropyl alcohol (IPA)
<b>Oxygen plasma</b>	30s	10s
<b>Metallisation</b>	DC magnetron sputtering	ebeam evaporation
<b>Materials</b>	Ta/Au (2/30 nm)	Cr/Au (2/50 nm)
<b>Resist stripper</b>	SVC 14	acetone

Table 3.1 *Fabrication parameters used for making electrical contacts.*

### Focused ion beam (FIB) milling

In FEBID processes, mainly secondary electrons participate in the precursor molecule dissociation and the fabrication of the main deposit is governed by the secondary electrons (SEs) generated near the surface by primary electrons [93, 77]. However, there are also SEs generated by highly energetic back-scattered electrons (BSEs), leading to the deposition of a parasitic halo around the main deposit [77] and giving rise to electrical leakage resistance [95]. The lateral size of the halo depends on the BSE-exit area which relates to many factors such as substrate materials, beam energy and beam current [96]. Other factors such as autocatalytic growth and surface activation process can also cause unintended deposition, further expanding the halo beyond the BSE-exit area [93].

In order to minimise the influence of conducting parasitic deposits during the transport measurements, trenches were milled by  $\text{Xe}^+$  focused ion beam (FIB) in between the electrical contacts. We estimated the diameter of the halo associated with our desired bridge to be around  $4\text{ }\mu\text{m}$  by depositing a bridge without the FIB cut as shown in **Figure 3.4 a**. The details of FEBID will be given in the next section. Hence, we have milled two  $8\text{ }\mu\text{m}$ -long trenches in parallel to ensure they can cover the halo as much as possible (**Figure 3.4 b**). Milling was performed in a Helios<sup>TM</sup> G4 PFIB UXe DualBeam<sup>TM</sup> FIB/SEM (University of Glasgow) with parameters set as: acceleration voltage=30 kV, beam current=0.34 nA and nominal depth=500 nm.

We also used the ion beam with a beam current of 0.24 pA to etch away nominally 1-nm-thick material from the Au contacts (green squares in **Figure 3.4 c**), to clean the surface contaminants and ensure good contact with the 3D nanobridge.

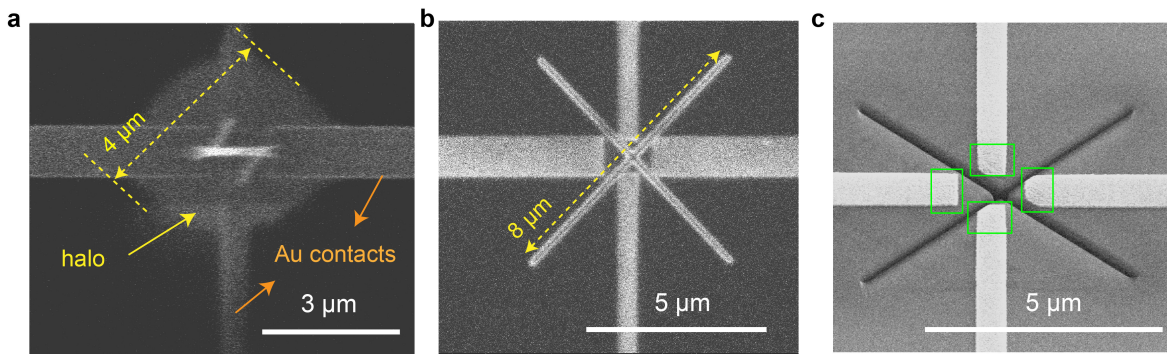


Fig. 3.4 FIB milling. (a) The size of the halo is estimated for the bridge to be deposited. (b) Lengths of the FIB milled trenches (c) FIB cleaning of the contacts

### Focused Electron Beam Induced Deposition (FEBID)

Following the preparation of the electrical contacts and the trenches between them, we now consider the 3D nano-printing of the desired bridge geometry. In recent years, the application of FEBID for 3D nanofabrication has advanced significantly, progressing from a trial-and-error approach to systematic creation of electron beam instructions that include beam position and dwell time [81]. In particular, we used an algorithm developed by our group member Luka Skoric, which is capable of creating beam scanning patterns directly from conventional 3D printing stereolithography (STL) file formats, the same approach followed by standard 3D printers [37].

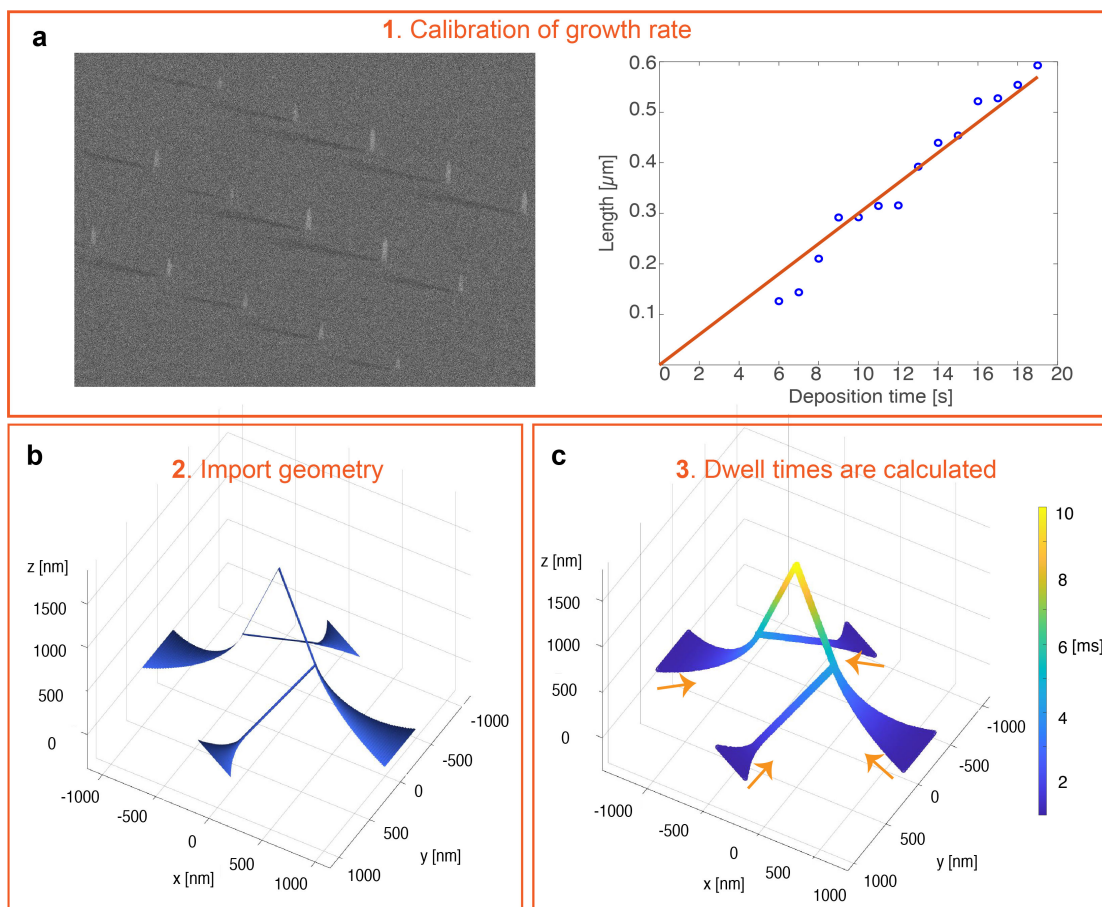


Fig. 3.5 Workflow of the algorithm to deposit a 3D nanobridge by FEBID. (a) Calibration of growth rate. (b) Geometry importation to the algorithm. (c) Generation of beam position and dwell time from the algorithm.

In our experiment, FEBID was performed in a Helios<sup>TM</sup> G4 PFIB UXe DualBeam<sup>TM</sup> FIB/SEM (University of Glasgow) using the following conditions: dicobalt octacarbonyl [ $\text{Co}_2(\text{CO})_8$ ] as precursor gas, chamber pressure =  $8 \times 10^{-7}$  mbar, acceleration voltage = 30



kV, and beam current = 0.34 nA. These conditions have been reported to result in greater than 95 at.% cobalt with nanocrystalline microstructure [38]. We first calibrated the growth rate under these conditions by building a set of spot depositions in parallel with different total deposition times. The resulting lengths of the vertical nanowires are measured and plotted against the deposition times and a growth rate of  $33 \text{ nm s}^{-1}$  is determined (**Figure 3.5 a**). Then, we imported the desired geometry to the algorithm (**Figure 3.5 b**) and the beam positions and dwell times can be calculated and written to a streamfile that can be read directly by the pattern generator of the scanning microscope. As shown in **Figure 3.5 c**, segments that have higher angles with respect to the substrate require longer dwell time to construct, and the four branches of the bridge were deposited in parallel.

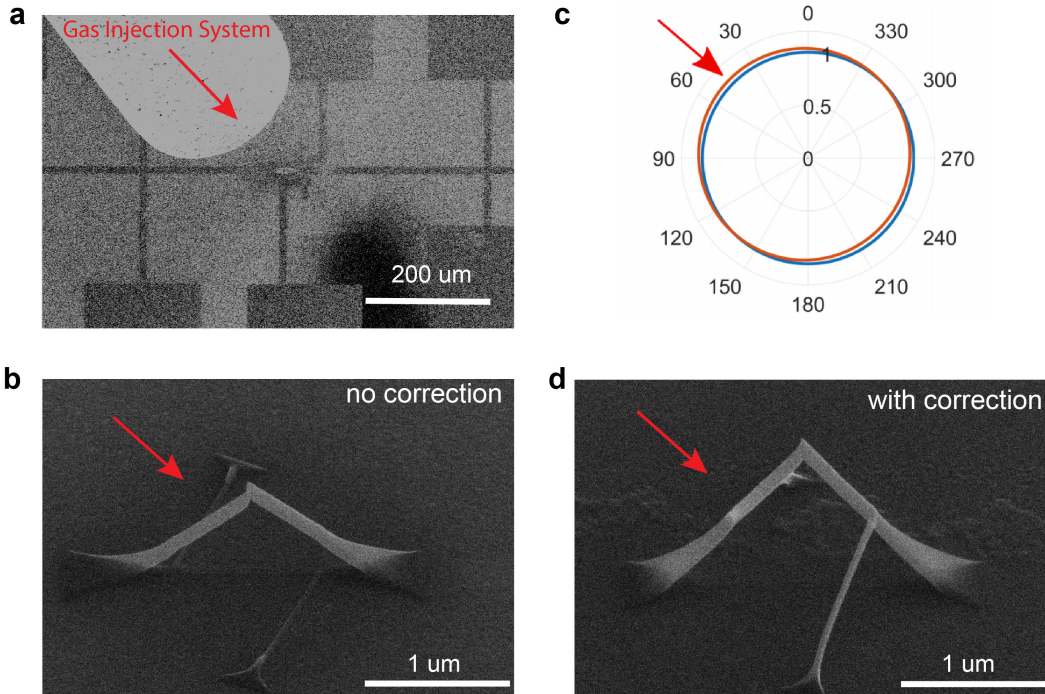


Fig. 3.6 *Correction for gas flux anisotropy. (a) Position of the gas injection system (GIS). Red arrows mark the direction of precursor flux. (b) Bridge built without gas anisotropy correction (c) Red circle: normalised scaling factor with respect to the direction of GIS ( $\phi_0 = 45^\circ, \alpha = 0.05$ ), Blue circle: unit circle for comparison. (d) Bridge built with gas anisotropy correction.*

The nanobridge is designed for magnetotransport measurements, and the precise connection of all branches at the top of the bridge is essential in the successful establishment of a functional circuit. For structures with multiple parts that need to meet precisely, a second-order effect, gas flux anisotropy must be taken into account [97]. As shown in **Figure 3.6 a**, the gas injection system (GIS) is located at one side of the structure ( $\phi_0 = 45^\circ$  to the

vertical direction) leading to a slightly larger growth rate for segments deposited towards the GIS compared to the ones grown away from the GIS (**Figure 3.6 b**). This effect can be corrected by scaling the calculated dwell times by [37]

$$(1 + \alpha \cos(\phi - \phi_0)),$$

where  $\phi$  is the azimuthal angle of a structure,  $\phi_0$  is the GIS angle, and  $\alpha = 0.05$  is the first order scaling factor. This scaling factor with respect to the direction of GIS is plotted in **Figure 3.6 c**, where we can see for segments growing towards the GIS (azimuthal angle between  $180^\circ$  and  $270^\circ$ ), we 'manually' lowered its growth rate. A bridge built successfully using this correction is shown in **Figure 3.6 d**.

### The resulting 3D circuits

Using the methods described above, we have successfully connected a complex, high aspect ratio nanostructure to a planar circuit patterned on a substrate using well-defined leads. The resulting 3D nonmagnetic circuit is shown by scanning electron microscopy (SEM) images in **Figure 3.7 a, b** and geometrical information of the bridge can be obtained from these images.

From the top view image (**Figure 3.7 a**), the width of the main bridge is  $160 \pm 5$  nm and the width of the 'enlarged base' is  $490 \pm 5$  nm. The projection of one leg's probed section is  $350 \pm 5$  nm. By tilting the sample stage by  $45^\circ$  (**Figure 3.7 b**), we can calculate the angle  $\alpha$ , between the bridge and substrate. We have measured the projected angle  $\alpha'$  to be  $62 \pm 0.5^\circ$  and  $60 \pm 0.5^\circ$  from the SEM image, which is the  $45^\circ$  projection to the substrate plane. Hence, the real angles can be calculated as  $\alpha = \tan^{-1}[\frac{\tan(\alpha')}{\cos(45^\circ)}]$  to be  $69 \pm 0.6^\circ$  and  $68 \pm 0.6^\circ$ . There is only a  $1.6 \pm 0.8^\circ$  difference in the angles formed by the legs and the substrate, so the degree of asymmetry is very small in our structure. With  $\alpha$  known, the length of one side of the probed region is calculated to be  $960 \pm 40$  nm. Finally, the thickness of the measured bridge is estimated from a broken bridge (**Figure 3.7 c**) that was deposited under the same conditions, where the thickness is about 140 nm for the main bridge and 370 nm for the apex region. This geometrical information was used to create the 3D CAD-based model and FEM mesh used in the magnetoresistance calculation.

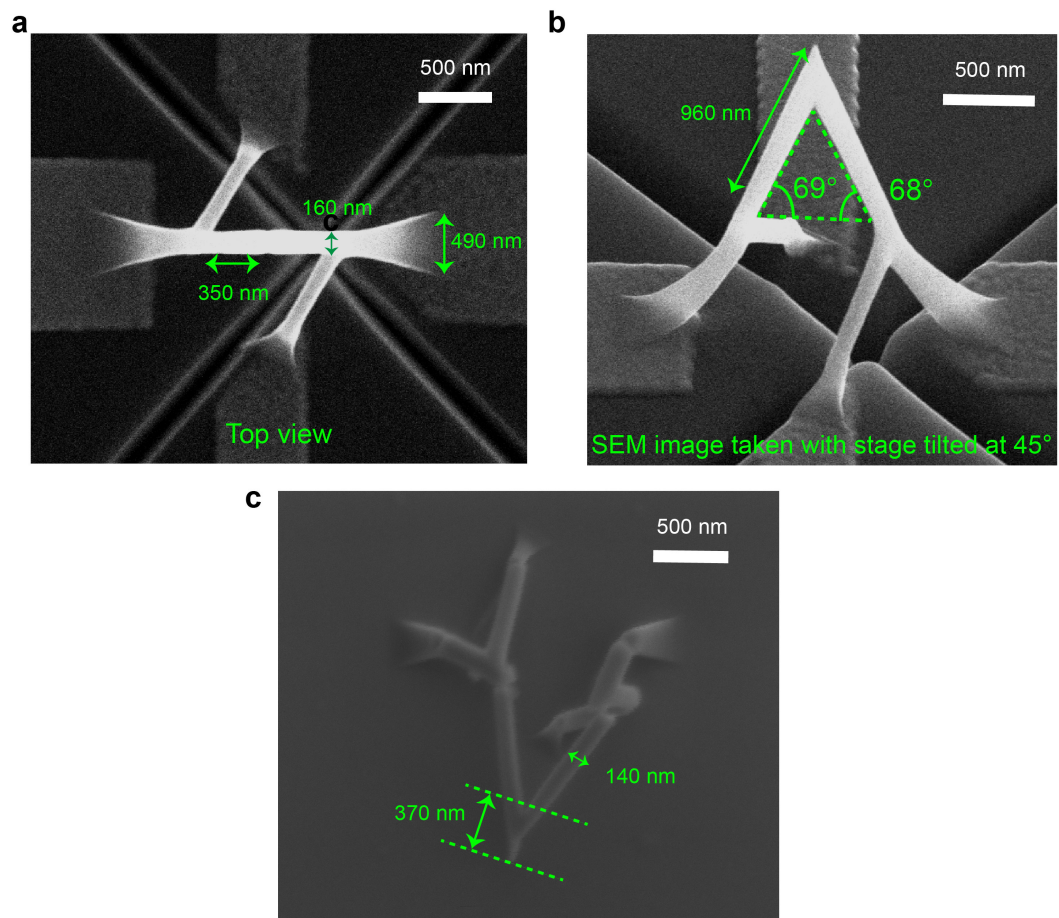


Fig. 3.7 SEM images of a resulting nanomagnetic circuit. (a) Side view of the fabricated nanomagnetic circuit. Image tilt of  $45^\circ$ . (b) Top view of the fabricated nanomagnetic circuit. (c) Top view of a broken bridge fabricated under the same conditions. Reproduced from [61].

## 3.2 Magnetotransport (MT) measurements

Following the realisation of the 3D nanomagnetic circuit, we next consider its magnetotransport (MT) measurements. The four branches of the nanobridge allow standard four-terminal AC lock-in technique to be employed. As shown in **Figure 3.8 a**, a current with a constant amplitude of  $0.6 \mu\text{A}$  at a frequency of 33 Hz was supplied through the main leg of the bridge while the voltage was measured across the side-leg contacts. By placing the voltage probes at both sides of the main conduction channel, this setup allows the measurement of both longitudinal and transverse voltage together.

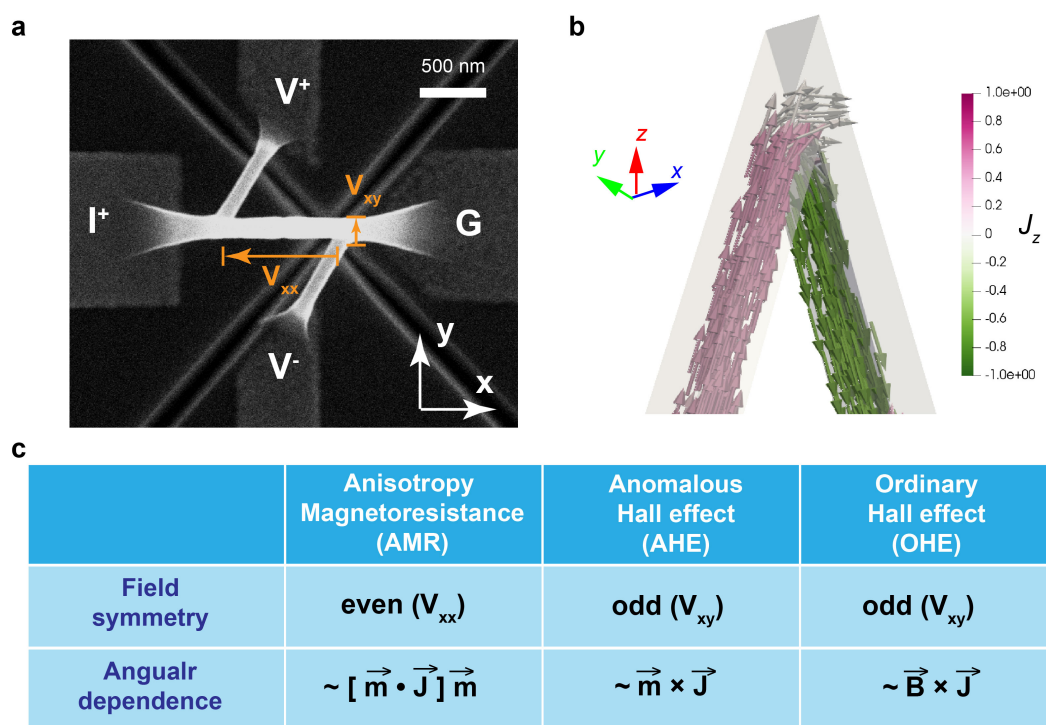


Fig. 3.8 *Magnetotransport measurements. (a) Four-probe magnetotransport measurement configuration, where the region between sidelegs was probed. (b) The simulation of the current density in the probed region of the 3D nanobridge with the colour indicating the z component of the current density. (c) Magnetoelectrical signals expected in a ferromagnetic structure and their field symmetries and angular dependencies [60].*

With this measurement setup combined with the 3D current profile in the nanostructure (**Figure 3.8 b**), regardless of which direction magnetic field is applied, we always expect to measure a superposition of multiple MT effects such as anisotropic magnetoresistance (AMR), planar Hall effect (PHE), anomalous Hall effect (AHE) and ordinary Hall effect (OHE), which are common intrinsic MT effects expected in single ferromagnetic materials

[60]. To understand the contribution of each MT effect to the total signal probed, and the influence of the 3D geometry, we performed measurements with the sample at different orientations with respect to the applied magnetic field direction. In this way, we can exploit their angular dependencies and field symmetries, which are usually their fingerprints as summarised in **Figure 3.8 c**.

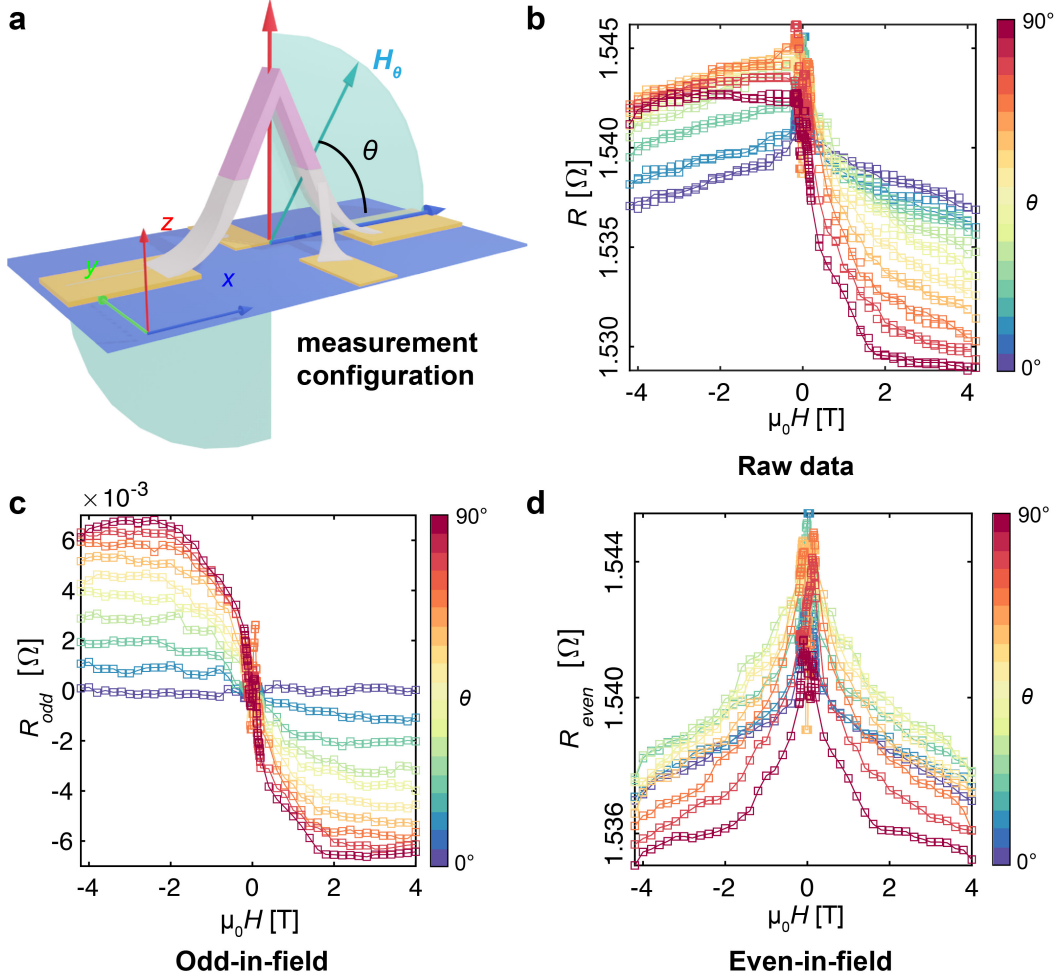


Fig. 3.9 Magnetotransport measurements. (a) The schematic shows how the field is applied relative to the 3D nanobridge,  $\theta$  is the angle between the applied field and the substrate. (b) MT hysteresis loops obtained from  $-4$  T to  $4$  T and  $4$  T to  $-4$  T for each field angle  $\theta$  from  $0^\circ$  to  $90^\circ$ . (c) Odd-in-field signal,  $R_{odd}$ . (d) Even-in-field signal,  $R_{even}$ . Reproduced from [61].

To obtain the angular dependence of the MT signal, we applied magnetic field from  $\theta = 0^\circ$  to  $\theta = 90^\circ$ , with an interval of  $10^\circ$  in the XZ plane as shown in **Figure 3.9 a**.  $\theta$  is defined as the angle between the applied field and substrate. To obtain information on the field symmetry, at each field direction we measured a full MT hysteresis loop from  $-4$  T

to 4 T and from 4 T to -4 T, plotted from violet to red in **Figure 3.9 b**. The two branches overlap at high fields, with the hysteresis loop confined to the low field region, which is the focus of chapter 4. All measurements were performed at 180 K. There is a clear angular dependence observed in the raw data, where the signal becomes less symmetric as the angle changes from  $\theta = 0^\circ$  to  $\theta = 90^\circ$ . Unlike in 2D, where Hall bars are often patterned to separate various MT effects, here we make use of the signal's different symmetries with regard to the sense of the applied field to differentiate coexisting MT effects. Specifically, the raw data is separated into the odd-in-field part as  $R_{odd} = [R(H) - R(-H)]/2$ , and the even-in-field part as  $R_{even} = [R(H) + R(-H)]/2$  as shown in **Figure 3.9 c** and **Figure 3.9 d**, respectively. In this chapter, we concentrated on the high field range only, where the magnetization is fully reversible, so that odd- and even-in-field signals correspond to odd- and even-in-magnetization effects.

With the raw data separated into odd and even parts, we first compare them qualitatively to the symmetries and angular dependence of the AMR, PHE, AHE and OHE on the current, internal magnetization and magnetic field induction [60]:

$$\vec{E} = \rho_{\perp} \vec{J} + \underbrace{(\rho_{\parallel} - \rho_{\perp})}_{\text{AMR+PHE}} (\vec{m} \cdot \vec{J}) \vec{m} + \underbrace{\rho_{AHE} \vec{m} \times \vec{J}}_{\text{AHE}} + \underbrace{R_{OHE} \vec{B} \times \vec{J}}_{\text{OHE}}, \quad (3.1)$$

where  $\vec{E}$  is the electric field,  $\vec{J}$  is the current density vector,  $\vec{m}$  is a unit vector in the magnetisation direction,  $\rho_{\parallel}$  is the resistivity for  $\vec{J}$  parallel to  $\vec{m}$ ,  $\rho_{\perp}$  is the resistivity for  $\vec{J}$  perpendicular to  $\vec{m}$ ,  $\rho_{AHE}$  is the anomalous Hall resistivity,  $R_{OHE}$  is the ordinary Hall coefficient ( $R_{OHE} = \rho_{OHE}/B$ , where  $\rho_{OHE}$  is the ordinary Hall resistivity, which is a function of  $B$ ) and  $\vec{B}$  is the total magnetic field induction,  $\vec{B} = \mu_0(\vec{H}_a + \vec{H}_d + \vec{M})$ . Here,  $\vec{H}_a$  is the applied field,  $\vec{H}_d$  is the demagnetising field and  $\vec{M}$  is the magnetisation.

First, we consider the odd contribution to the signal. The AHE is an odd-in-magnetisation effect, as its induced transverse electric field changes in sign with the reversal of magnetisation, and its strength is determined by the component of magnetisation perpendicular to the current ( $m_{\perp}$ ) [60, 68]. The ordinary Hall effect is also an odd-in-field effect, and is usually a much smaller effect compared to the AHE [60]. From the odd signal plotted in **Figure 3.9 c**, we observe that for all  $\theta$  values,  $R_{odd}$  appears to level off for applied fields greater than 2 T. As the AHE dominates the odd signal and depends on the magnetisation only, this indicates that the magnetisation is effectively saturated at a field around 2 T. Above 2 T, a small negative slope can be observed (most significant at  $\theta = 90^\circ$ ), which



we attribute to the ordinary Hall effect [38]. Quantitative analysis will be given in **section 3.3**.

We next check the even-in-magnetisation effects - typically the AMR and PHE, which are the longitudinal and transverse components of the anisotropic resistivity and remain the same when the magnetisation reverses. Given by the second term in Equation 3.1, their magnitude depends on the magnetisation parallel to the current direction ( $m_{\parallel}$ ) [60, 62]. The even signal measured in the bridge is plotted in **Figure 3.9 d**, where we notice that for all  $\theta$ , the resistance is always the highest when the applied field is around 0 T. This can be understood as the magnetisation at remanence tends to align along the long (easy) axes of the bridge due to shape anisotropy, which coincides with the current direction for this geometry. Since cobalt has a positive AMR ratio [38], the resistance is highest when the magnetisation and current directions are aligned. Secondly, unlike the odd signal, the even signal does not saturate at fields beyond 2 T but rather decreases further with applied field. As  $(\rho_{\parallel} - \rho_{\perp})$ , i.e., the AMR term in Equation 3.1, is not expected to change significantly after saturation [98], the measured change is attributed to the magnon magnetoresistance (MMR) [59, 73], which has been reported as a linear and non-saturating negative MR present after magnetic moments are fully saturated. MMR originates from the progressive suppression of spin disorder caused by spin waves in a ferromagnet under an increasing field strength, which results in a drop of resistance due to a reduction in the electron-magnon scattering [59]. The magnitude of MMR depends on the strength, and not the sign of the applied field, and has therefore an even response with the applied field. Quantitative analysis on the even signal will be given in **section 3.3** as well.

### 3.3 Quantitative understanding of magnetotransport results at high fields

To obtain a quantitative understanding of the different contributions of the aforementioned effects, we investigate the angular dependence of  $R_{odd}$  and  $R_{even}$  at high fields ( $\pm 4$  T). We concentrate on the data at high fields, where the magnetic state is close to uniform and the angular dependence of MT signals is usually the fingerprint of the underlying physical mechanisms.

As illustrated by Equation 3.1, to understand the MT measurements, we need to access both magnetisation ( $\vec{m}$ ) and current ( $\vec{J}$ ). Because of the 3D vectorial nature of both  $\vec{m}$  and  $\vec{J}$ , interpreting MT measurements in a 3D structure is particularly challenging. To assist our understanding of the measurements, we set up a MT simulation tool that makes use of both a multi-macrospin model and a finite element method (FEM) analysis, as explained below.

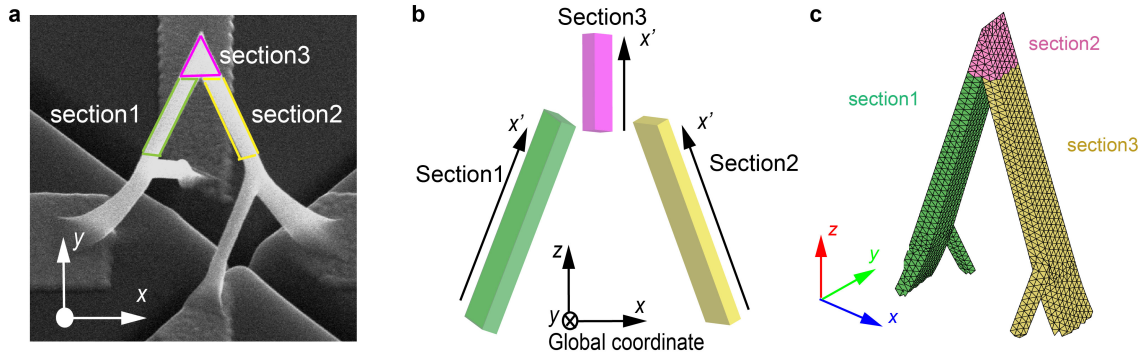


Fig. 3.10 The setup of the MT simulation tool. (a) The probed region of the structure is considered to be made up three independent nanowires. (b) Multi-macrospin model made up with three single-domain nanowires. (c) The FEM mesh of the bridge used to simulate MT signals. Reproduced from [61].

First, we need to determine the magnetisation of the bridge. An adapted multi-macrospin (multiple single domain) approximation is used here to determine magnetic configuration in the nanobridge at high-fields ( $\pm 4$  T) in a simple and computationally efficient way. The probed region of the structure is considered to be made up of three single-domain nanowires, as marked in green, pink and yellow, respectively in **Figure 3.10 a, b**. The interaction between the three regions is not considered in the model, i.e., the magnetization vectors for each section,  $\vec{m}_1(\theta)$ ,  $\vec{m}_2(\theta)$  and  $\vec{m}_3(\theta)$  are determined independently by minimising the sum of Zeeman and demagnetising energies of each section at a given  $\theta$ . Due to the nanocrystalline nature of FEBID Co under these growth conditions[38], which results in



magnetic properties dominated by shape anisotropy, we do not consider the intrinsic magnetocrystalline anisotropy of cobalt in the model. As described in **section 3.3.3**, this approach is sufficient to fully understand the magnetic behavior of the nanocircuit from MT signals under the application of high magnetic fields. The detailed setup of this model is described in **section 3.3.1**.

After obtaining magnetic configuration from the macrospin model, we simulate the MT signal by solving the electric potential  $u$  across the side contacts using a finite element method (FEM) with a CAD-based FEM mesh that reproduces the dimensions of the printed nanobridge **Figure 3.10 c**. The influence of different MT effects is summarized as a magnetization- and field- dependent resistivity tensor  $\rho(\vec{m}, \vec{B})$  rewritten from Equation 3.1 as:

$$\vec{E} = \rho(\vec{m}, \vec{B})\vec{J} \quad (3.2)$$

$$\rho(\vec{m}, \vec{B}) = \begin{pmatrix} \rho_{\perp} + \rho_G m_x^2 & \rho_G m_x m_y - \rho_{AHE} m_z - R_{OHE} B_z & \rho_G m_x m_z + \rho_{AHE} m_y + R_{OHE} B_y \\ \rho_G m_x m_y + \rho_{AHE} m_z + R_{OHE} B_z & \rho_{\perp} + \rho_G m_y^2 & \rho_G m_y m_z - \rho_{AHE} m_x - R_{OHE} B_x \\ \rho_G m_x m_z - \rho_{AHE} m_y - R_{OHE} B_y & \rho_G m_y m_z + \rho_{AHE} m_x + R_{OHE} B_x & \rho_{\perp} + \rho_G m_z^2 \end{pmatrix}, \quad (3.3)$$

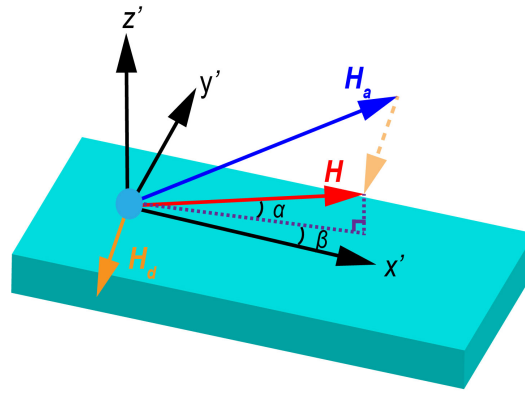
where  $m_x$ ,  $m_y$ , and  $m_z$  are the x, y and z component of the magnetization vector  $\vec{m}$ ,  $B_x$ ,  $B_y$  and  $B_z$  are the x, y and z component of the total magnetic induction  $\vec{B}$ .

For each section and angle  $\theta$  considered, a different resistivity tensor is calculated from the modelled magnetization distribution  $\vec{m}(\theta)$  and total field distribution  $\vec{B}(\theta)$ , and assigned to the corresponding sections of the nanobridge. We note that a non-magnetic conducting layer underneath the bridge due to Co parasitic deposition of cobalt [99] has been included in the simulations for a better quantitative agreement of the base resistance. After obtaining the potential difference between side contacts for fields applied in all directions, the odd part and even part of the simulated results can be separated in the same way as for the experimental data, for comparison. Details of the FEM simulation setup are given in **section 3.3.2**.

### 3.3.1 Multi-macrospin approximation

#### Determination of $\vec{M}$ in a single domain nanowire at high fields

As described before, a multi-macrospin model is used to determine the magnetisation in the nanobridge at fields ( $\pm 4$  T) in a simple, computationally efficient way. Before studying the 3D nanobridge, we first consider how to determine the magnetisation in a single domain nanowire with a known applied field by minimising the sum of Zeeman and demagnetising energies,



Local coordinate system

Fig. 3.11 *Macrospin model. The applied field  $\vec{H}_a$ , the demagnetising field  $\vec{H}_d$  and the effective field  $\vec{H}$  are considered for a nanowire in the local coordinate system.*

The energy in a single domain nanowire with a known applied field can be written as:

$$\vec{E} = -\mu_0 \vec{H}_a \cdot \vec{M} - \frac{1}{2} \mu_0 \vec{H}_d \cdot \vec{M}. \quad (3.4)$$

As shown in **Figure 3.11**, the magnetisation can be written with the local coordinate system  $x'y'z'$  as:

$$\vec{M} = M_s \begin{pmatrix} \cos(\alpha) \cos(\beta) \\ \cos(\alpha) \sin(\beta) \\ \sin(\alpha) \end{pmatrix}, \quad (3.5)$$

where  $\alpha$  is the angle between  $\vec{M}$  and the  $x'y'$ -plane,  $\beta$  is the angle between the projection of  $\vec{M}$  on the  $x'y'$ -plane with the  $x'$ -axis, and  $M_s$  is the saturation magnetisation of the material. The demagnetising field is the magnetic field generated by the magnetisation within the ferromagnet material and is determined uniquely by the geometrical shape of the body as

[100]

$$\vec{H}_d = -N\vec{M}. \quad (3.6)$$

The demagnetising field lies along the opposite direction of  $\vec{M}$ , and has a magnitude proportional to  $M$ . The coefficient  $N$  is the demagnetising factor and has three components  $[N_{x'} N_{y'} N_{z'}]$ , which are associated with the three-principal axes of the geometry, and they obey the general constraint  $N_{x'} + N_{y'} + N_{z'} = 1$ . The demagnetising field can be written as

$$\vec{H}_d = -M_s \begin{pmatrix} N_{x'} \cos(\alpha) \cos(\beta) \\ N_{y'} \cos(\alpha) \sin(\beta) \\ N_{z'} \sin(\alpha) \end{pmatrix}. \quad (3.7)$$

The applied field is

$$\vec{H}_a = -H_a \begin{pmatrix} a_{x'} \\ a_{y'} \\ a_{z'} \end{pmatrix}, \quad (3.8)$$

where  $[a_{x'} a_{y'} a_{z'}]$  is the unit vector for the applied field. Hence the total energy  $E$  can be rewritten as :

$$E = -\mu_0 H_a M_s \times [a_{x'} \cos(\alpha) \cos(\beta) + a_{y'} \cos(\alpha) \sin(\beta) + a_{z'} \sin(\alpha)] + \frac{1}{2} \mu_0 M_s^2 [N_{x'} \cos^2(\alpha) \cos^2(\beta) + N_{y'} \cos^2(\alpha) \sin^2(\beta) + N_{z'} \sin^2(\beta)] \quad (3.9)$$

By solving the two partial differential equations below, we can determine  $\alpha$ ,  $\beta$  and hence the direction of  $\vec{m}$ .

$$\begin{aligned} \frac{\partial E}{\partial \alpha} = -H_a [-a_{x'} \cos(\beta) \cos(\alpha) - a_{y'} \sin(\beta) \sin(\alpha) + a_{z'} \cos(\alpha)] + \\ M_s \sin(\alpha) \cos(\alpha) [-N_{x'} \cos^2(\beta) - N_{y'} \sin^2(\beta) + N_{z'}] = 0 \end{aligned} \quad (3.10)$$

$$\begin{aligned} \frac{\partial E}{\partial \beta} = -H_a [-a_{x'} \cos(\alpha) \sin(\beta) - a_{y'} \cos(\alpha) \cos(\beta)] + \\ M_s \cos^2(\alpha) \sin(\beta) \cos(\beta) [-N_{x'} + N_{y'}] = 0 \end{aligned} \quad (3.11)$$

### Determination of the demagnetising factor for each section of the bridge

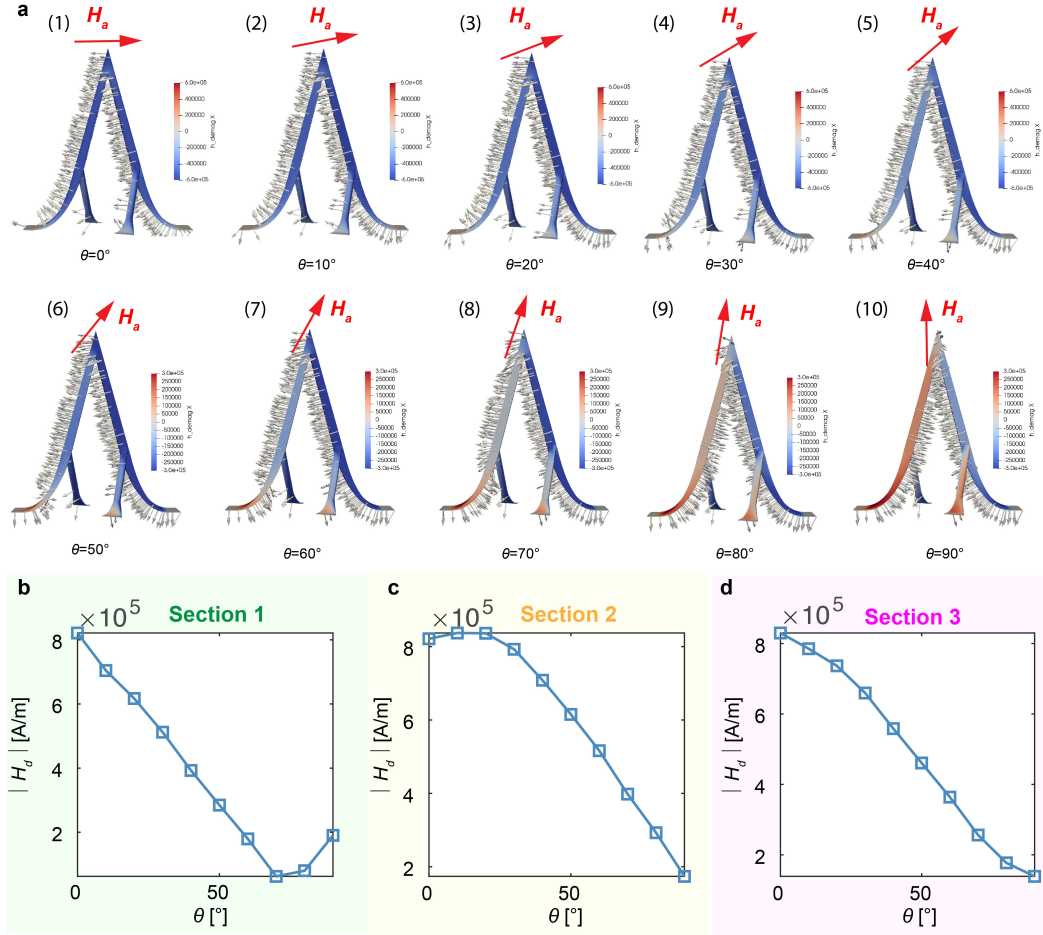


Fig. 3.12 *Magnum.fe* simulations of the demagnetising field  $\vec{H}_d$  for  $\vec{H}_a$  applied in different directions. (a) The grey arrows indicate the direction of  $\vec{H}_d$  (note that the lengths of the arrows do not represent the magnitude of the demagnetising field) and the blue-red colour scale indicates the x-component of the  $\vec{H}_d$ . (b)-(d) The averaged magnitude of  $\vec{H}_d$ , from the simulation for the three sections marked in **Figure 3.10**

To apply the macrospin model of a single nanowire of the nanobridge, we assume the bridge is made up of three single-domain nanowires as shown in **Figure 3.10**. Now, we need to determine the demagnetising factor for each wire. To get a reasonable estimation of the demagnetising factor for each wire, we have simulated the demagnetising field  $\vec{H}_d$  for fields applied from  $\theta = 0^\circ$  to  $\theta = 90^\circ$  using a finite element method based micromagnetic simulation, the *magnum.fe* package [56]. This simulation was performed by Dr Class Abert from the University of Vienna. The saturation magnetisation,  $M_s$ , used in this simulation is 1.67 T [38], and the results are shown in **Figure 3.12 a**. The grey arrows indicate the

direction of  $\vec{H}_d$  and the colour scale represents the x-component of  $\vec{H}_d$ .

We also plot the average magnitude of  $\vec{H}_d$  in each section of the bridge in **Figure 3.12 b-d** to get a general idea on the distribution of the demagnetising field. For section 1 (**Figure 3.12 b**), the minimum of  $|\vec{H}_d|$  occurs at  $\theta = 70^\circ$ . As shown in **Figure 3.12 a(8)**,  $\vec{H}_a$  is parallel to the long axis (easy) of section 1, and hence gives the smallest  $|\vec{H}_d|$ . In contrast, for section 2,  $|\vec{H}_d|$  peaks at  $\theta = 20^\circ$ , where as shown in **Figure 3.12 a(3)**,  $\vec{H}_a$  is parallel to the hard axis of section 2, leading to a maximum in  $\vec{H}_d$ . It is not immediately clear which is the easy axis for section 3 due to its unusual geometry. However, from **Figure 3.12 d**, we can get a hint that its easy axis is more aligned with the  $\theta = 90^\circ$  direction as  $|\vec{H}_d|$  decreases with increasing  $\theta$ .

To determine the demagnetising factor for each section, we plot the x, y, z components in the global coordinate system of the simulated  $\vec{H}_d$  obtained from micromagnetic simulations, against the applied field angle  $\theta$ , as a thick red line in **Figure 3.13**. We also plot the simulated  $\vec{H}_d$  from the macrospin model described in section 3.3.1 with a series of different demagnetising factors in different colours. Here, the demagnetising factors  $[N'_x \ N'_y \ N'_z]$  used correspond to the local axes in each section, and the demagnetising field is calculated in local coordinates and then converted into the global coordinates.

For Section 1 and Section 2 (**Figure 3.13 a,b**), we find that  $N = [0 \ 0.4 \ 0.6]$  (yellow line) matches the micromagnetic simulation the best. From the micromagnetic simulation, we observe that the component of the demagnetising field in the y direction is about three orders of magnitude smaller than the components in the x and z direction and hence it is not considered here. For section 3, we find  $N = [0.06 \ 0.35 \ 0.59]$  (orange line) fits best to the micromagnetic simulation as shown in **Figure 3.13 c**. For section 3, a range of  $N'_x$  from 0 to 0.1 were tested and  $N'_x = 0.06$ , which gives the best results, is plotted here.

After finding the demagnetising factor for each section, the multi-macrospin model is used to determine the magnetisation  $\vec{M}$  and demagnetising field  $\vec{H}_d$  for external magnetic fields applied in different directions. These data are then used in the FEM analysis for the MT signal calculations. This approach is sufficient to fully understand the MT signals from the nanocircuit under the application of high magnetic fields, which will be shown in **section 3.3.3**.

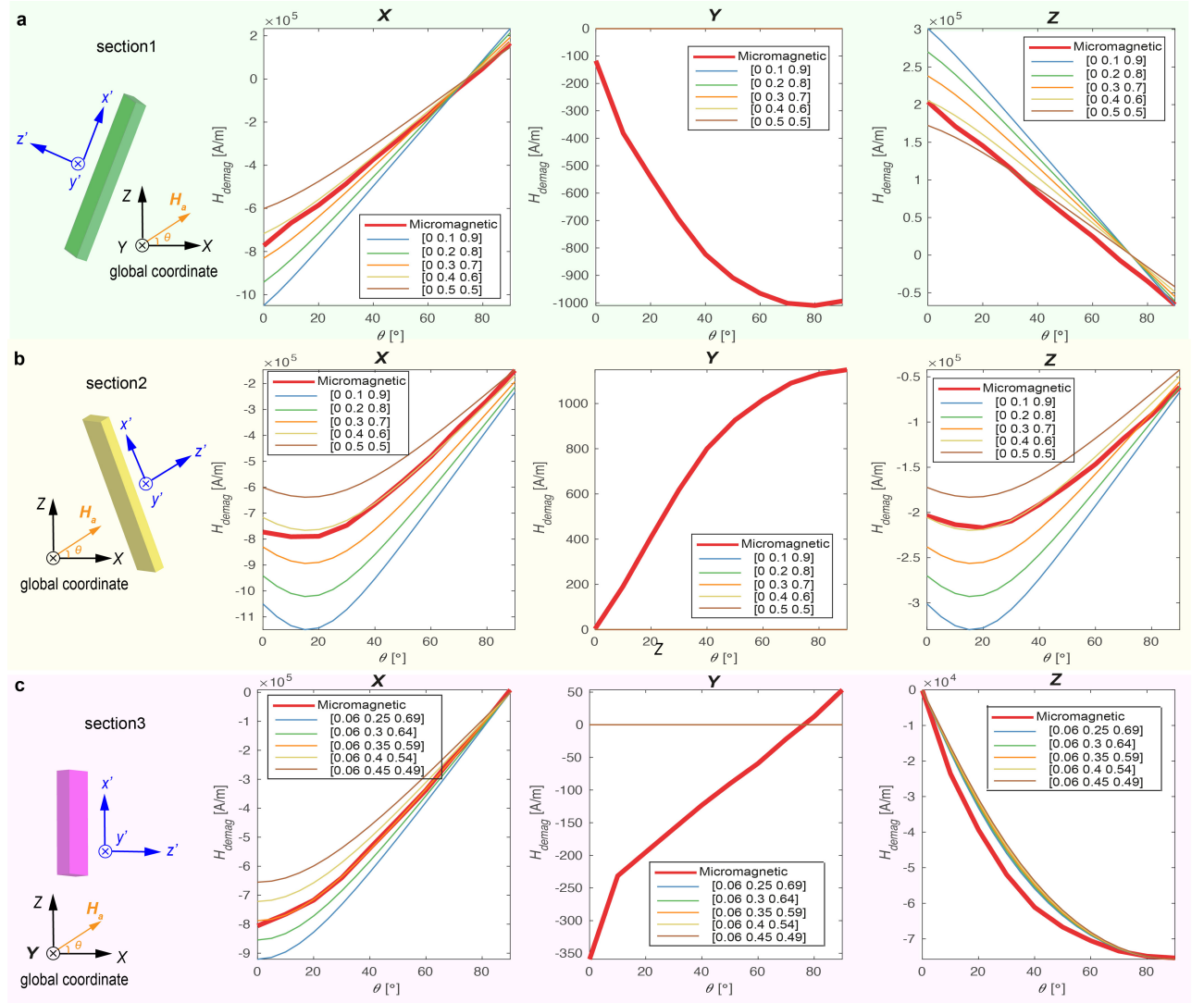


Fig. 3.13 Comparison of the averaged  $x$ ,  $y$ ,  $z$  components of the demagnetising field,  $\vec{H}_d$ , obtained from macrospin and micromagnetic simulations in (a) Section 1 (b) Section 2 (c) Section 3. For each section, the demagnetising field of micromagnetic simulations is given in red and used to identify the optimal demagnetising factor for the structure.

### 3.3.2 MT signals simulation using finite element method

#### Equation to solve and boundary conditions

To calculate the MT signal, we assume a constant steady current is supplied to the bridge, hence the current is conserved as

$$\nabla \cdot \vec{J} = 0. \quad (3.12)$$

The current in cobalt is governed by the Ohm's law as

$$\vec{J} = \sigma \vec{E}, \quad (3.13)$$

and the electric field is defined as the gradient of the electric potential  $u$ ,

$$\vec{E} = \nabla u. \quad (3.14)$$

Hence, we can rewrite the current conservation equation as

$$-\nabla \cdot (\sigma \nabla u) = 0, \quad (3.15)$$

and solve the electric potential  $u$ , using the FEM method. The resistivity tensor ( $\sigma^{-1}$ ) used is described in Equation 3.3.

We assume a constant current of 1 A flowing into the bridge through Face 1 and out of the bridge through Face 2, as shown in **Figure 3.14 a**. Thus, the current flowing in and out of the nanobridge is set using Neumann boundary conditions as  $\vec{n} \cdot (\sigma \nabla u) = -J_{in}$  or  $J_{out}$ , respectively. Here  $\vec{n}$  is the outward unit normal and  $J_{in} = J_{out} = 1A/(500nm \times 100nm)$  is the current density at Face 1 and 2. Secondly, we set the electric potential to be 0 at Face 2, as a Dirichlet boundary condition  $u = 0$ . Finally, for all other Faces in this model, we set  $\vec{n} \cdot (\sigma \nabla u) = 0$ , as no current flows in or out of the model through other Faces. Finally we can measure the voltage at side contacts and process it in the same as we process the data.

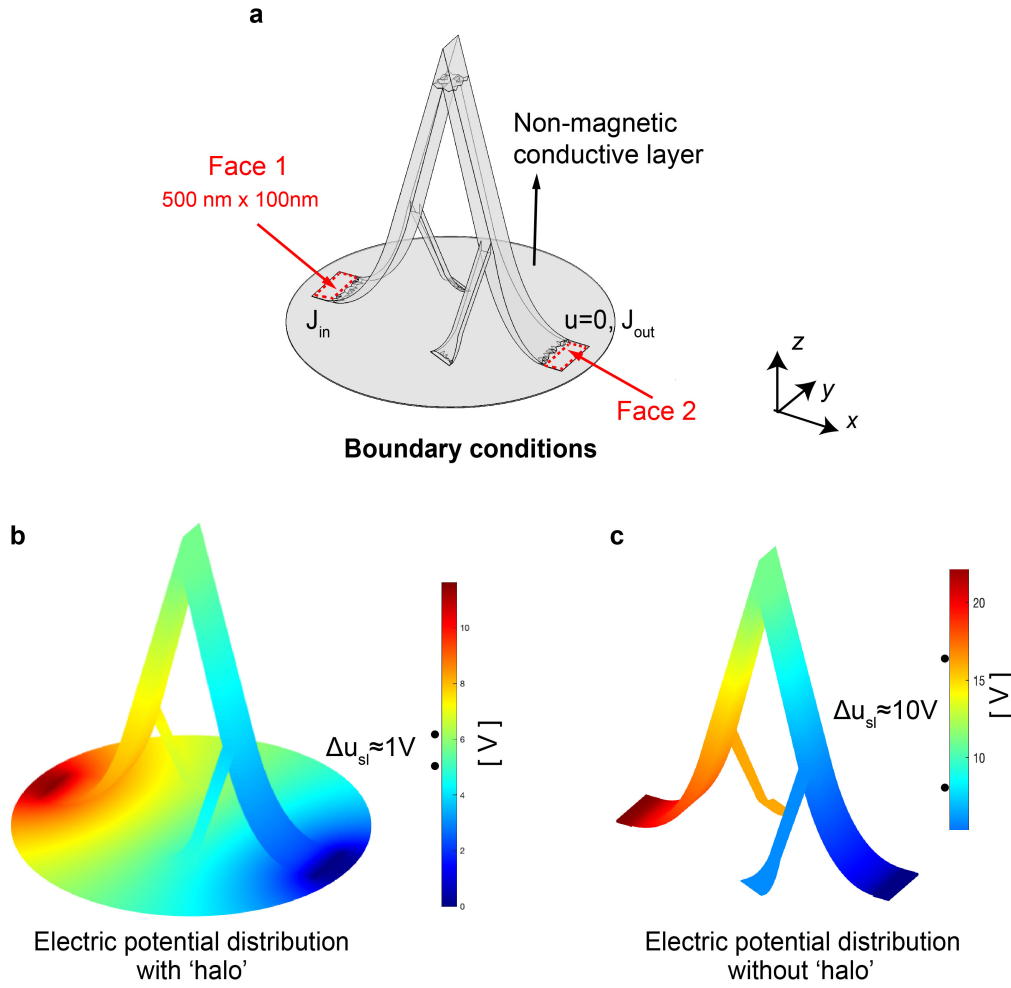


Fig. 3.14 *FEM simulation. (a) Boundary conditions. (b) Simulated electric potential distribution with a conductive layer underneath the bridge. (c) Simulated electric potential distribution for the bridge only.*

### Materials properties used and unintended deposition around the 3D nanobridge

The 3D nanobridge is deposited by FEBID with 30 kV acceleration voltage and 0.34 nA beam current using  $\text{Co}_2(\text{CO})_8$  as precursor. Similar growth conditions as the ones used here for 2D deposits lead to a metallic nanocrystalline material, formed by cobalt crystals with typical sizes around 5-10 nm, and atomic percentages of  $\approx 90\text{-}95\%$  Co [39, 38]. In our case, the larger beam currents in combination with a 3D geometry both enhance the local heating [101], which is likely to promote higher Co purity via autocatalytic effects [40, 102], enhancing the electrical conduction properties of the material. Local heating during 3D growth is also likely to enhance the Co content, crystallinity, and magnetic properties [103]. Taking into account the lowest resistivity value reported so far for FEBID, is



26  $\mu\Omega\text{cm}$  [102], and the typical resistivity of polycrystalline cobalt thin films deposited by conventional physical vapour deposition methods is, 11  $\mu\Omega\text{cm}$  [98, 104–106], we thus expect the resistivity of the probed region of the nanobridge to be in the range of 11–26  $\mu\Omega\text{cm}$ .

We first substitute the resistivity  $\rho_{Co} = 11\mu\Omega\text{cm}$  into the bridge model shown in **Figure 3.14 c**, which gives a simulated voltage across the side contacts of about 10 V, which is 10 times larger than the resistance experimentally measured. Since the resistivity of FEBID Co is not likely to be smaller than the resistivity of polycrystalline cobalt thin films, this small measured resistance is attributed to an unintended deposition (‘halo’) around the desired 3D nanostructure. This ‘halo’ effect is caused by precursor dissociation by secondary and backscattered electrons reaching distances far beyond the primary electron beam, a common effect in FEBID [107]. This indicates the FIB milled trenches explained in the **section 3.1.2** did not completely prevent the influence of this ‘halo’. Since this parasitic deposit is reported to have low cobalt concentration [108, 109, 99], here it is modelled as a non-magnetic, circular, 10-nm-thick thin film as shown in **Figure 3.14 a**. With this ‘halo’ included in the FEM model, the simulated resistance is reduced by approximately a factor of 10, and we reach a good quantitative agreement between experiments and simulations by using  $\rho_{Co} = \rho_{halo} = 15\mu\Omega\text{cm}$  (**Figure 3.14 b**).

### 3.3.3 Interpretation of magnetotransport measurements at high fields

After setting up the MT simulation tool as described in **section 3.3.1** and **section 3.3.2**, we can now use it to achieve a quantitative understanding of the 3D magnetoelectrical signals by comparing the odd and even-in-field data respectively with the simulation that considers different MT effects.

#### Odd-in-field data

The angular dependence of the odd signal is examined by plotting the average of  $|R_{odd}(4\text{ T})|$  and  $|R_{odd}(-4\text{ T})|$  with respect to the  $\theta = 0^\circ$  case (squares in **Figure 3.15 a**), together with the simulated odd signals that consider AHE, OHE or both (lines in **Figure 3.15 a**). There is a continuous increase in the magnitude of the odd component as the field rotates from  $\theta = 0^\circ$  to  $\theta = 90^\circ$ , and a good agreement between the simulation and the data, confirming that the odd signal is due to a combination of the dominating AHE and the smaller OHE [38].

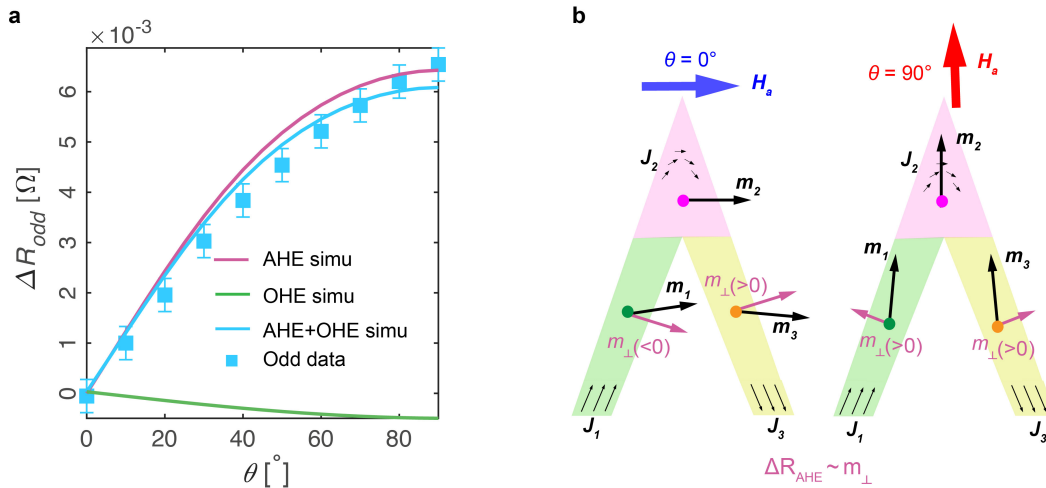


Fig. 3.15 (a) Comparison between the angular dependence of the odd part data and the AHE and OHE simulation. (b) Averaged magnetisation vectors,  $\vec{m}_1(\theta)$ ,  $\vec{m}_2(\theta)$  and  $\vec{m}_3(\theta)$  for three sections for  $\theta = 0^\circ$  and  $\theta = 90^\circ$  and their components on the current normal directions. Reproduced from [61]

We first consider the dominant contribution of AHE. The increasing trend of AHE magnitude is intuitively understandable by considering the  $\theta = 0^\circ$  and  $\theta = 90^\circ$  cases as shown in **Figure 3.15 b**. The magnetization vector  $\vec{m}$  calculated for each section from the macrospin model and its component of on the current-normal direction ( $m_{\perp}$ ) are plotted. As the AHE depends on  $m_{\perp}$  [60], at a first glance it might appear that the  $\theta = 0^\circ$  case would result in a larger AHE effect, as the magnitude of  $m_{\perp}$  is larger for green and yellow sections.

However, the different current paths result in  $m_{\perp}$  with opposite signs for these two sections, and therefore the two AHE signals cancel out. Using analogous arguments for the pink region, the current turns its direction along this section, also resulting in a negligible AHE signal. The opposite scenario occurs at  $\theta = 90^\circ$ , where the same sign of  $m_{\perp}$  for all three sections leads to the signals adding up.

This slightly unexpected angular dependence of AHE originates from the 3D current path which has components in both  $x$  and  $z$  direction (**Figure 3.16**). This makes the AHE being sensitive to both  $m_x$  and  $m_z$ , and thus making it possible for AHE to cancel out, as is seen at  $\theta = 90^\circ$ . This contrasts with both 2D nanostrip and V-shape structures, where due to the planar current distribution, the AHE only probes a single component (in this case  $m_z$ ) of the magnetisation. This is a key difference that sets this type of 3D spintronic devices apart from their 2D counterparts. Moreover, we only measured this effect because we were able to place the voltage probes at both sides of the bridge across the width direction. This is also a good example to illustrate the advantages of 3D structures in device connectivity.

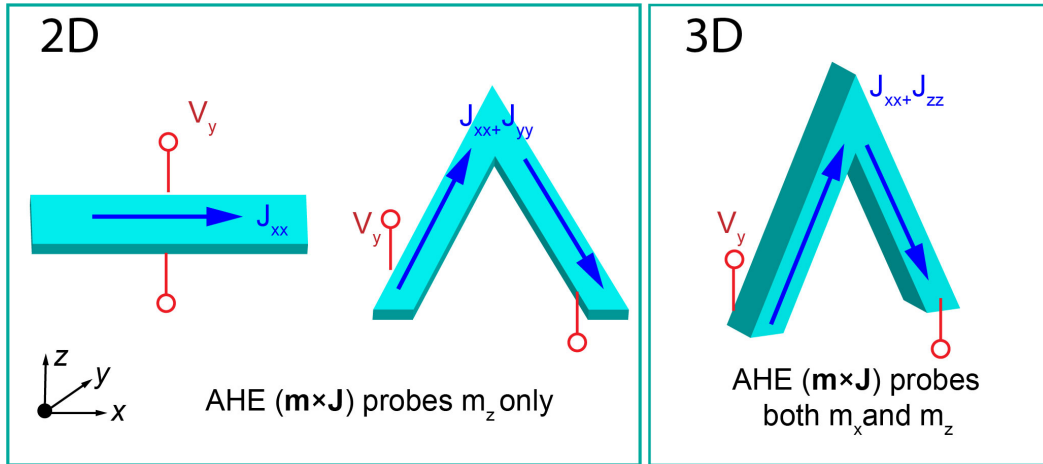


Fig. 3.16 Arrangements of voltage probes in different situations (a) 2D wire (b) 2D v-shape (c) 3D v-shape

Since the total induction  $\vec{B}$  is parallel to  $\vec{m}$ , the magnitude of the OHE follows the same trend as the AHE, which explains why the negative linear slope is the most obvious at  $\theta = 90^\circ$  in **Figure 3.9 c**. From the model fitting, we find  $\rho_{AHE} = 5.6 \times 10^{-9} \Omega\text{m}$  and  $R_{OHE} = -1.2 \times 10^{-10} \Omega\text{m/T}$ , of the same range as the anomalous Hall resistivity and ordinary Hall coefficient reported in the literature for FEBID-deposited cobalt [38].

### Even-in-field signal

For the even part of the signal, we plot the average of  $|R_{\text{even}}(4\text{T})|$  and  $|R_{\text{even}}(-4\text{T})|$  with respect to the  $\theta = 0^\circ$  case as squares in **Figure 3.17a**. We observe a general decreasing trend with a peak at around  $\theta = 30^\circ$ . We first examine what are commonly considered the main intrinsic contributions to the even signal: the AMR and PHE. The simulated sum of AMR and PHE signals (referred for brevity as AMR) is plotted in **Figure 3.17 a** (purple line), which takes the form of a monotonic increase in the resistance with increasing  $\theta$ . The AMR ratio = 0.95% reported in the literature for FEBID-deposited cobalt [38] is used here. Again, we can explain the angular dependence of AMR by considering  $m_{\parallel}$  at  $\theta = 0^\circ$  and  $\theta = 90^\circ$  (**Figure 3.17 b**).  $m_{\parallel}$  is larger at  $\theta = 90^\circ$ , so we would expect the AMR to be larger at  $\theta = 90^\circ$ , consistent with the simulated signal. However, the experimental data exhibit a very different angular dependence, implying that AMR is not the only contribution.

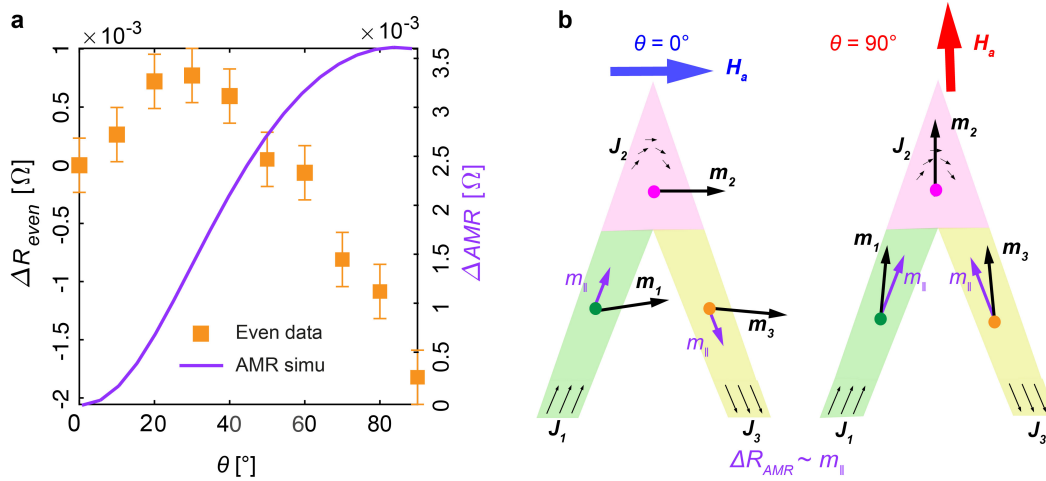


Fig. 3.17 (a) Comparison between the angular dependence of the even part of the data and the AMR simulation. (b) Averaged magnetisation vectors,  $\vec{m}_1(\theta)$ ,  $\vec{m}_2(\theta)$  and  $\vec{m}_3(\theta)$  for three sections at  $\theta = 0^\circ$  and  $\theta = 90^\circ$  and their components on the current direction. Reproduced from [61].

To understand the significant difference between the AMR simulation and the even part of the signal, we examine the angular dependence of magnon magnetoresistance as an additional contribution. The change of resistivity due to MMR can be described by the electron-magnon scattering model developed by Raquet *et al* [59]:

$$\Delta \rho_{\text{mmr}}(T, B) \approx \rho(T, B) - \rho(T, 0) \propto \frac{BT}{D(T)^2} \ln \left( \frac{\mu_{\text{Bohr}} B}{k_B T} \right), \quad (3.16)$$

where  $T$  is the temperature,  $D(T)$  is the temperature dependent magnon stiffness,  $\mu_{Bohr}$  is the Bohr magneton,  $k_B$  is the Boltzmann constant, and  $B$  is the projection of the total effective magnetic field,  $\vec{B} = \mu_0(\vec{H} + \vec{M})$ , on the direction of the magnetization, *i.e.*, the magnitude of the total effective field, acting to suppress the magnitude of spin-waves present in the system. Here  $\vec{H}$  is the vector sum of the applied field  $\vec{H}_a$  and demagnetizing field  $\vec{H}_d$ ,  $\vec{H} = \vec{H}_a + \vec{H}_d$ , and  $M$  is the magnetization.

According to Equation 3.16, MMR leads to a negative change of resistivity at constant temperature that decreases almost linearly with the magnitude of the effective field, which is consistent with the even part of the experimental signal for applied fields greater than 2 T (**Figure 3.9d**). Unlike AMR or AHE,  $\Delta\rho_{mmr}$  is not dependent on the direction of the magnetization with respect to the current but only on the magnitude of the total effective field. However, this does not necessarily imply that no change will occur in the  $\Delta\rho_{mmr}$  as a result of changing directions of the applied magnetic field. Previous studies investigating the contribution of MMR in nanostructures have mainly focused on measurements under fields applied along the easy axis of 2D thin films or nanowires, where the demagnetizing field is negligible, leading to an effective field equivalent to the applied field [59, 110]. However, in the case of a non-planar 3D nanocircuit like the one analysed here, the applied field is always oblique to at least one component of the circuit. As a result, a non-zero demagnetizing field exists, which modifies the effective magnetic field at any angle.

The change of resistance due to MMR is calculated by including the  $\Delta\rho_{mmr}$  term in the resistivity tensor as shown in Equation 3.17.

$$\rho(\vec{m}, \vec{B}) = \begin{pmatrix} \rho_{\perp} + \rho_G m_x^2 + \Delta\rho_{mmr} & \rho_G m_x m_y - \rho_{AHE} m_z - R_{OHE} B_z & \rho_G m_x m_z + \rho_{AHE} m_y + R_{OHE} B_y \\ \rho_G m_x m_y + \rho_{AHE} m_z + R_{OHE} B_z & \rho_{\perp} + \rho_G m_y^2 + \Delta\rho_{mmr} & \rho_G m_y m_z - \rho_{AHE} m_x - R_{OHE} B_x \\ \rho_G m_x m_z - \rho_{AHE} m_y - R_{OHE} B_y & \rho_G m_y m_z + \rho_{AHE} m_x + R_{OHE} B_x & \rho_{\perp} + \rho_G m_z^2 + \Delta\rho_{mmr} \end{pmatrix}, \quad (3.17)$$

$\Delta\rho_{mmr}$  can be obtained using Equation 3.16 with the total effective calculated from our macrospin model. The resultant change of MMR is plotted as a black line in **Figure 3.18 a**. An opposite trend in the angular dependence of MMR with respect to the AMR is observed, with the resistance becoming more negative with increasing angle. Again, we consider the extreme cases of  $\theta = 0^\circ$  and  $\theta = 90^\circ$  in **Figure 3.18 b** to understand this angular dependence intuitively. At  $\theta = 0^\circ$ , the applied field has a larger component perpendicular to each section's

easy axis, resulting in a larger demagnetising field, and thus a lower magnitude of the overall effective magnetic field, leading to a higher resistance. At  $\theta = 90^\circ$ , the field is more aligned with the easy axes for all three sections, leading to a lower demagnetising field, and a larger magnitude of the total effective field, associated with a larger drop of resistivity, as seen in the simulated data. In the MMR calculation, the temperature dependent magnon stiffness  $D(180\text{K}) = 390 \text{ meV\AA}$ [59] was used. Since the magnon scattering model developed by Raquet et al. only indicates the proportionality, but not the absolute magnitude of  $\Delta\rho_{mmr}$ , a factor of 15 is used to produce the best fit to the data.

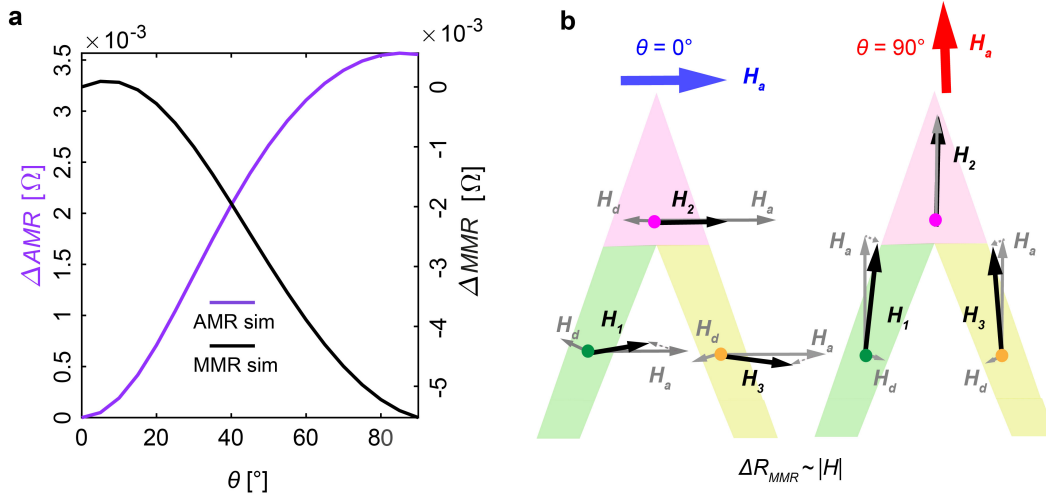


Fig. 3.18 (a) Simulation of the AMR and MMR effects (b) Applied field,  $\vec{H}_a$ , demagnetising field,  $\vec{H}_d$  and their vector sum  $\vec{H}$  for each section of the bridge. Reproduced from [61].

Finally, we compare the sum of AMR and MMR obtained from simulations (**Figure 3.19**, orange line), to the even data (**Figure 3.19**, squares). An excellent agreement with experiments is observed, with the maximum resistance at around  $\theta = 30^\circ$ , and the overall angular trend well reproduced. This demonstration of the strong influence of the three-dimensional geometry on the magnetotransport reveals the importance of non-collinear alignments between magnetic fields and geometry in non-planar magnetic nanocircuits. In particular, this work demonstrates how magnetostatic interactions in 3D geometries manifest through a significant deviation of the MMR contribution.

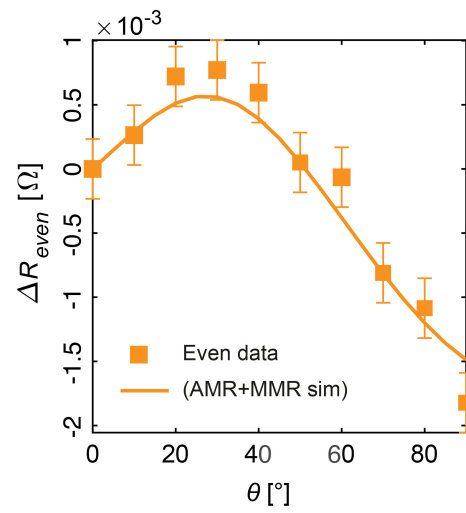


Fig. 3.19 Comparison between the sum of AMR and MMR simulations and the even data. Reproduced from [61].

### 3.4 Chapter Summary

In this chapter, we first demonstrate the realisation of a 3D nanomagnetic circuit that allows four probe measurements on a relatively complex 3D nanomagnets by employing an advance 3D-nanoprinting technique, FEBID. We study the magnetoelectrical response of this circuit and exploit signal symmetries and angular dependence with respect to magnetic field configurations to address the superposition of different magnetotransport effects. Specifically, in addition to the fully detailed MT measurements, we use multi-macrospin and finite-element calculations to disentangle and understand key magnetotransport effects including Hall effects and magnetoresistance signals, obtaining a clear understanding of their magnitudes and angular dependencies as a function of the field direction.

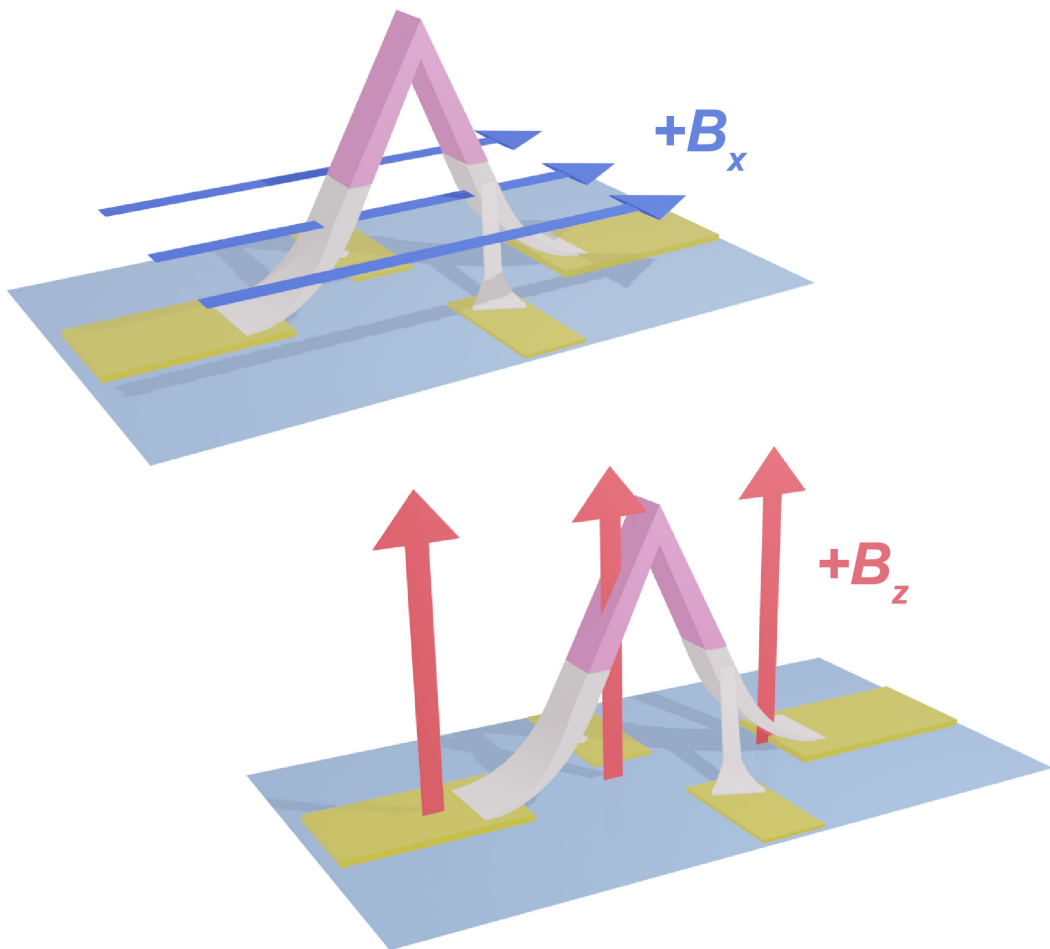
We identified that the 3D geometry of the magnetic nanostructure has influenced the magnetoelectrical signals in two major ways. First, the 3D vector nature of both  $\vec{m}$  and  $\vec{J}$  induces deviations of Hall effect signal from the familiar angular dependence usually observed in planar geometries, due to the fact that signals that, e.g., cancel out in planar geometries may add up in 3D. Second, the overall magnetoelectrical signal has a significant angular-dependent magnon contribution, due to varying magneto-static interactions throughout a 3D circuit which are not present in a standard planar magnetic device.

This study shows the potential of using 3D magnetic devices to create magnetotransport responses with complex angular dependence external magnetic fields. It also provide insights into the influence of a 3D geometry on the magnetotransport effects, constituting the basis for exploring complex spintronic effects emerging in three dimensions. Long-term, it is an important step towards the realisation of 3D devices. The methodology shown here combining FEBID 3D printing with standard planar lithography can be extended to more complex 3D geometries and other materials, leading to the fundamental study of phenomena that exploit the interplay between 3D geometry and magnetotransport.



## Chapter 4

### Magnetisation reversal processes in a 3D cobalt nanobridge



## Introduction

The understanding of magnetisation reversal processes in 3D nanostructures, their electrical responses, identification of magnetic states and field driven transitions are critical, especially with respect to the use of 3D nanomagnets in sensing, memory and information processing applications [17, 22]. In the previous chapter, we took the advantage of the fact that, at high fields, the magnetisation profile is nearly uniform and employed an angular dependence study on magnetic fields and a multi-macrospin model to analyse the influence of 3D geometry on different magnetotransport effects. Building on our understanding of these effects and their corresponding parameters, in this chapter, we aim to investigate the magnetisation reversal process of the same 3D nanobridge from magnetotransport measurements.

Compared to high resolution magnetic microscopies [111, 25] that are usually used for characterising rather complex magnetic states in 3D structures, magnetotransport measurements provide a fast and daily accessible way to detect magnetisation reversal. However, it is an integral measurement method and hence only provides the overall response of the section between electrical contacts. Thus, instead of direct observation of the spin textures, we can only infer possible magnetic states involved from these measurements [112, 113]. Inferring magnetic states from magnetotransport measurements is particularly challenging in our 3D nanobridge, as not only are magnetisation configurations are intrinsically more complicated due to the three dimensionality, but there are also several different effects, such as AMR, AHE, and MMR, superimposed together in the signal probed due to our diagonal-contact design as explained in the previous chapter. As a result, in addition to measuring the magnetotransport hysteresis loops, auxiliary tools such as stochastic analysis, micromagnetic simulation, and finite element modelling are also employed in this study to aid the understanding of the switching process.

In this chapter, we focus on the magnetisation reversal process of the nanobridge under field applied in two principle directions. For each direction, we first examined the characteristics of the MT hysteresis loops and then by comparing the experimental data with the micromagnetic and finite element modelling results, possible magnetisation states involved and switching routes during the switching process are proposed. This study illustrates how 3D devices, such as the nanobridge studied, are susceptible to external magnetic fields in multiple directions [17, 43], resulting in different features in MT responses that are appealing to sensing and computing applications[8]. We also see that 3D structures generally lead to more complex magnetic states, particularly as magnetostatics becomes more important, leading typically to swirling states such as vortices [50, 114].

## 4.1 Magnetisation reversal process in $x$ -direction

In this section, we investigate the magnetisation reversal processes of the bridge under field applied in  $x$ -direction which is parallel to both the substrate and the bridge as illustrated in **Figure 4.1**. The same coordinate system is used here as in the previous chapter and this direction corresponds to the  $\theta=0^\circ$  case in the high-field study. Full magnetotransport (MT) hysteresis loops were measured from + 2.5 T to -2.5 T and from -2.5 T to 2.5 T. For the non-transition area ( $|\mu_0 H_x| > 0.5$  T), a fast field sweep rate of 0.05 T/s was used and the resistances was measured at 0.5 T steps, whereas a slow sweep rate of 0.5 mT/s was used to observe detailed switching over regions where interesting magnetic phenomena occur ( $|\mu_0 H_x| < 0.5$  T) and the resistance was measured at 1 mT steps. All the electrical measurement settings used were the same as those used in the high-field study presented in the previous chapter and hence are not repeated here.

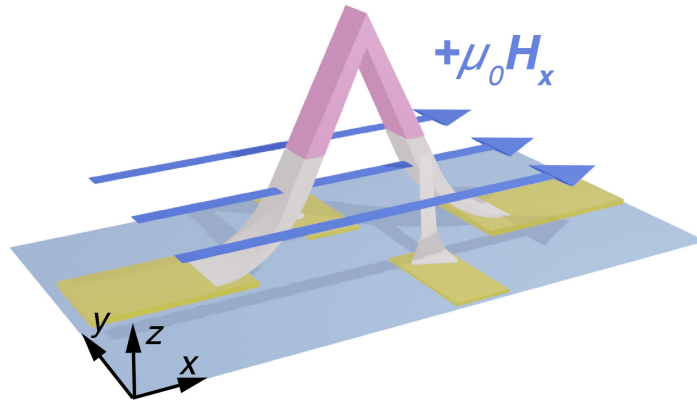


Fig. 4.1 Schematic of applied field configuration with respect to the 3D nanobridge. Field is applied in the positive  $x$ -direction.

Since the stochasticity of a switching event usually reveals the underlying reversal mechanism [115–117], to gain more insights into the reversal process, we repeated the measurement of a full hysteresis loop 16 times. The average of these 16 cycles is presented in **Figure 4.2** to introduce the general trend of the signal first and the details of each cycle will be analysed later.

### 4.1.1 Analysis of the experimental MT hysteresis loops

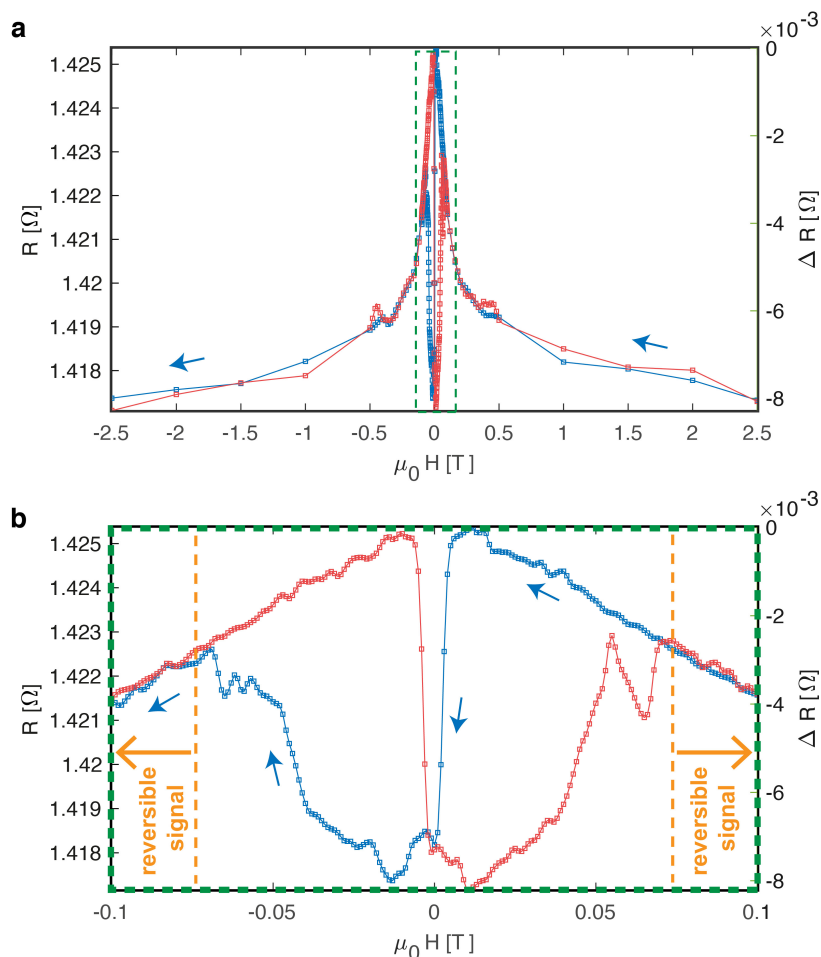


Fig. 4.2 Magnetoresistance hysteresis loop (16 averages) for field applied in  $x$ -direction. (a) Full hysteresis loop between  $-2.5$  T and  $2.5$  T (b) Zoom-in region between  $-0.1$  T to  $+0.1$  T. The right y-axis plots the relative change of resistance with respect to the maximum.

#### Averaged MT hysteresis loop

To begin analysing the experiment data, we examine the average plot of 16 full MT hysteresis loops to obtain an overview of how MT signals change with applied field (**Figure 4.2 a**). The forward sweep (from  $+2.5$  T to  $-2.5$  T) was plotted in blue, while the backward sweep (from  $-2.5$  T to  $+2.5$  T) was plotted in red, and the details between  $\pm 0.1$  T (green dash box) are shown in **Figure 4.2 b**. The first thing to notice is that the forward and backward sweeps are symmetric about  $\mu_0 H_x = 0$  T, indicating that even-in-field effects such as AMR and MMR dominate the signal. This symmetry at high fields has already been explained in

the  $\theta=0^\circ$  case in the high-field study, as odd-in-field effects such as AHE and OHE from two legs of the bridge cancel out each other due to different current directions [61]. Then, taking the forward sweep (blue line) as an example, as the field decreases from 2.5 T, the resistance gradually increases to a maximum. This can be understood as at lower fields, the magnetisation tends to align along the long axes of the bridge due to shape anisotropy, which coincides with the current direction for this geometry. The resistance is the greatest when the magnetisation coincides with the current direction due to the AMR effect given that cobalt has a positive AMR ratio [38] while the AHE effect is negligible. Also, as the magnitude of the applied field decreases, so does the drop in resistance caused by MMR [61]. For  $\mu_0 H_x > 0.075$  T (marked by the yellow dash line in **Figure 4.2 b**), the MT signal is reversible as the forward and backward sweep overlap on each other suggesting magnetic moments reverse coherently in this range.

For  $\mu_0 H_x < 0.075$  T, the MT signal becomes irreversible, and this is the region which we will focus more in this chapter. After the resistance reaches a maximum value, a significant drop is observed. The magnitude of this drop is surprisingly large ( $\approx 8$  m $\Omega$ ) and is of comparable size with the total increase of resistance as the field sweeps from +2.5 T to  $\approx 0$  T. This size of the drop indicates that the bridge is unlikely to be switched via domain wall (DW) propagation, because local texture changes such as DWs should not induce a change equivalent to aligning almost all magnetic moments in the  $x$ -direction under a 2.5 T field. Aside from the magnitude, the second distinctive feature of this drop is its sharpness, given that the plot is the result of an average of 16 cycles, this suggests that the drop is also very reproducible. Finally, the resistance climbs back gradually before dropping again as the field increases in the opposite direction.

### Analysis of switching events in all 16 cycles

After having discussed the general pattern of the full-range MT hysteresis loops revealed by the average plot, we now examine all 16 individual cycles in the irreversible range in order to gain more information about the switching events. For an overview, we plotted all 16 cycles together with their average (thicker lines) as shown in **Figure 4.3**. Forward and backward sweeps are plotted separately from now on, allowing a clearer observation of details in curves. Though there are some variations in the MT loops, the overall behaviour is the one previously discussed in the averaged curve, characterised by a significant drop at around 0 T.

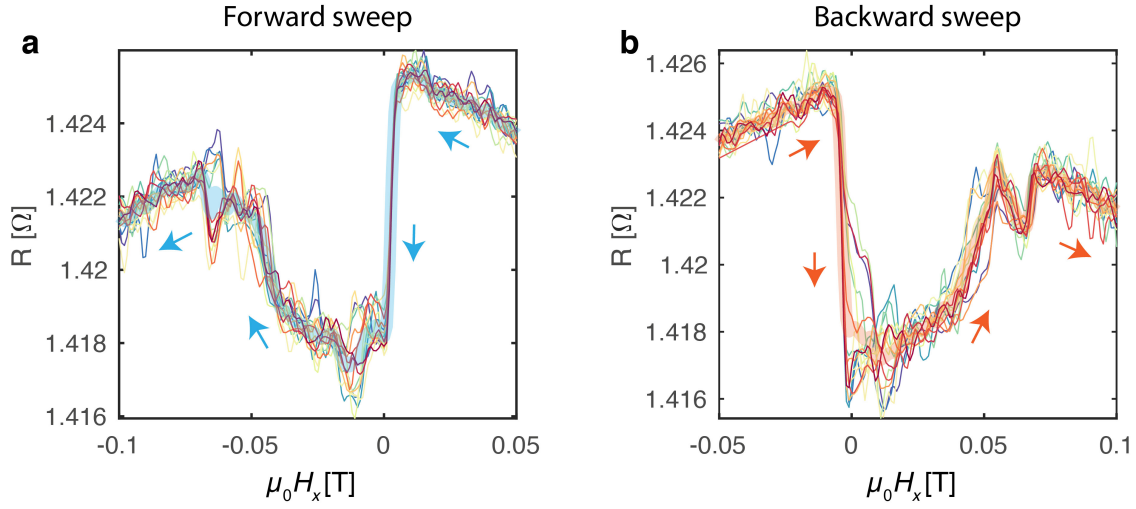


Fig. 4.3 All 16 MT loops measured for field applied in the  $x$ -direction. The thicker line represents the average of the 16 cycles. (a) Forward sweeps. (b) Backward sweeps.

To infer the behaviour of the system for the low-field range, we defined two switching events for both forward and backward sweeps as shown by the red and green arrows in **Figure 4.4 a** and **b**. Specifically, we study the range of data where significant transitions occur (from +0.05 to -0.1 T and from -0.05 to +0.1 T for forward and backward sweeps, respectively), and identify two switching fields (marked by the red and green vertical lines) where the mean of the resistance changes most abruptly. The distribution of the switching fields for forward and backward sweeps are summarised in the form of histograms in **Figure 4.4 c** and **d**, respectively. Indeed, as predicted by the average plot, event 1 is highly deterministic, particularly in forward sweeps where they all occur at the same field. In comparison, event 2 exhibits more uncertainty in the switching fields for each cycle. The different histogram distribution for each events is a first indication that different magnetic processes are involved in these two events [118]. We also notice that in backward sweeps there is a slightly higher degree of stochasticity for both events compared to forward sweeps, which may be due to a slight misalignment of fields with respect to the  $x$ -direction.

In addition to the distribution of switching fields, we also record the resistance change ( $\Delta R$ ) associated with each switching event (**Figure 4.4 e** and **f**) by calculating the difference in the mean values of the regions separated by the switching events. (The mean of resistance of each region is marked by the horizontal lines in **Figure 4.4 a** and **b**). The drop of resistance related to event 1 ( $\approx 6$  mΩ) is nearly double the size of the change related to event 2 ( $\approx 3$  mΩ) and there is no significant difference in the standard deviation of  $\Delta R$ . For both events, the mean and standard deviation of both the switching fields and the corresponding  $\Delta R$  are

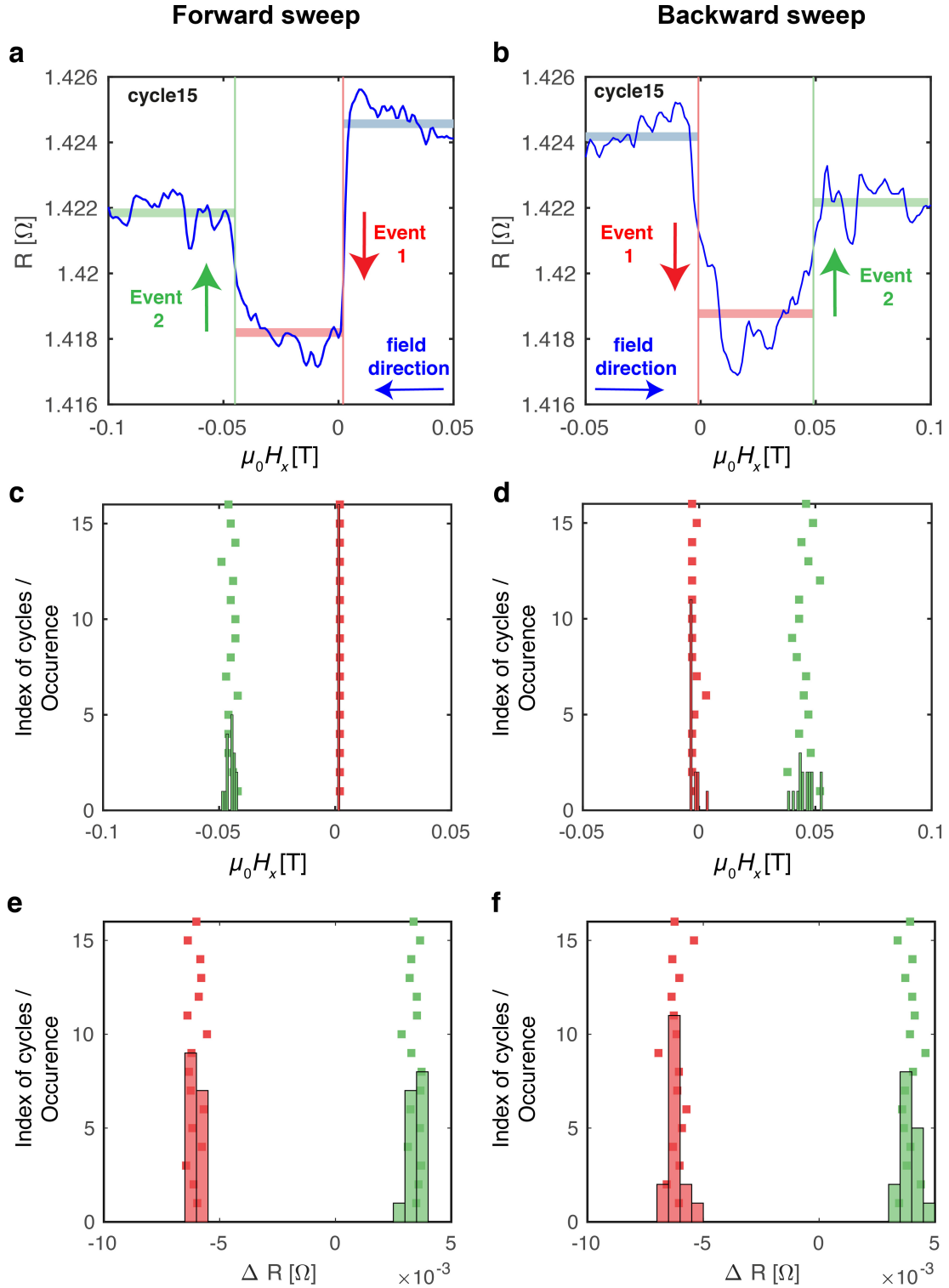


Fig. 4.4 Analysis of different switching events for all 16 cycles. The left column are plots for forward sweeps (between +0.05 and -0.1 T) and the right column are plots for backward sweeps (between -0.05 and +0.1 T). (a)-(b) Two switching events are defined. (c)-(d) Distribution of switching fields of both events. Bin width = 1 mT, which is the precision of measurement for the applied field. (e)-(f) Distribution of the resistance change in both events. Bin width = 0.5 mΩ (error in resistance measurement =  $\pm 0.25$  mΩ).

summarised in **Figure 4.5**. As we will discuss in detail in later sections, the analysis here performed complements well the study of the magnetic state for event 1 and 2 with the aid of micromagnetic and FEM modelling. This statistical analysis of the curves can be used as supportive signatures for corresponding processes and may assist in the identification of similar switching events in more complicated reversal processes, such as the case with the field applied in the  $z$ -direction, which will be presented in **section 4.2**.

$\mu_0 H_x$					
		Forward sweep		Backward sweep	
Mode		1 (16/16)		1 (16/16)	
		Event 1	Event 2	Event 1	Event 2
switching field	mean (mT)	2	-44.8	-2.3	45.3
	std ( $10^{-3}$ )	0	1.9	1.5	3.8
change of resistance	mean (m $\Omega$ )	-6.1	3.4	6.2	3.9
	std ( $10^{-3}$ )	0.27	0.24	0.33	0.31

Fig. 4.5 Summary of the switching field and change of resistance for event 1 and 2.



### 4.1.2 Micromagnetic and finite element modelling

Having performed a first analysis of the experimental data at low fields, consisting of identifying the two switching events and some statistical analysis, we now turn to micromagnetic simulation to explore the evolution of magnetic configurations during the reversal process. For quantitative comparison with the experimental MT signal, the electrical responses of these configurations are simulated using the finite element method (FEM) explained in the previous chapter. The setup of the simulation tools is introduced first.

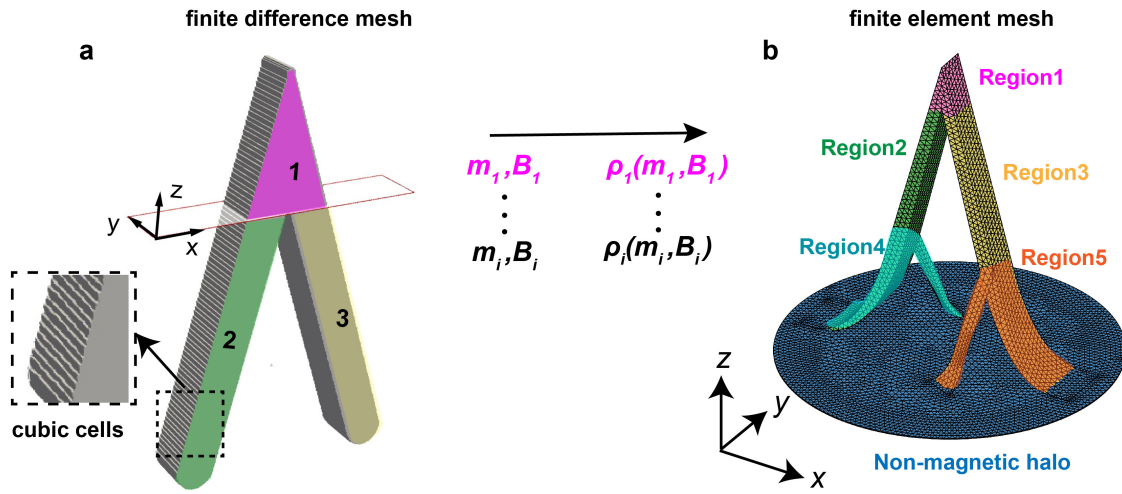


Fig. 4.6 (a) Finite difference mesh used for micromagnetic simulation. (b) FEM mesh used to simulate MT signals.

#### Micromagnetic simulation setup

As the first attempt to understand the magnetic configurations involved in the reversal process of the 3D nanobridge, we chose the MuMax3 package for its easy implementation and fast speed [55]. For now, only the top part of the bridge (region above the side-leg contacts) is considered as this geometry can be created easily by extruding 2D primitive geometries available in MuMax3. The finite difference mesh used is shown in **Figure 4.6 a**, and the dimensions of the model are designed according to the measurements obtained from the SEM images presented in **section 3.1.1**. FEBID cobalt is modelled using a saturation magnetisation  $M_s = 1.67$  T (same as in the macrospin model) and exchange stiffness  $A_{ex} = 3 \times 10^{-11}$  J/m [119]. No magnetocrystalline anisotropy is included due to the nanocrystalline nature of FEBID cobalt [120]. The dipolar exchange length of the simulated material is  $\sqrt{2A_{ex}/(\mu_0 M_s^2)} = 5.1$  nm, hence a cubic mesh size of 4 nm is employed. Magnetic fields

are applied from -2.5 T to + 2.5 T at 2 mT steps in  $x$ -direction. The mesh is divided into three regions (**Figure 4.6 a**), and the normalised averaged magnetisation ( $\vec{m}_i$ ) and the total effective field ( $\vec{B}_i$ ) of each region are exported for later calculation of the region-specific resistivity tensor  $\rho_i(\vec{m}_i, \vec{B}_i)$  for the FEM modelling of MT responses. The details of spin configurations in the whole bridge are recorded in *.vtk* files.

### FEM simulation set up for MT signal in magnetic reversal process

The setup of the FEM simulation is the same as the one introduced in **section 3.3.2** for the high-field study, *i.e.*, same mesh and boundary conditions are used. The resistivity tensor  $\rho(\vec{m}, \vec{B})$  still takes into account the same MT effects including AMR, AHE and MMR with parameters obtained from the high-field study. However, the  $\vec{m}_i$  and  $\vec{B}_i$  in the tensors are determined in a different way following some approximations described in details hereafter. In the previous high-field study, where a 4 T field was applied, we assumed the magnetisation profile in each region to be uniform, and  $\vec{m}_i$  and  $\vec{B}_i$  for each region was calculated from a macrospin model [61]. In this reversal process study, especially at low fields, the approximation of a uniform magnetisation profile does not hold anymore. However, although the spin textures may vary significantly within one region, the current density is relatively uniform across the top part of the bridge (region 1 to 3 in **Figure 4.6 b**), hence we use the averaged magnetisation across each region (directly exported from MuMax3) in the corresponding resistivity tensor for a first approximation of the MT signal.

The second thing to notice is how the smooth-ramp parts connecting the bridge to the planar electrodes (region 4 and 5 in **Figure 4.6 b**) are handled differently in the high-field and low-field regions. Since their magnetic configurations are not simulated due to the complicated geometry and significant increase in computational time, different assumptions are used for different field ranges. For  $|\mu_0 H_x| < 0.5$  T, we assume the magnetisation in these regions to follow the ramp geometry due to the shape anisotropy and thus coincide with the current profile. In this case, the AHE is negligible and the AMR effect is taken into account by treating the smooth ramps as non-magnetic parts with a resistivity equals to  $\rho_{||}$  (as a reminder,  $\rho_{||}$  is the resistivity when the current and magnetisation are aligned). For  $0.5$  T  $< |\mu_0 H_x| < 2.5$  T, however, since the experimental hysteresis loops are entirely reversible in this range, we assume the magnetisation from the smooth ramps (region 4 and 5) to follow the applied field in the same way as region 2 and 3 does, respectively. Ideally, the magnetic configurations of smooth ramps should not affect the MT signals due to the four-probe method used. However, the parasitic halo formed beneath the bridge has caused an unwanted electrical connection between voltage probes, and hence we need to take them into account.

The resistivity settings for the whole bridge, including the smooth ramps and the parasitic halo, and coefficients used for the MT effects are the same as those used in the high field study.

### Results from micromagnetic and FEM modelling

First, we compare the experimental MT results (**Figure 4.7 a**) to the simulated MT results following the aforementioned approximations (**Figure 4.7 b**) which account for the AMR, AHE and MMR effects. The breakdown of the contribution from these effects is shown in **Figure 4.7 c** and will be discussed alongside the different simulated magnetic states. In general, the simulation result reproduces the data very well, including the general symmetric pattern, the gradual increase in resistance as the field approaches 0 T and the sharp drop in resistance at  $\approx 0$  T with a magnitude at around  $\approx 6$  m $\Omega$ , which is very similar to the average drop we measured in **section 4.1.1**. A small disagreement is found regarding the switching field values, which is expected as the simulation is performed at 0 K, in contrast to experiments done at 180 K.

To understand what are the different magnetic states and their contribution to the overall simulated MT signal, six states of interest are defined, as shown by the blue squares in **Figure 4.7 b**. Their corresponding magnetic configurations are shown in **Figure 4.8 a**. For better visualisation of the 3D spin configurations, we also plot their cross-sectional view in the  $XY$ ,  $XZ$  and  $YZ$  planes in **Figure 4.8 b, c and d**, respectively. The magnetic configurations of these six states and their relationship with different MT effects are discussed as the following:

**State 1 to state 2.** As shown in **Figure 4.8 a**, the magnetisation is saturated in the  $x$ -direction in state 1 and gradually aligns along the long axis for each of the two legs of the bridge in state 2 due to shape anisotropy, except for the caps formed at the bottom of each leg and a domain wall at the region joining both. During this process, the AMR contribution gradually reaches its maximum (green line in **Figure 4.7 c**) as  $\vec{m}$  gets aligned with  $\vec{J}$  [60]. The AHE (yellow line in **Figure 4.7 c**), on the contrary, is negligible in state 1 because the contribution from each leg cancels out [61] and it remains approximately equal to zero in state 2 because there is almost no component of  $\vec{m}$  that is perpendicular to  $\vec{J}$ . Finally, because of the decreasing total effective field, the MMR (purple line in **Figure 4.7 c**) exhibits its signature linear increase as the field approaches 0 T [59].

**State 2 to state 3.** This is the step that corresponds to the sharp decrease in resistance. In **Figure 4.8 a**, we observe that the magnetic configuration of the entire bridge has changed,

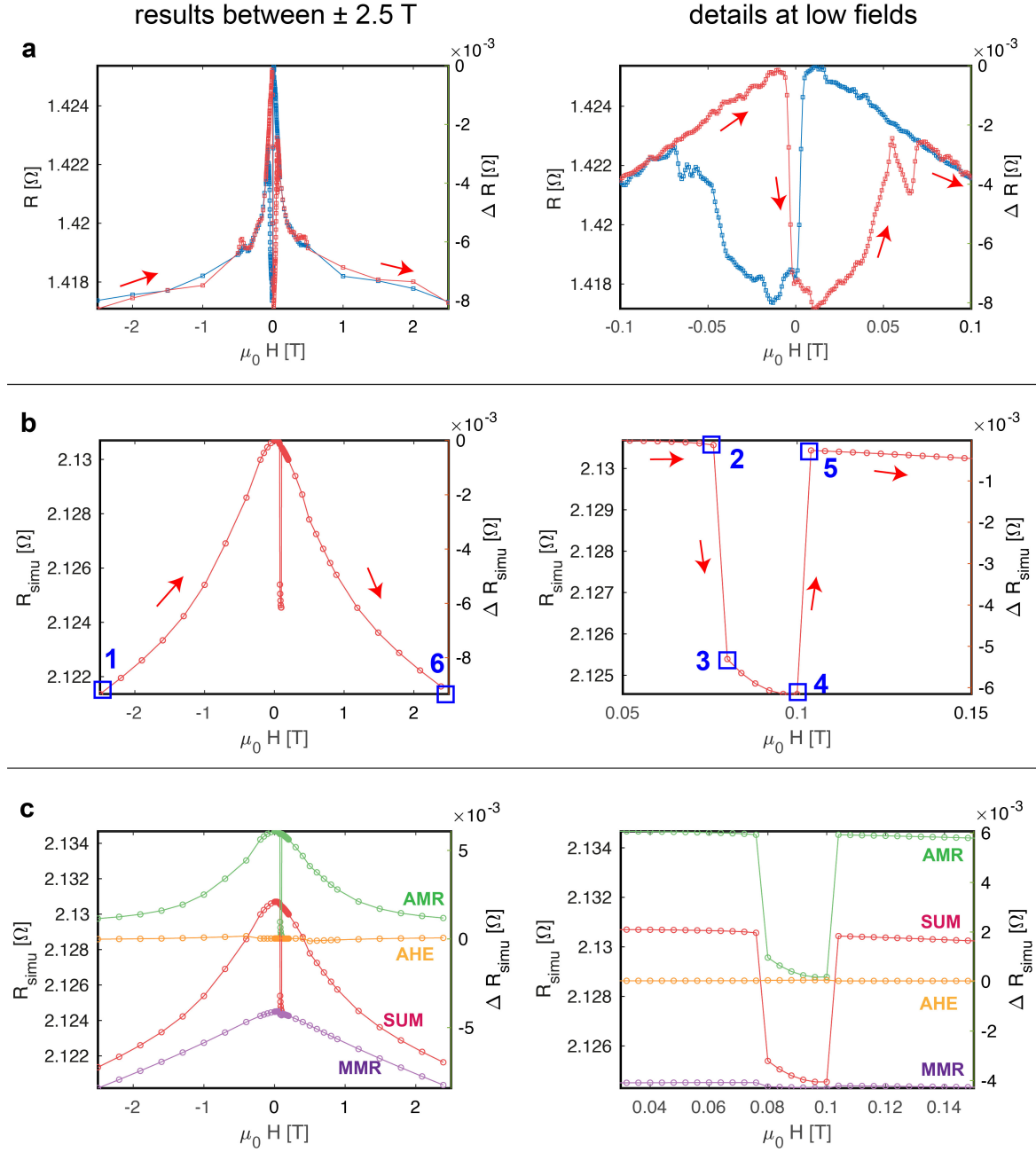


Fig. 4.7 Experiment and simulated MT results. The left column plots results for the full - 2.5 T to + 2.5 T field range. The right column plots a smaller range of fields near 0 T. (a) The experimental MT hysteresis loops. (b) The simulated MT hysteresis loops that considers all effects including AMR, AHE, and MMR. (c) The simulated contribution from different effects.

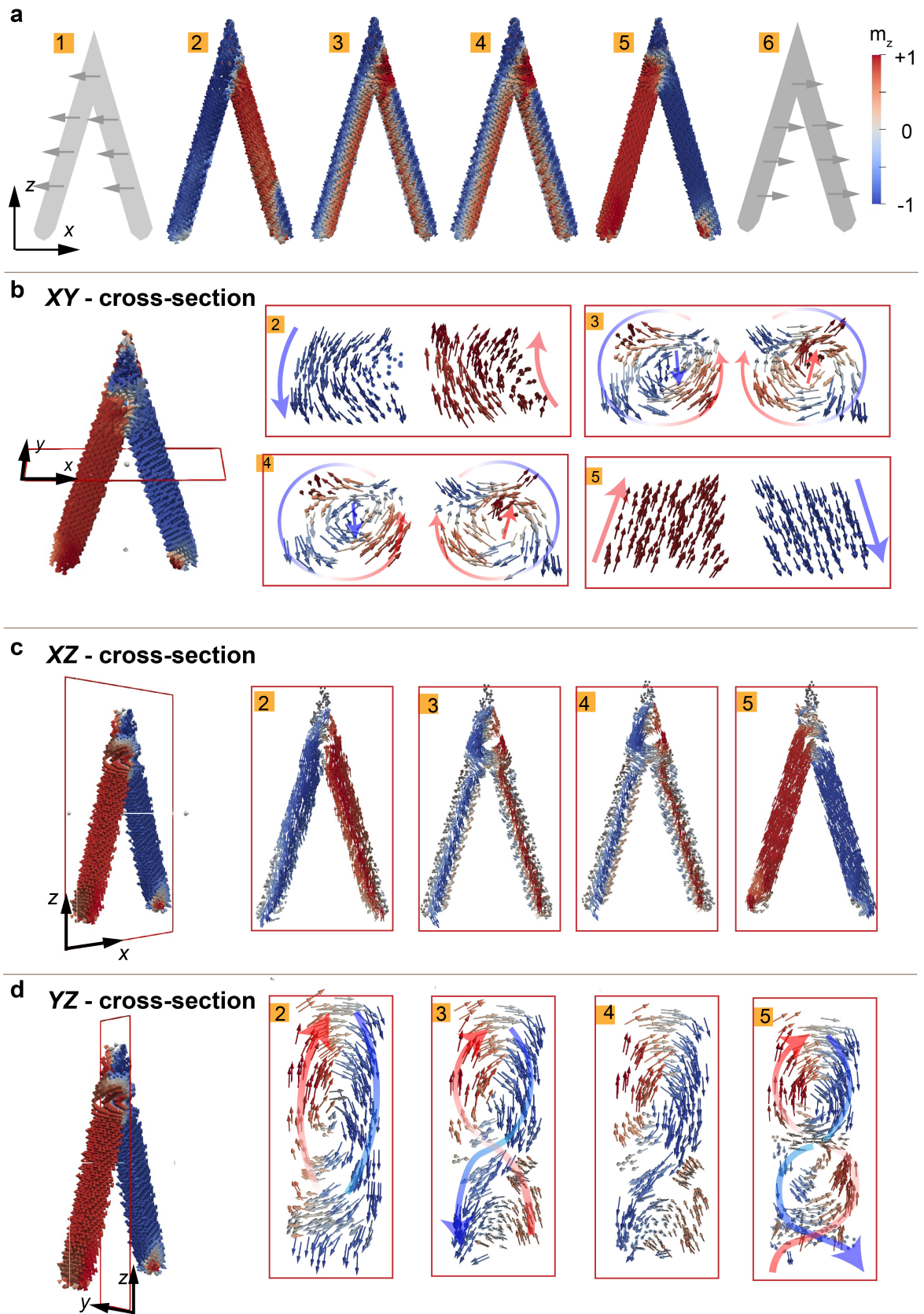


Fig. 4.8 The simulated magnetic configurations of the sates of interest. The arrows represent the direction of magnetisation and the colour represents the  $m_z$ . (a) The front view of the magnetisation states. (b) XY-cross-sectional view of the magnetic configurations. (c) XZ-cross-sectional view of the magnetic configurations. (d) YZ-cross-sectional view of the magnetic configurations.

which is to be expected from the MT signal, because local texture changes, such as the presence of domain walls, should not result in such a large drop. The  $XY$  cross-sectional view in **Figure 4.8 b** reveals that two vortex tubes [121] with the same chirality are formed in state 3. The cores of these two vortex tubes can be seen more clearly in the  $XZ$  cross sectional view (**Figure 4.8 c**), which have opposite  $m_z$  for both legs. Since the magnetisation is circulating around the current axis, it will induce a large drop in the AMR and lead to the cancelling out of AHE again. As shown in **Figure 4.7 c**, indeed AMR is the major contribution to this drop. We also notice that the MMR effect becomes slightly more negative in state 3. The MMR is a measure of spin disorder, and it depends on the orientation of the magnetisation relative to the applied field [73]. In this vortex tube state, the majority of the magnetisation is more parallel to the field applied in the  $x$ -direction, introducing less spin disorder and hence a slightly decreased resistivity.

**State 3 to state 4.** There is an additional drop of resistance in state 4 due to a decrease of AMR. This is the state just before switching back to the high resistance state, where a spin distribution is most perpendicular to the current direction.

**State 4 to state 5.** As the applied field keeps increasing in the positive  $x$ -direction, the bridge instantly exits the vortex tube state. In comparison with state 2, the magnetisation of the two legs has reversed. For the MT simulation, where the relative orientation of magnetisation with respect to the current is most important, state 2 and 5 are nearly equivalent. Thus, in state 5, the resistance has returned to a level comparable to state 2.

**State 5 to state 6.** This is the reverse process of state 1 to 2, given that the magnetisation reversal in that field range is fully reversible.

It is also worth noting how the magnetisation from two legs are connected at the apex region of the bridge from the micromagnetic simulation (shown by the  $YZ$  cross-sectional view in **Figure 4.8 d**), despite the fact that this cannot be confirmed by MT measurements solely. In state 2, the magnetisation of the entire bridge forms a large vortex present at the top. As the bridge attempts to switch via the vortex tube states (states 3 and 4), we see how a vortex-antivortex pair forms, coinciding with vortex tubes in the legs. In state 5, to adapt to the reversed uniform magnetic states for the legs compared to the previous state 2, there is an additional vortex formed. Micromagnetic simulation suggests the formation of complex magnetic configurations in the top part to match the varying magnetic states from the legs, which can be either uniform or vortex tubes. In particular, the vortex-antivortex pair

has a natural tendency to annihilate [122] but exists to connect the two stable vortex tubes. These swirling configurations, from the perspective of AMR and AHE effects, are almost equivalent, hence microscopy methods are required to have a clear identification of them.

The good agreement between the experimental and simulated MT results provides a good understanding of the reversal processes of the bridge under  $x$ -direction field application. In particular, the combination of micromagnetic and FEM modelling enables the identification a non-trivial vortex tube state in the nanobridge. As shown in **Figure 4.9**, this type of extended vortex structure with a core parallel to the nanowire axis (also known as *global vortex state* [112] or *vortex domain* [121]) has been predicted and observed in nanowires with diameters exceed a critical value [50, 114, 123], where the energy reduction due to the decrease in magnetostatic energy by forming a flux closure configuration exceeding the increase in exchange energy. The vortex tube structures existing in nanowires have been proposed before for the concept of 3D vortex-based magnetic memories, which offers some interesting properties such as their stability against thermal fluctuation due to the large energy barrier that separates two vortex tubes with opposite polarities and the minimised stray field that avoids magnetostatic interaction between memory elements [112, 124]. From an MT perspective, it is also interesting to note how the vortex tube state results in a state with resistivity approximately equal to  $\rho_{\perp}$  (when  $\vec{m}$  is perpendicular to  $\vec{J}$ ) in a nanowire without saturating it in the transverse direction, which usually requires a large field if the aspect ratio is high [112].

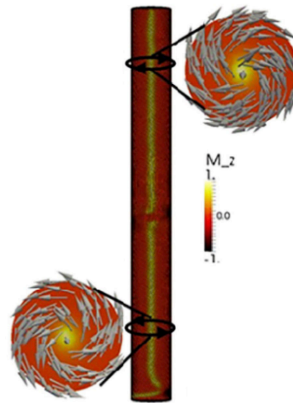


Fig. 4.9 *The global vortex state found in a Co nanowire. The image is reproduced from [121] under CC4 Attribution licenses.*

One discrepancy between the experiment and the simulation is the value of the field when the vortex tube forms, which is around 2 mT in the data but at 80 mT in the simulation. The

discrepancy in the switching field is expected, given that the simulation is performed at 0 K instead of 150 K: indeed, thermal excitation will makes switching easier and therefore will occur at lower fields [55]. The second difference is the way the system exits the vortex tube state. Indeed, the micromagnetic simulation predicts an abrupt reversal from vortex tube to mono-domain state only by assuming an ideal wire without surface roughness, grain boundaries, and defects. In experiments, we observe the resistance changing gradually in a wider field region indicating the magnetisation does not reverse at once and the reversal proceeds only upon further increase in the magnetic field. This is indicative of the pinning of DWs, which continue to propagate upon further increase in the magnetic field [125]. Multiple walls might be involved in this process, therefore giving rise to the relatively wide range of fields where the resistance changes [112].



## 4.2 Magnetisation reversal process in $z$ -direction

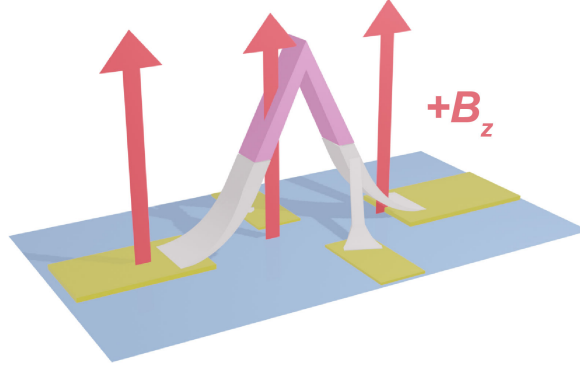


Fig. 4.10 Schematic of the applied field configuration with respect to the 3D nanobridge. Field is applied in the positive  $z$ -direction.

In this section, we investigate the reversal process of the bridge under field applied in  $z$ -direction *i.e.*, the direction perpendicular to the substrate, as shown in **Figure 4.10**. Except for the field direction, the rest of the measurement setup is identical to that described in the  $B_x$  case. Sixteen full MT hysteresis loops were measured again, and the average is shown in **Figure 4.11**. This general asymmetric pattern was already understood in the high-field study as the odd effects (AHE and OHE) from different parts of the bridge no longer cancel out each other as they do in the  $B_x$  case [61]. The measurements are fully reversible for  $|\mu_0 H_z| > \approx 0.15$  T. However, the understanding of the switching process in this case happening at lower fields is not trivial; as shown in **Figure 4.11 b**, the MT signals in the low field region are far more complicated than those in the  $B_x$  case with multiple transitions observed.

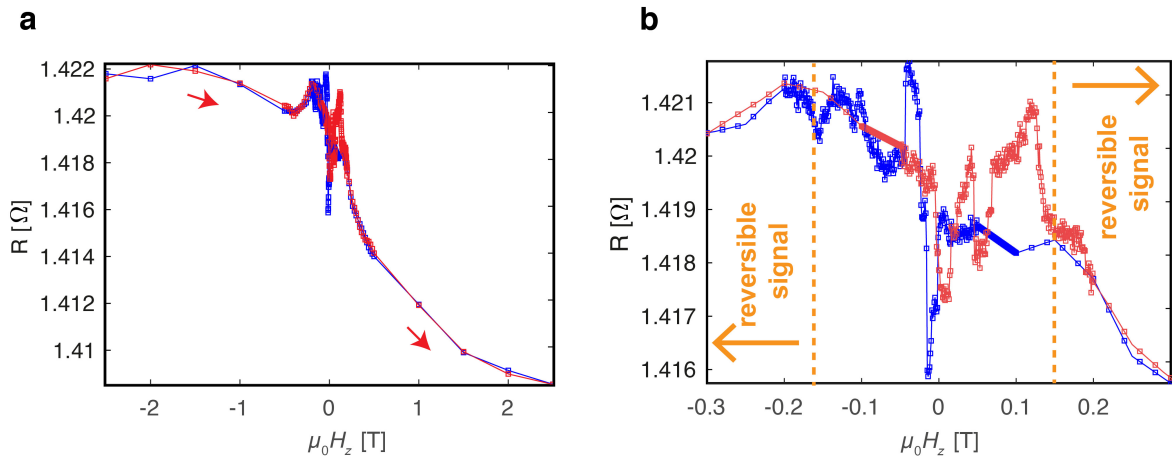


Fig. 4.11 The average of 16 MT hysteresis loops for field applied in  $z$ -direction. **(a)** The full hysteresis loop between -2.5 T to 2.5 T. **(b)** Zoom-in region between -0.3 T to and 0.3 T.

In the  $B_x$  case, the loops were highly reproducible, with the same trend observed for all events measured and only small variability in the fields where these events take place. This is not the case for the  $B_z$  case, where different curves recorded are fundamentally different, showing different reversal modes with more metastable states. We can intuitively explain this due to the different projections of  $B_x$  and  $B_z$  over the bridge legs, and different types of reversal mechanism expected from these projections; in particular with  $B_z$  likely to produce a DW propagation dominated reversal. A  $B_z$  field has a larger projection along the legs of the bridge, so that triggers DW motion and the pinning of DW leads to a more stochastic process, whereas a  $B_x$  field has a larger component transverse to the leg axes, resulting in an overall more rotation of the magnetisation, with the second being a more deterministic process [112, 113]. For the  $B_z$  case, we have essentially identified two switching modes for

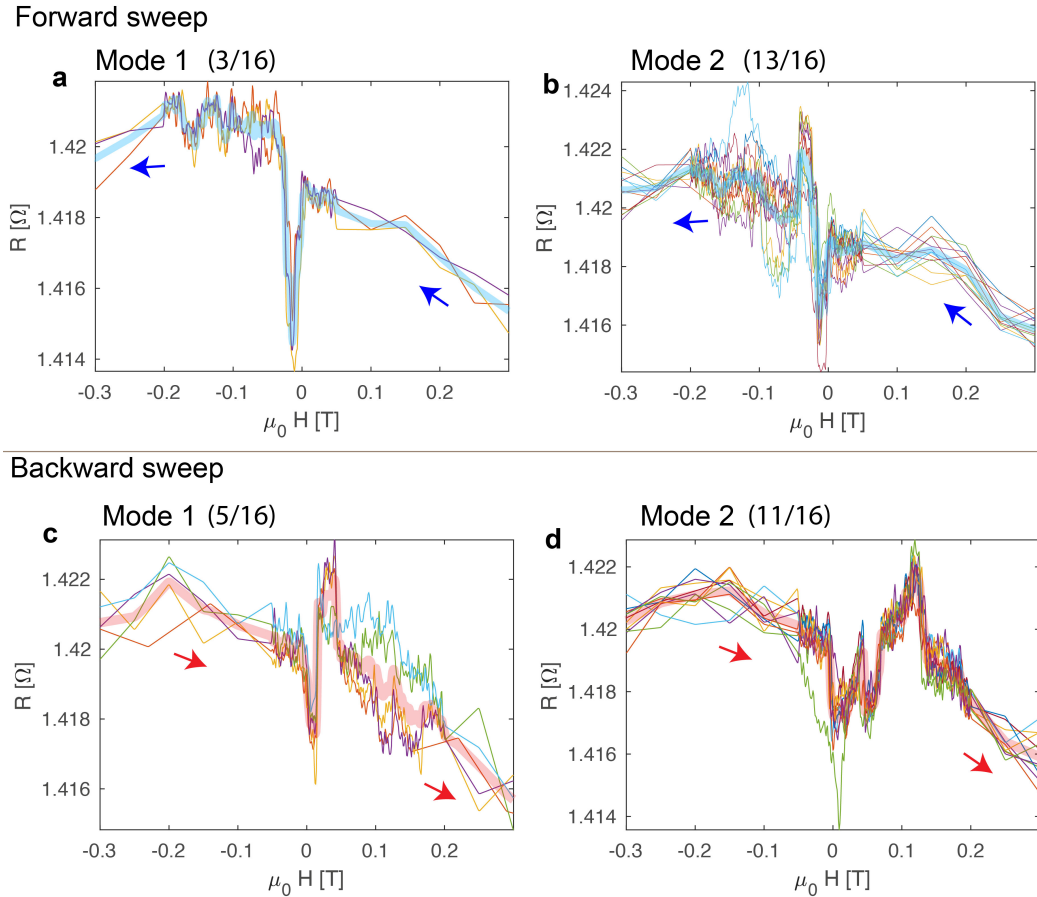


Fig. 4.12 An overview of all 16  $B_z$  hysteresis loops in the range between  $\pm 0.3$  T. Two switching modes are identified for both (a)-(b) Forward sweeps and (c)-(d) Backward sweeps. The thicker line represents the average of each mode. The number of times each type of mode is observed with respect to the total 16 loops is included in brackets.

both forward (**Figure 4.12 a and b**) and backward sweeps (**Figure 4.12 c and d**). For each mode, the average is plotted as the thick line.

### 4.2.1 Analysis of the experiment MT loops

To better present the details of each switching mode, we plot the average of each mode separately for the forward and backward sweeps, as shown in **Figure 4.13** and **Figure 4.14**, respectively. From the  $B_x$  study, where the magnetisation reversal process is less complicated, we have discussed the classification of relevant magnetisation states in terms of changes in the resistance. This information, together with the understanding of the saturated states in  $\pm z$ -direction from the high-field study, allows us to analyse these more complicated reversal processes for the  $B_z$  case and propose states involved based on the average plots. The micro-magnetic simulation for this case is still work in progress and will be addressed in future work.

#### Forward sweeps: mode 1

We start from mode 1 of the forward sweeps as shown in **Figure 4.13 a** ( between  $\pm 2.5$  T) and **b** (between  $\pm 0.3$  T).

**State 1 and state 5.** As labelled in **Figure 4.13 a**, state 1 and 5 are the saturated states in the  $+z$  and  $-z$  directions (Their schematics are shown in **Figure 4.13 e (1), (5)**). As discussed in detail in chapter 3, the study of these two states in the high-field study explains that the asymmetric hysteresis loop is caused by the fact that odd effects such as AHE and OHE from the two legs no longer cancel out each other [61].

**State 2 and state 4.** As the magnitude of the applied field decreases, the magnetisation coherently aligns with the bridge geometry as shown in the schematics in (**Figure 4.13 e (2), (4)**). On the MT signal (**Figure 4.13 b**), we define these two states roughly at the end of the reversible signal range (marked by the yellow vertical line). The higher resistance at state 4 compared to state 2 may originate from the opposing AHE effects from the top part of the bridge [61], and these two states are equivalent in terms of AMR.

**State 3.** Between state 2 and state 4, we observe a resistance drop with a magnitude of  $\approx 5$  m $\Omega$ , which is at a comparable size with the average resistance drop measured in the  $B_x$  case ( $\approx 6$  m $\Omega$ ) when a vortex tube state formed. Hence, we can deduce that in mode 1, the

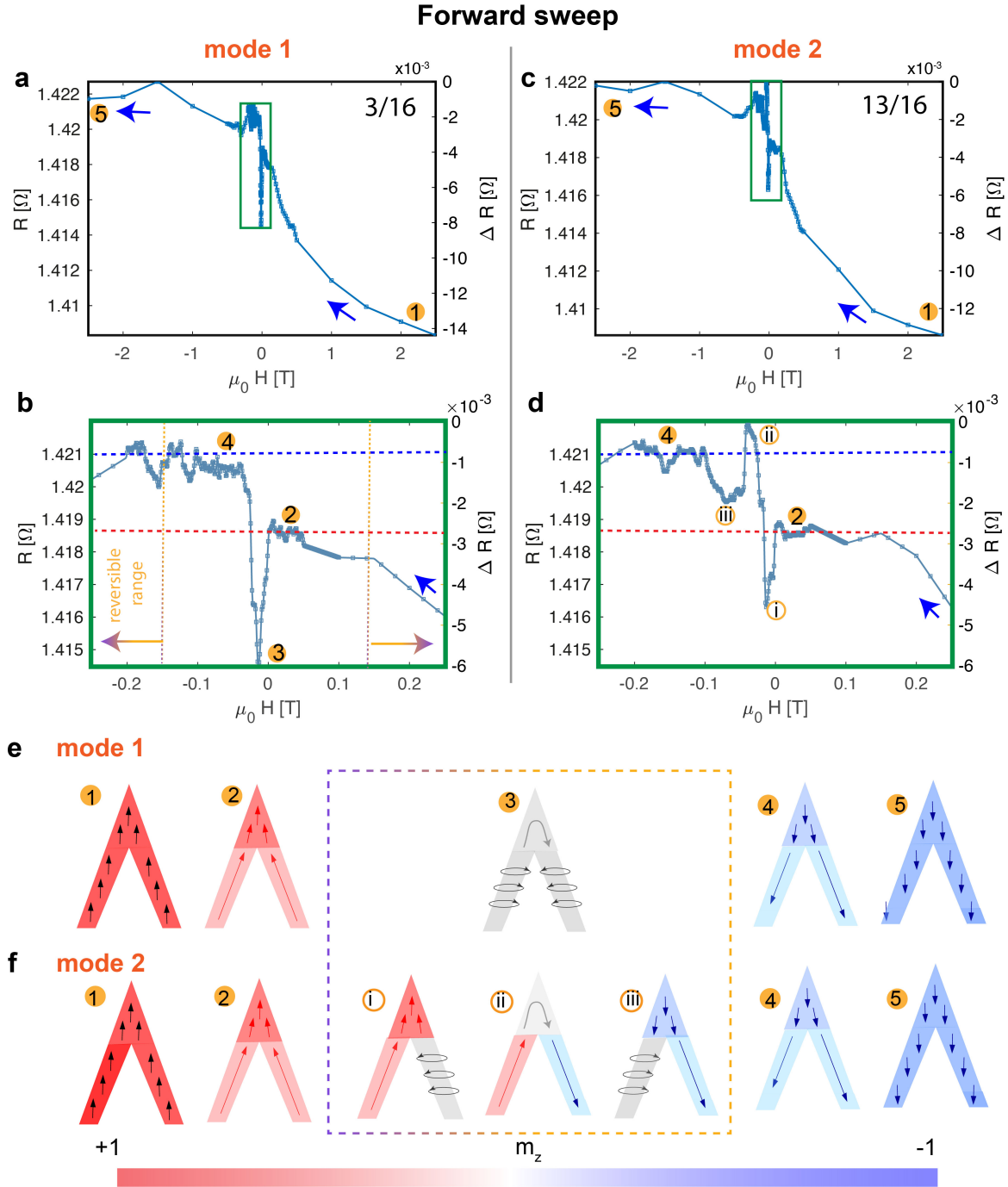


Fig. 4.13 Comparison between the two switching modes for the forward sweeps. (a)-(b) Mode 1 in  $\pm 2.5$  T and  $\pm 0.3$  T range, respectively. (c)-(d) Mode 2 in  $\pm 2.5$  T and  $\pm 0.3$  T range, respectively. (e) Proposed states for mode 1. (f) Proposed states for mode 2.

bridge also switches via a vortex tube state as illustrated in state 3 in **Figure 4.13 e (3)**.

### Forward sweeps: mode 2

For mode 2 of the forward sweeps, the same states 1,2,4 and 5 are defined on the MT signal (**Figure 4.13 c and d**), and the same resistance measured at these states between modes 1 and 2 supports our identification of these states. Now, the difference between modes 1 and 2 can be understood simply by noticing how the reversal process occurs between states 2 and 4. Three new states are defined between state 2 and 4 as shown in **Figure 4.13 d**.

**State 2 to state i.** There is a drop of  $\approx 2.5 \text{ m}\Omega$ , which is roughly half of the large drop we saw in mode 1. Hence, a reasonable hypothesis is that this change corresponds to only one leg falling into the vortex tube state as illustrated in **Figure 4.13 f (i)**.

**State i to state ii.** After this leg switches, **state ii** is reached. As shown in **Figure 4.13 f (ii)**, an increase in resistance is expected due to the increase in the AMR with the disappearance of the vortex tube, and also the elimination of the negative AHE from the top region of the bridge. The MT data also confirms this increase in resistance.

**State ii to state iii.** Then, another drop of resistance of  $\approx 2.5 \text{ m}\Omega$  is observed in the data, which could be attributed to the second leg switching via the vortex state as shown in **Figure 4.13 f (iii)**.

**State iii to state 4.** Finally, the second leg switches, the resistance climbed back to state 4 level again due to the increase of AMR. The successive switching of the two legs proposed for mode 2 can be explained by the fact that the  $B_z$  field is not aligned perfectly in symmetry with respect to the two legs [83].

### Backward sweeps: modes 1 and 2

**Figure 4.14** shows the average of two switching modes for backward sweeps. Mode 1 of the backward sweeps resembles the same pattern (drop-rise-drop) as mode 2 of the forward sweeps. Hence, it may also correspond to the sequential switching of two legs via vortex tube states. Mode 2 of the backward sweeps generally follows the same pattern as mode 1, but with more intermediate steps. The step sizes of resistance change are still around  $2.5 \text{ m}\Omega$

implying that switching is still governed by curling of magnetisation [83] and may relate to more complicated process such as multiple vortex tube domains formed sequentially in one leg [124] .

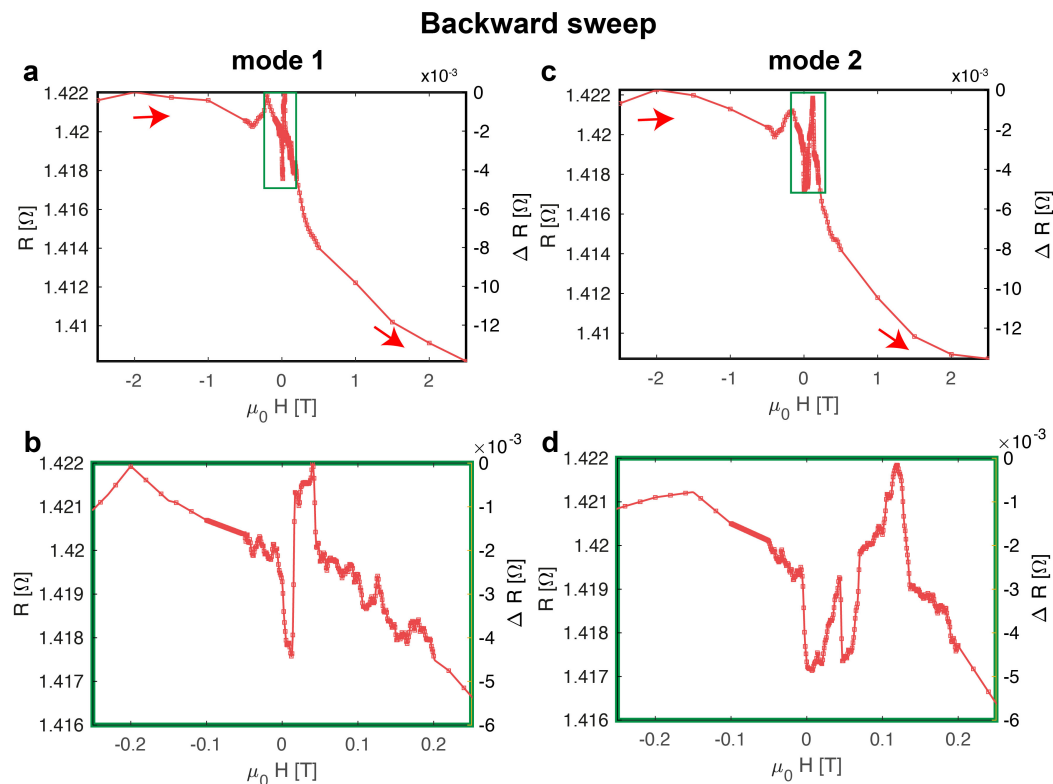


Fig. 4.14 The comparison between the two switching modes in the backward sweeps. (a)-(b) Mode 1 in  $\pm 2.5$  T and  $\pm 0.3$  T range, respectively. (c)-(d) Mode 2 in  $\pm 2.5$  T and  $\pm 0.3$  T range, respectively.

### 4.3 Chapter Summary

The interpretation of the magnetic reversal process using magnetotransport measurements in 3D nanostructures [112, 83] with relatively complex geometry with respect to the electrical contacts, such as the nanobridge investigated, is a very challenging task considering the multiple MT effects superposed and the intrinsically more complicated spin configurations due to the complex energy landscapes in 3D structures [121]. In this chapter, together with the high-field study presented previously, we demonstrate how we build an understanding of the nanobridge's reversal processes and their corresponding MT signals step by step, from known saturated magnetic states (high-field study presented in chapter 3) to relatively simple and reproducible processes ( $B_x$  case), and finally the assignment of possible states in a more complicated process ( $B_z$  case) according to the measured resistance values.

Specifically, in the  $B_x$  case, we observe one deterministic switching event associated with a large resistance drop. The good agreement between the data and the simulation which is based on a combination of micromagnetic and FEM modelling allows us to identify a non-trivial vortex-tube state which exists to minimise the magnetostatic energy [121, 50, 114]. In the  $B_z$  case, the switching processes become more complicated and stochastic, indicating more DW propagation mediated processes [112]. By comparing the magnitude of resistance change with the  $B_x$  case, some possible magnetic states based on the vortex tube configuration have been proposed. The micromagnetic simulation for the  $B_z$  case is still work in progress and will be addressed in future work.

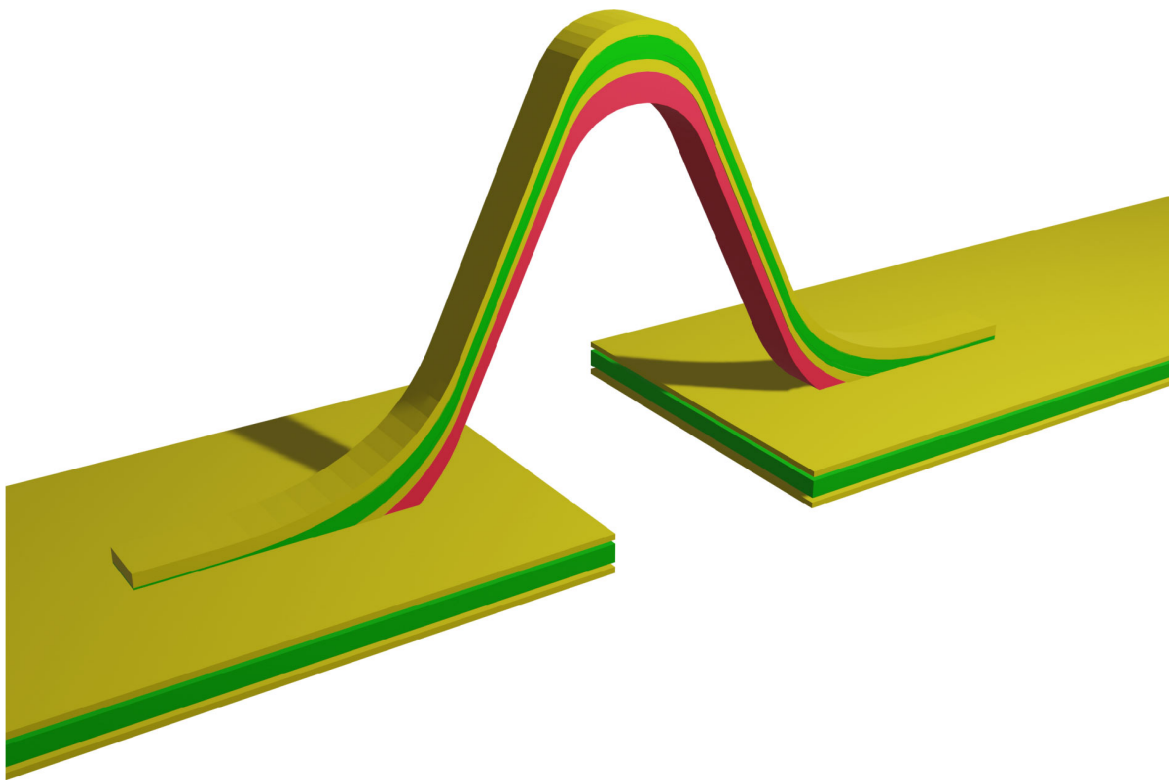
In addition to deducing possible magnetic configurations involved in the reversal process, the magnetotransport study also demonstrates the great potential of using 3D nanomagnets in applications. For example, the vortex tube state available in the 3D nanobridge results in an equivalent resistivity of  $\approx \rho_{\perp}$  without requiring a large field to saturate the structure in the transverse direction. Combined with the low stray field exhibited by the vortex tube states, they could be potentially interesting for 3D vortex based memory [124]. The different shapes and reproducibility of MT loops obtained from the  $B_x$  and  $B_z$  cases also demonstrate how 3D structures are inherently susceptible to field with different directions due to the complicated energy landscapes in 3D structures [50]. Depending on the magnitude and direction of the magnetic field, the 3D bridge shows the potential to be programmed in different states [112] and to have control over the stochasticity of the switching process. These make the 3D nanobridge potentially interesting for serving as a building block for neuromorphic computing[118].





## **Chapter 5**

### **3D Nanomagnetic Systems with Multilayered Materials**



## Published Material Included in This Chapter

A substantial part of the work presented in this chapter has been previously published in the following article:

*Meng, F.; Donnelly, C.; Skoric, L.; Hierro-Rodriguez, A.; Liao, J.-w.; Fernández-Pacheco, A. Fabrication of a 3D Nanomagnetic Circuit with Multi-Layered Materials for Applications in Spintronics. Micromachines 2021, 12, 859. <https://doi.org/10.3390/mi12080859>.*

This is published under a Creative Commons Attribution (CC-BY) License. Being the result of my own original work, considerable parts of this article are reproduced in this thesis as allowed by this license.

## Contributions

### ■ section 5.1. 3D nanoramps with multilayered materials

- The dark-field MOKE setup and the characterisation methodology was developed by our former group member Dr Dedalo Sanz-Hernandez.

### ■ section 5.2. Create a 3D nanomagnetic circuit with multi-layered materials

- The algorithm used to generate codes for computerised beam control for 3D nanoprinting was developed by our group member Luka Skoric.
- I would like to thank Dr Jungwei Liao for his training in the use of all the lithographic techniques mentioned.
- I would also like to thank Dr Claire Donnelly, Dr Amalio Fernandez Pacheco, and Dr Aurelio Hierro-Rodriguez for their advice on the development of the simulation methodology for understanding magnetoelectrical signals from 3D geometries.

All the results presented in this chapter are the result of my own work.

## Introduction

In previous chapters, we discussed magnetotransport studies on a nanomagnetic circuit created via direct-writing of a cobalt 3D nanostructure on pre-patterned contacts. The FEBID technique employed represents the most advanced 3D nano-printing technique currently available [91], providing significant more flexibility in the choice of geometries. Hence, this fabrication route is well suited for prototyping devices with complex geometries and exploring 3D geometrical effects on magneto-electrical signals. However, FEBID, essentially a chemical vapour deposition, is limited by the range of magnetic materials it can deliver (only cobalt, iron or cobalt-iron alloys [40]) and can not be used directly to create materials or interfaces with the quality typically required by spintronic applications [126].

To introduce high-quality magnetic materials into 3D systems, researchers have developed a reliable strategy consisting of using physical vapour deposition on top of a non-magnetic scaffold. These scaffolds can be created in various ways, including FEBID [43], two-photon lithography [41, 19] and also self-assembly[42]. In this way, a 3D nanomagnetic domain wall conduit and a frustrated 3D nanowire lattice have been realised respectively by evaporating 50 nm-thick permalloy on top of a nano-ramp (created by FEBID [43]) and a freestanding diamond lattice structure (created by two-photon lithography [19]).

In this chapter, we adapt this 'scaffold + physical vapour deposition' method to the use of multilayered materials in 3D systems by using DC magnetron sputtering on top of FEBID made non-magnetic scaffolds. We first employed a dark-field MOKE [43] setup to probe a 3D nano-ramp created with Ta/CoFeB/Ta layers and tested the viability of using sputtered materials to achieve functional 3D systems. Then, we consider how to connect such a 3D nanomagnet made with multilayered materials into electrical circuits, which is not straightforward as the full-coverage characteristics of PVD methods invariably lead to the short-circuit of the 3D structure. A multi-technique fabrication method has been developed to overcome this issue and was demonstrated with the establishment of a 3D nanobridge circuit. The magnetic states of this circuit were investigated by magnetotransport measurements aided by a combination of micromagnetic and finite element modelling.

## 5.1 3D nano-ramp with multilayered materials

Previously, in our group, Sanz-Hernandez *et al.* has demonstrated field-mediated controllable domain wall injection from 2D thin film into a 3D nanomagnetic conduit which was fabricated by evaporating 50 nm thick permalloy on top a 3D nano-ramp created via FEBID. He established a dark-field MOKE setup which enables independent and simultaneous detection of the magnetic switching of both the 3D nanoramp and the 2D film around it [43]. By exploiting the geometrical bias of the magnetic field exerted on 2D and 3D components, he obtained one of the first observations for transmitting magnetic information to a different plane, which is an essential advancement in the field of 3D spintronics [12]. Here, to incorporate multilayered materials which plays a vital role in the development of spintronics into a 3D system, we replaced thermal evaporation with DC magnetron sputtering. Since sputtering and thermal evaporation usually result in thin films with very different properties such as uniformity, film stress, and density, we adopted this established characterisation methodology as a first step to understand 3D nanomagnetic systems with multi-layered materials.

### 5.1.1 Sample fabrication

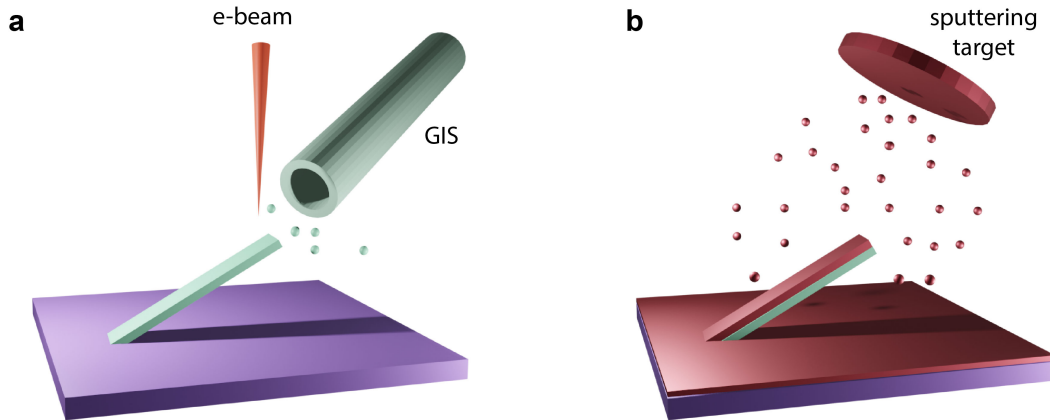


Fig. 5.1 *Sample fabrication. (a) A non-magnetic scaffold is 3D printed using FEBID, with its composition being a carbon-rich amorphous mixture of carbon and platinum [80]. (b) Magnetic multilayered thin films is sputtered onto the scaffold. For simplicity, only one layer is shown.*

The 3D nanomagnetic ramp was created via a two-step process. In step 1, a non-magnetic scaffold was built via FEBID (**Figure 5.1 a**) using a non-magnetic precursor  $(\text{CH}_3)_3\text{Pt}(\text{C}_6\text{H}_5)_3$  with an accelerating voltage and beam current of 30 kV and 21 pA, respectively. Under these growth conditions, the non-magnetic ramp has a composition a

carbon-rich amorphous mixture of carbon and platinum [80]. The nanoramp was designed to make a  $30^\circ$  angle with respect to the substrate to be compatible with the dark-field MOKE setup in our laboratory. In step 2, Ta/CoFeB/Ta (2/10/2 nm) was deposited over the whole sample using DC magnetron sputtering (**Figure 5.1 b**). CoFeB, a workhorse of spintronic devices [127], was chosen due to its soft material properties, high spin polarisation and moderate magnetisation which are ideal for nanowire-based domain wall conduit devices, for memory or logic applications [128]. The integration of CoFeB onto a 3D systems thus represents the first realisation of a 3D spintronic device with these material properties.

### 5.1.2 Dark-field MOKE setup and the corresponding characterisation methodology

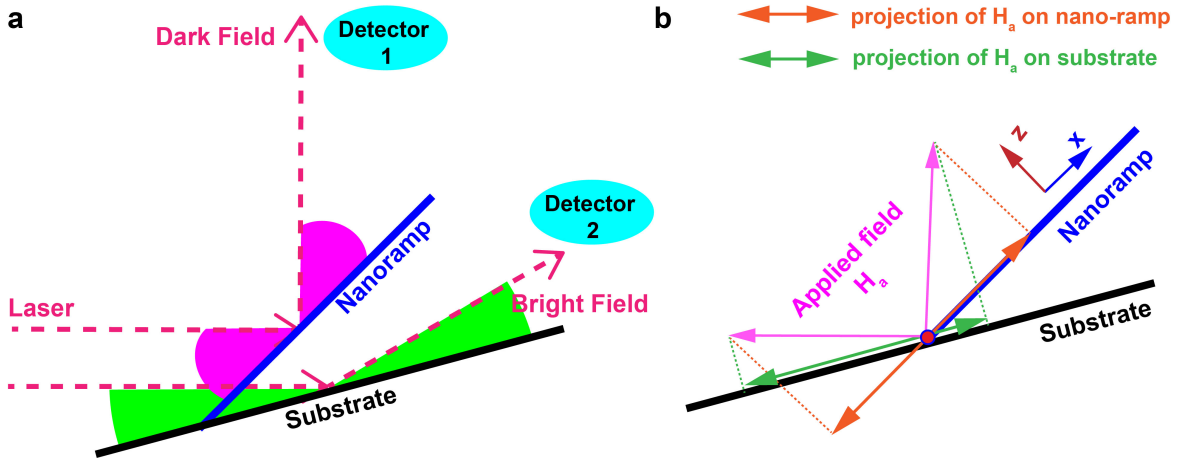


Fig. 5.2 (a) Dark-field MOKE setup (b) Magnetic field configuration. The applied field ( $0$  and  $\pi$  phase is shown in pink) consists of a low-frequency oscillating field along the  $x$ -axis, combined with a constant  $z$ -offset normal to it. The projections of the applied field on the nanoramp and substrate are shown in orange and green, respectively.

3D geometries pose many challenges on the characterisation of 3D nanomagnets, especially with the use standard magnetometry or magnetic microscopy methods [111, 43]. In the group, a dark-field MOKE was developed, exploiting the different angles formed by the 3D nanostructure and the thin film with respect to the laser direction (**Figure 5.2 a**). Hence, compared to a standard MOKE setup, two detectors were positioned at two different angles, which capture specular reflections from both the film and ramp part. This setup allows the detection of the measurements of the nanoramp and the film around it simultaneously and independently [43].

With the dark-field MOKE setup, the switching mechanisms of a 3D nanoramp made with multilayered materials under external field could be investigated. As shown in **Figure 5.2 b**, applied field ( $\vec{H}_a$ ) consists of a low-frequency oscillating field along the nanowire axis ( $x$ -axis), combined with a constant  $z$ -offset normal to it. Such applied field (labelled by pink) always has a symmetric positive and negative projections along the nano-ramp direction (labelled by orange). However, the projection is not symmetric for the substrate plane (labelled by green). It is challenging to interpret isolated hysteresis loops, as any applied field has a different projection along different parts of the sample, thus a set of measurements with different  $z$ -offsets were obtained.

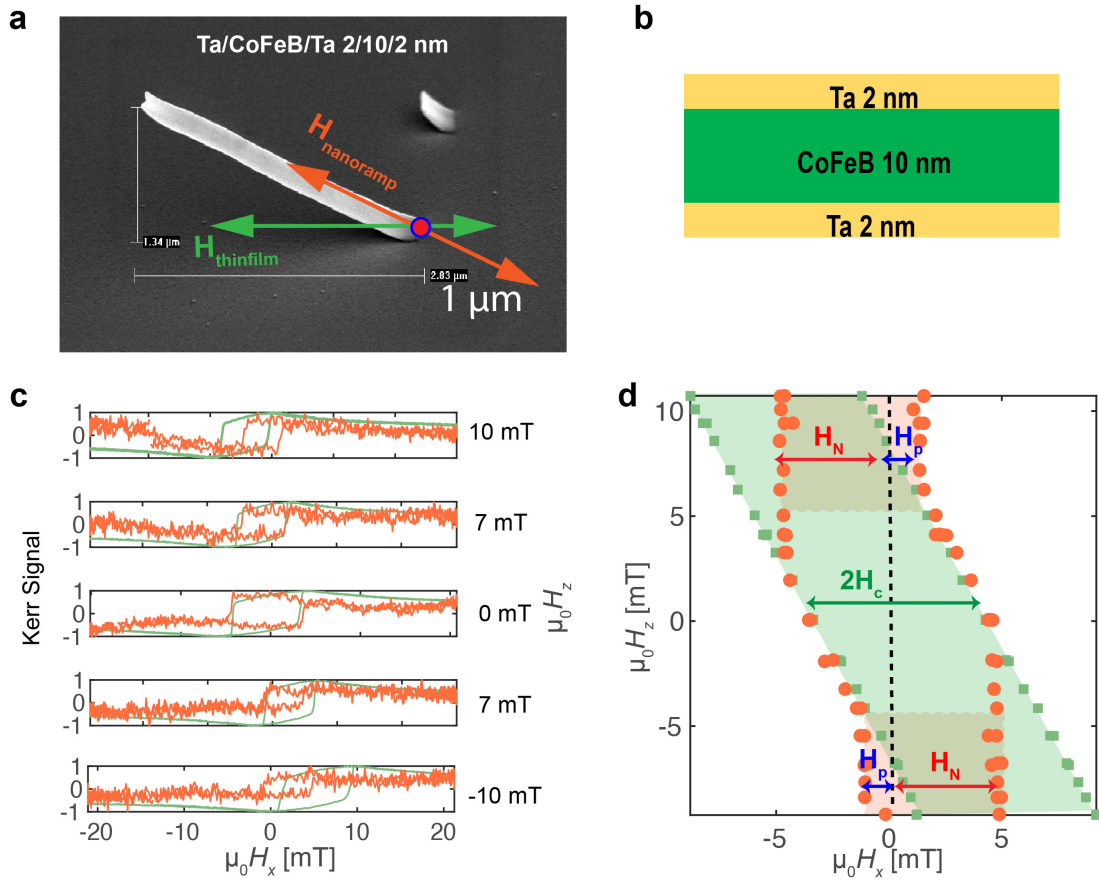


Fig. 5.3 (a) SEM image of a nanomagnetic ramp after sputtering Ta/CoFeB/Ta (2/10/2 nm). The projection of applied field on the 3D nanoramp and the 2D thin film are labelled in orange and green respectively. (b) The schematic of magnetic materials used. (c) Subset of hysteresis loops for the 3D ramp (orange) and the 2D film (green) at different  $H_z$  offsets. (d) ( $H_x$ ,  $H_z$ ) diagram of switching fields for the nanoramp (orange) and the 2D film (green).

The resultant magnetic nanoramp with Ta/CoFeB/Ta (2/10/2 nm) materials on top is shown in **Figure 5.3 a** and the system was characterised using the aforementioned method. In **Figure 5.3 c**, a subset of hysteresis loops obtained from both the film and the ramp at varying offset  $H_z$  are plotted in green and orange, respectively. To compare the switching events from the ramp and the film, we plot points at switching fields as shown in **Figure 5.3 d**. First, we see the film (green dots in **Figure 5.3 d**) switched asymmetrically as a function of  $H_x$  for any  $H_z$ . This is expected as explained in the field setup, the projection of the total applied field on the substrate is not symmetric, hence the film is geometrically biased and we measured a  $H_c \approx 4$  mT.

Then we consider the switching behaviour of the nanoramp which has a richer switching landscape, as seen by the orange dots in **Figure 5.3 d**. We can infer that its switching behaviour is influenced by the film as the symmetric projection of the field on the nanoramp plane will result in hysteresis loops that are symmetric about  $H_x = 0$  mT if the ramp switches independently. For cases where offset  $|\mu_0 H_z| > 5$  mT (shaded by orange boxes), the film experiences a large geometrical bias, which may prevent the film from switching while the ramp does. In this regime, we identify two switching mechanisms for the ramp. For example, for  $\mu_0 H_z > 5$  mT, the film is positively biased. As  $\mu_0 H_x$  increases from negative to positive, the film switches first and there will be a DW formed in the ramp and when the projection of  $\vec{H}_a$  along the nanowire is high enough, the ramp can be switched via DW propagation. As  $\mu_0 H_x$  decreases from positive to negative, the large geometrical bias prevents the film from switching and hence the ramp can only switch via DW nucleation. The threshold propagation and nucleation fields are  $\mu_0 H_P = 2$  mT and  $\mu_0 H_N = 5$  mT, respectively and we also observe switching via nucleation to be sharper than that via propagation. For  $|\mu_0 H_z| < 5$  mT, the geometrical bias becomes smaller and we see the switching of the ramp follows the film line. This is a direct consequence of the film acting as a source of domains and the projection of  $\vec{H}_a$  along both the ramp and the film-ramp connection is enough to propagate the domain walls, and the whole system switches fully.

In this study, we used a dark field MOKE characterisation methodology to first demonstrate that multilayered materials could be incorporated into 3D systems successfully through sputtering. As a consequence, we obtain a functional 3D device with the quality that can transport magnetic information in three dimensions under external magnetic fields.

## 5.2 3D nanomagnetic circuit with multilayered materials

After testing the viability of using sputtered multilayered materials in 3D systems, we now consider how to create a 3D nanomagnetic circuit with multilayered materials, in which electrical current should be injected to exploit magnetoelectrical and spin transport effects. Until now, the realisation of a 3D spintronic device based on PVD materials with a 3D geometry has not yet been realised. As shown in **Figure 5.4 a, b**, one of the major obstacles preventing this strategy from being used in 3D spintronic devices is that with standard PVD techniques, the material is deposited everywhere on a substrate, meaning that without additional non-trivial fabrication steps, the current is shunted away from the 3D structure and instead runs through the continuous thin film deposited around it.

In this study, we have developed a fabrication process to overcome the 'current shunt' constraint of the 'scaffold + PVD' method. To demonstrate this new process, we have developed a 3D circuit based on a nanobridge geometry (**Figure 5.4 c**) and Ta/CoFeB/Ta materials. The bridge geometry was chosen again as it is the basic element that can readily interconnect different parts of a 3D nanomagnetic circuit and Ta/CoFeB/Ta multilayer was used as it has been tested it on the 3D nanoramp. The non-magnetic scaffold of the bridge was created by FEBID again, exploiting the capability for mask-less fabrication of 3D structures with tens of nanometre spatial resolution [77].

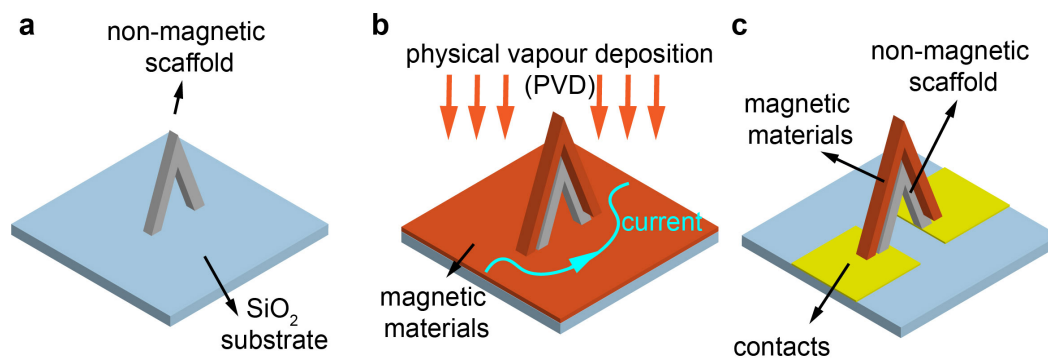


Fig. 5.4 Creating a 3D nanomagnetic circuit using the combination of a scaffold and PVD. (a) Create a non-magnetic scaffold. (b) Incorporate magnetic materials using PVD, magnetic thin films deposited will shunt current from the 3D structure. (c) The ideal 3D nanomagnetic circuit created using 'scaffold + PVD' method. Reproduced from [129].



### 5.2.1 Fabrication process

To overcome the shunting effect, in addition to sputtering thin films on top of a non-magnetic scaffold created by FEBID, we make use of patterned resist to limit the area of the deposited thin films, as well as a milled trench under the 3D structure to ensure the current only flows through the top of the 3D bridge. A summary of the fabrication process is given in **Figure 5.5** and each step will be explained in details hereafter.

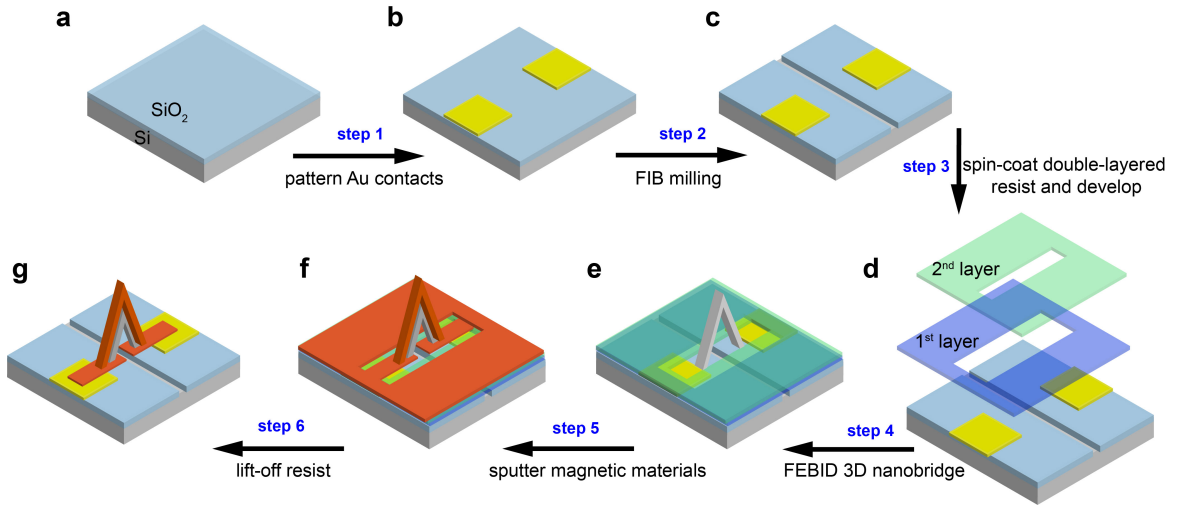


Fig. 5.5 *Fabrication process. (a) Preparation of a clean silicon substrate with 300 nm thermally oxidised silicon dioxide. (b) Patterning of Au contacts using optical-lithography and sputtering. (c) Milling of a trench between two contacts using focused ion beam. (d) Spin-coating and patterning of the double-layered resist. (e) FEBID 3D Pt-C scaffold (f) Sputter multilayered materials. (g) Lift-off resist. Reproduced from [129].*

#### Step 1 : Au contact pads

At the beginning of the process, Au contact pads were patterned on a clean silicon dioxide substrate using optical-lithography and sputtering (**Figure 5.5 a, b**). The material used for contacts was Ta/Au (2/30 nm).

#### Step 2: Focused ion beam milling

Next, a trench was milled by focused ion beam (FIB) between the two contact pads (**Figure 5.5 c**), preventing the formation of a continuous film under the bridge. FIB milling is a critical step in this fabrication process and must be completed before the use of resist. This is due to the fact that if the resist is exposed to the ion beam, it will harden and therefore cannot be removed in the subsequent lift off process, leading to metallic lift off edges spanning the

trench, which provide paths for the current to shunt as shown in **Figure 5.6**. Milling the trench beforehand also avoids inadvertent gallium ion implantation, which can lead to the deterioration of the magnetic material [130].

The width and depth of the trench should be sufficient to prevent the formation of a continuous film within the trench. In our case, for a total 30 nm thick materials to be sputtered, we have milled a trench of width =  $0.85\ \mu\text{m}$  and nominal depth = 500 nm, which is sufficient for this purpose, as proved by the electrical insulation test presented later. In this study, a  $\text{Ga}^+$  ion beam was used and milling parameters were set as the following: accelerating voltage = 30 kV, beam current = 0.28 nA, beam diameter overlap = 50% and dwell time =  $1\ \mu\text{s}$ .

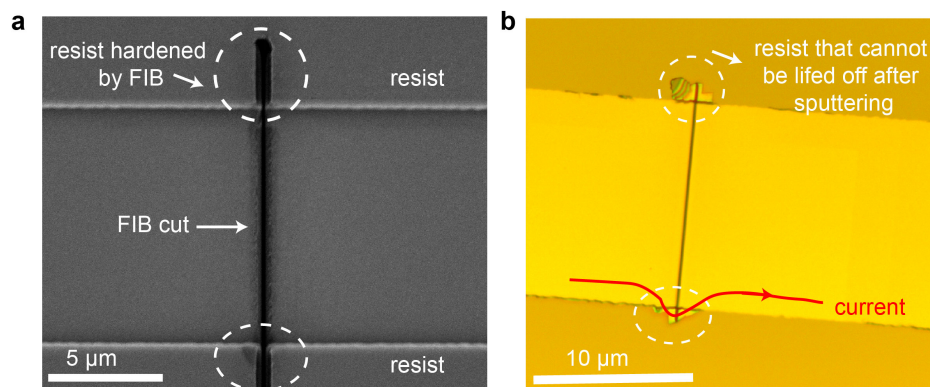


Fig. 5.6 The consequence of using FIB milling after the deposition of resist. (a) SEM image taken after FIB milling with resist around. (b) Optical microscopy image taken after metallisation: the region irradiated by FIB cannot be lifted off.

### Step 3: Spin-coating and patterning of double-layer resist

The double-layer resist was then patterned using optical lithography to open a narrow window on top of the trench and contacts (**Figure 5.5 d**). This step is used to limit the total area of the deposited thin film. The use of double-layer resist is essential for a clean lift-off after sputtering which is a non-directional deposition process. This can not be achieved using single-layer resist without the assistance of ultrasonic bath which will damage the 3D structure. A detailed comparison of the effects of single- and double-layer resist are given in **Figure 5.7**.

With the single layer resist used (**Figure 5.7 a-c**), as the sputtering technique employed here for incorporating multilayered materials is a non-directional deposition method, materials are deposited not only on top of the resist but also on side walls. Once a continuous film

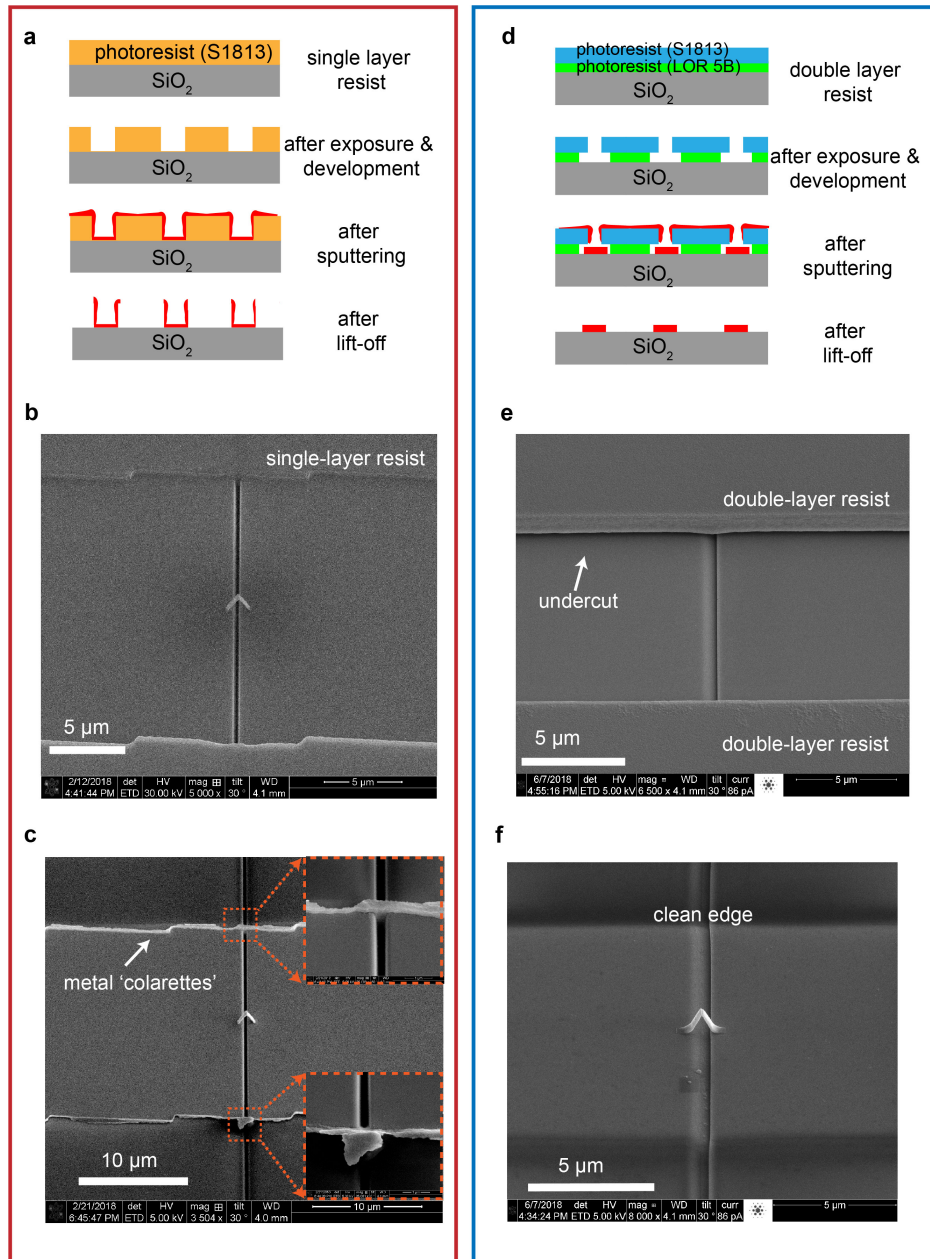


Fig. 5.7 Comparison between using single- and double- layer resist. (a) Schematics of using single layer resist. (b)-(c) SEM images taken before and after metallisation when using single layer resist. (d) Schematics of using double-layer resist. (e)-(f) SEM images taken before and after metallisation when using double-layer resist.

is formed, materials on side walls can not be removed together with the resist and result in significant lift off edges (metal 'colarettes') that will shunt the current. In contrast, double layer resist (Figure 5.7 d-e) can lead to the formation of an undercut. This is a consequence of the top layer resist (S1813) being light sensitive, while the under layer (LOR5B) only

being dissolved by direct contact with the developer entering through the opening of the top layer (**Figure 5.7 d**). The degree of the undercut is determined only by the dissolution time, and is not related to laser exposure dose. This undercut (**Figure 5.7 d, e**) ensures the deposition of a discontinuous film after sputtering and as shown in **Figure 5.7 f**, results in a clean edge without any shunting of the current. We also used a warm SVC 14 solution, which is a relatively strong resist stripper, to facilitate the lift-off process without utilising an ultrasonic bath.

#### Step 4: 3D non-magnetic scaffold fabricated by FEBID

Within the window opened, a non-magnetic 3D bridge was deposited across the trench via FEBID combined with the CAD implementation recently developed in our group [37]. In the same way as the 3D nanoramp shown in **section 5.1**, a non-magnetic precursor  $(\text{CH}_3)_3\text{Pt}(\text{C}_p\text{CH}_3)$  was used with electron beam's accelerating voltage and beam current set to be 30 kV and 21 pA, respectively. The CAD design of the bridge is shown in **Figure 5.8 a**. In contrast to the previous four-probe design used for the cobalt bridge, we chose the most basic shape of the bridge here. This is due to the fact that conformal deposition from PVD methods on high-aspect ratio structures is always a challenge [131], and to avoid potential disconnection of the thin film, we removed complex geometry parts such as the side-legs and also replaced the pointy top of the bridge with a flat top to improve the conformality of the film on the top part.

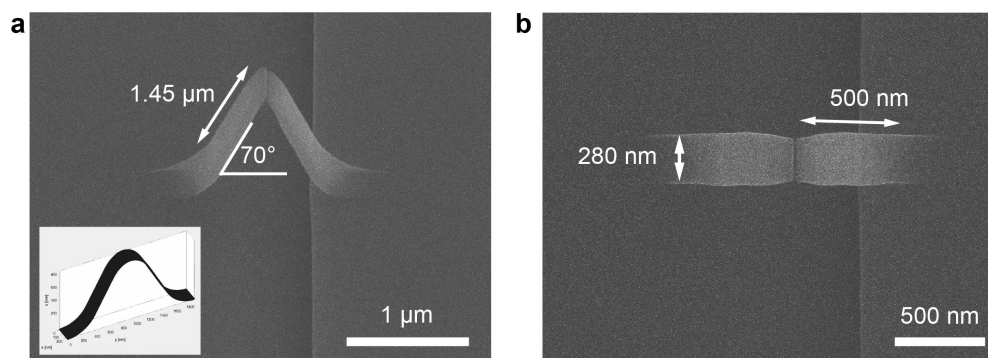


Fig. 5.8 *FEBID process. (a) SEM image of the printed Pt-C scaffold (stage tilt at 30°). Inset is the CAD design of the bridge. (b) Top view of the printed Pt-C bridge.*

To alleviate charging effects [77] during FEBID deposition, a layer of Ta/Pt (2/10 nm) was sputtered on top of the sample prior to deposition. The front and top view of the fabricated bridge scaffold (**Figure 5.8 a, b**) show that the legs of the fabricated bridge are 1.45  $\mu\text{m}$  long, 280 nm wide, forming an angle of 70° with the substrate. From the top view, we observe a reduced width and thickness with respect to the CAD design at the middle part of the bridge

where the two legs connect. This is due to the very shallow angle of that central part, which leads to a reduction in the number of secondary electrons generated and hence slows down the growth speed [81]. It is also challenging to fabricate shallow features repeatably with reduced number of electrons as the growth becomes more susceptible with small changes in experimental conditions [81, 132]. Further optimisation would be required for a better match with the design. However, this structure serves the purpose of this work effectively, which is to demonstrate the integration of multilayered material in a 3D nanomagnetic circuit.

### Step 5: Sputtering of multilayered materials and lift-off

Finally, a thin film of Ta/CoFeB/Ta (2/20/2 nm) was deposited with DC magnetron sputtering (**Figure 5.5 f**) and the resist was lifted off, leaving the 3D scaffold coated with the magnetic thin film and connected to the electrical contacts by the 2D magnetic tracks (**Figure 5.5 g**). The 3D nanomagnetic circuit achieved after lift off is shown in **Figure 5.9 a, b**, where we observe the resulting device: a 3D bridge spanning over a FIB milled trench and is connected into the electrical circuit. Details of the magnetotransport setup will be given in **section 5.2.3**.

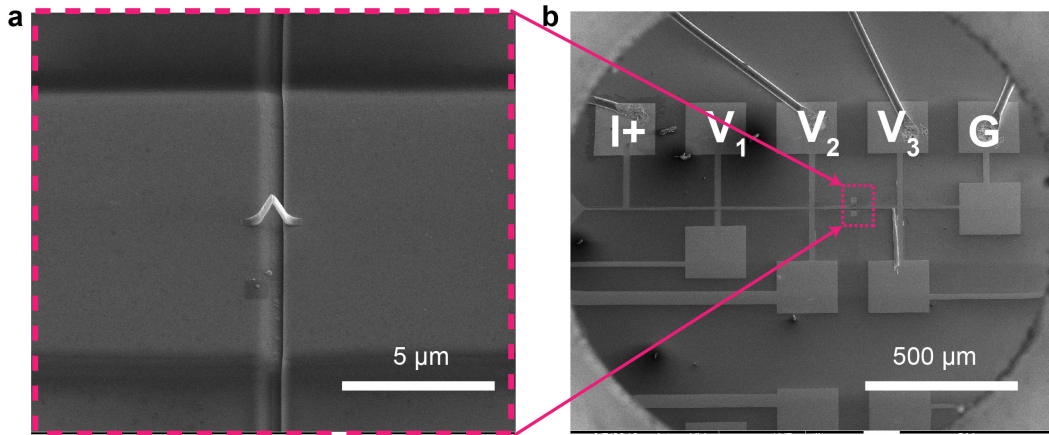


Fig. 5.9 3D nanomagnetic circuit. (a) Side view of the printed 3D nanomagnetic circuit (stage tilt equals to 30°). (b) Top view zoom-out of the printed 3D nanomagnetic circuit, showing the electrical pads, microwire bonds, and area (red square) where the bridge was fabricated. Current ( $I^+$ ), ground (G) and voltage (V) pads for magnetotransport measurements are indicated.



### 5.2.2 Electrical insulation verification of the FIB milled trench and the non-magnetic 3D scaffold.

The functionality of this magnetic 3D nanobridge relies on two primary factors: first, that the shunting of the current by 2D thin film is negligible, and second, that the 3D scaffold is non-conductive and the current flows primarily through the 3D magnetic layer. We determine whether this is the case by comparing the resistance measured across the fabricated magnetic nanobridge (**Figure 5.9 a, b**) which is around 30 k $\Omega$ , with two designed control structures.

First, we test whether the FIB milled trench successfully prevents shunting of current by repeating the fabrication process (**Figure 5.5**) without depositing the 3D bridge (step 4 is skipped). This test sample is shown in **Figure 5.10 a** and the two-probe I-V curve measured across the trench using a probe station with a Keithely 4200 SCS semiconductor system is shown in **Figure 5.10 b**. By measuring the slope, the resistance across the trench is calculated to be  $31.6 \pm 1.6$  G $\Omega$  which is six orders of magnitude higher than the resistance measured across the magnetic bridge. Hence, we conclude that the FIB cut provides enough insulation.

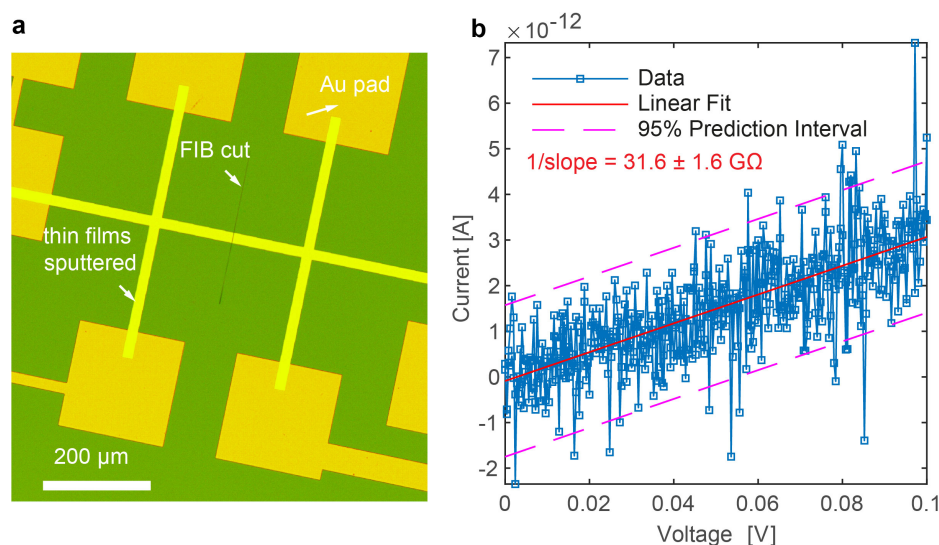


Fig. 5.10 *Electrical insulation verification of the trench. (a) An optical microscopy image of the FIB test device (without 3D bridge). (b) I-V curve measured across the FIB milled trench.*

Then we check that the resistivity of the Pt-C scaffold is much higher than the magnetic thin film. Another device was fabricated using the same process, but without sputtering the thin film (step 5 and 6 are skipped) so that we can measure the resistance of the Pt-C bridge scaffold (**Figure 5.11**). Three sweeps of voltage were applied, 0-3-0V, 0-7-0V and 0-10-0 V respectively (**Figure 5.11 a**). Since from the second sweep, we see permanent change of

the bridge, so we measure the differential resistivity of the bridge from the first sweep as shown in **Figure 5.11 b**. The decreasing resistivity with increasing voltage is the behaviour expected, as the Pt-C scaffold is essentially Pt inclusions in a carbonaceous matrix [38]. The minimum resistance of the Pt-C scaffold calculated is  $3 \text{ G}\Omega$  which is also significantly larger than the resistance measured across the bridge with magnetic thin film on top (specifically, five orders of magnitude higher). The corresponding resistivity of the scaffold is  $1.5 \times 10^9 \mu\Omega\text{cm}$ , which is in the range of reported values ( $10^6$  to  $10^{12} \mu\Omega\text{cm}$ ) for Pt-C structures grown using  $(\text{CH}_3)_3\text{Pt}(\text{C}_p\text{CH}_3)$  precursor [38]. Deformation of the bridge is observed clearly from the comparison of SEM images taken before and after the electrical tests (**Figure 5.11 c, d**) and this also proves that current flows through the bridge and hence demonstrates the effectiveness of the FIB trench.

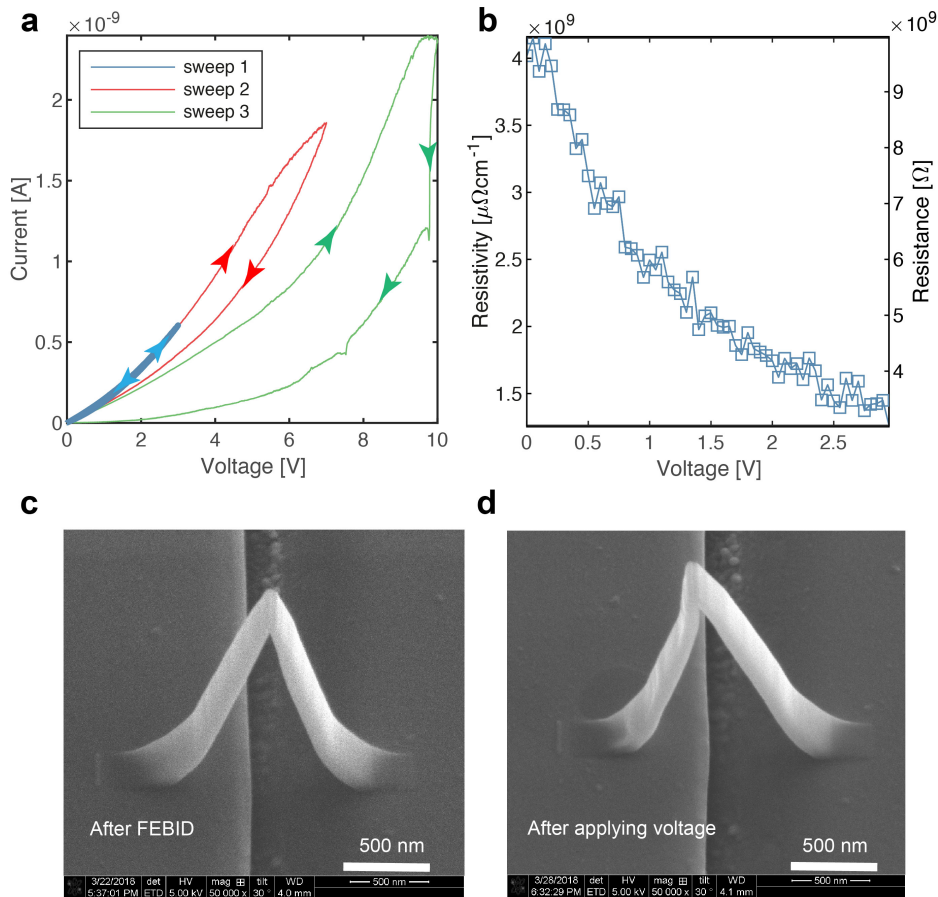


Fig. 5.11 Electrical insulation verification of the Pt-C scaffold. (a) I-V curves of 3 voltage sweeps applied across the Pt-C scaffold. (b) Differential resistivity calculated from the first sweep. (c)-(d) SEM images taken before and after applying a 10V voltage sweep.

### 5.2.3 Magnetotransport characterisation of the 3D device

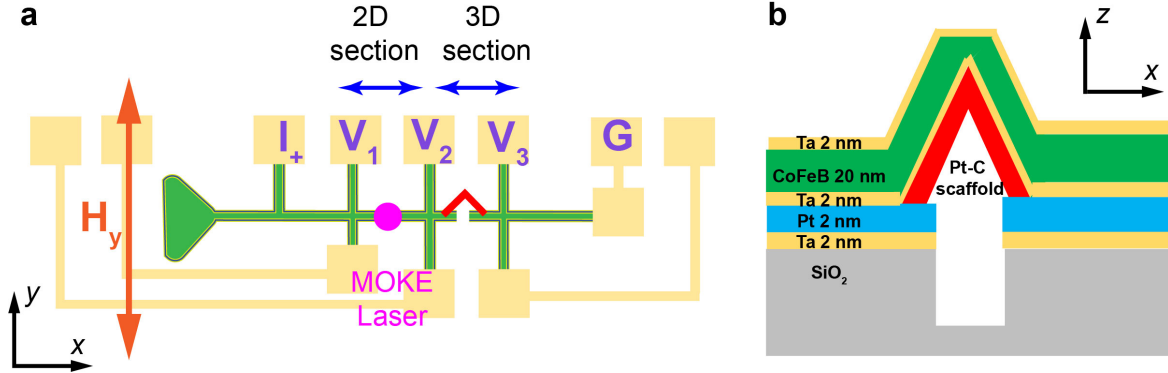


Fig. 5.12 (a) The schematic that shows the MOKE and MT measurement positions. (b) The schematic of the cross-section of the 3D device.

Following the validation of this fabrication process, we next consider the magneto-transport (MT) results obtained from the 3D nanomagnetic circuit. The measurement configuration is shown in **Figure 5.12 a**. A standard 4-terminal technique was used for the MT measurements, with an AC current of constant magnitude of  $2.5 \mu\text{A}$  supplied between  $I_+$  and  $G$ . Hence, the current flows along the long-axis of both the 2D magnetic track and the 3D bridge and an in-plane magnetic field  $H_y$  of up to 12 mT is applied perpendicular to the current direction. We measured not only the voltage drop across the 3D bridge section ( $V_2$ - $V_3$ ) but also the 2D track section ( $V_1$ - $V_2$ ). By comparing the two measurements, we can determine the magnetic and magneto-transport properties of the 3D nanobridge. In the same setup, both transverse and longitudinal Magneto-Optic Kerr Effect (MOKE) measurements were also taken for the 2D track section with a laser diameter of  $5 \mu\text{m}$  to obtain complementary information for the magnetisation reversal process of this region.

In this measurement geometry, we measured the longitudinal voltage along the current direction and hence probed the anisotropic magnetoresistance (AMR) which results in a change in the longitudinal electric field. This change depends on the angle between the current and magnetisation [60]:

$$\vec{E} = \rho_{\perp} \vec{J} + (\rho_{\parallel} - \rho_{\perp})(\vec{m} \cdot \vec{J})^2, \quad (5.1)$$

where  $\vec{E}$  is the electric field,  $\vec{J}$  is the current density vector,  $\vec{m}$  is a unit vector in the magnetisation direction,  $\rho_{\parallel}$  and  $\rho_{\perp}$  are the resistivities for  $\vec{J}$  parallel and perpendicular to  $\vec{m}$  and  $\frac{\rho_{\parallel} - \rho_{\perp}}{\rho_{\perp}}$  is the AMR ratio. The maximum magnetic field can be applied with this set-up is only 12 mT, hence magnon magnetoresistance is not considered. Again, to understand the



MT measurements, we need to access both  $\vec{m}$  and  $\vec{J}$ . The different resistivity of the layers in the multi-layered material (**Figure 5.12**), along with the 3D geometry, adds complexity to the current distribution in the system. Thus, to understand the experimental MT results we employed again the combination of micromagnetic simulations and a simulation based on finite element method to calculate voltage and current profiles, to take both the magnetic configuration and current distribution into account.

## 2D track section: MOKE and magnetotransport characterisations

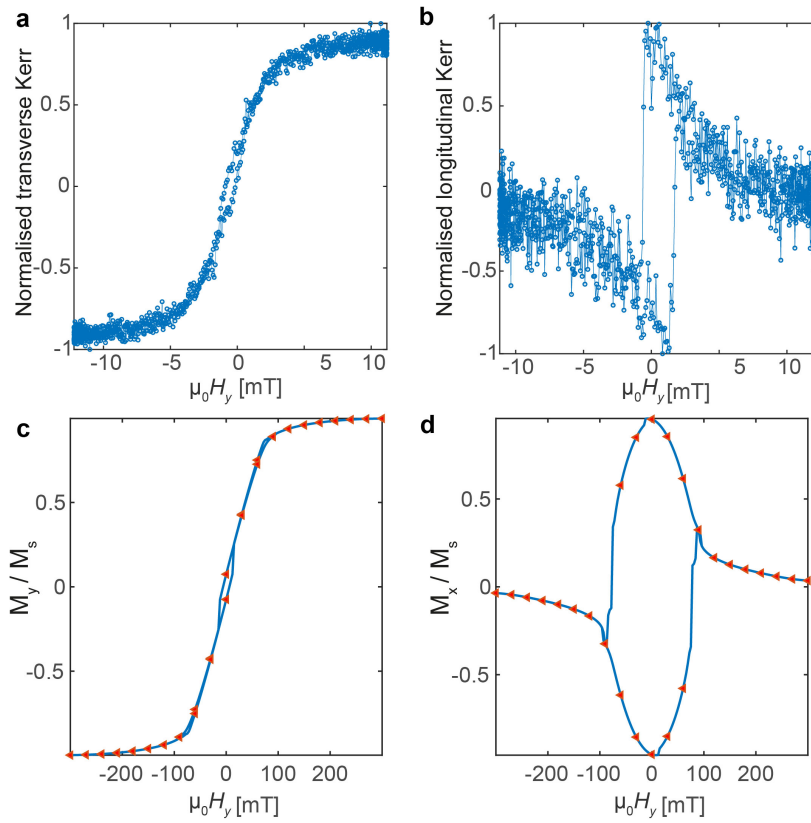


Fig. 5.13 2D track section: (a) Normalised transverse Kerr (proportional to  $M_y$ ). Error= $\pm 0.03$ . (b) Normalised longitudinal Kerr (proportional to  $M_y$ ). Error= $\pm 0.12$ . (c)-(d)  $M_y/M_s$  and  $M_x/M_s$  results from Mumax3 simulation.

First we consider the simpler part, the 2D track section without the nanobridge. For  $H_y$  applied perpendicular to the long axis of the 2D track, we have measured both the transverse Kerr signal ( $M_y/M_s$ ) and the longitudinal Kerr signal ( $M_x/M_s$ ) that provide access to the components of the magnetisation perpendicular and parallel to the current, respectively (**Figure 5.13 a, b**). As the field is applied along the hard axis, typical quasi-reversible  $M_y/M_s$  loops with a small coercive field of  $\approx 0.5$  mT are observed. On the other hand, the  $x$  component

of magnetisation (parallel to the easy axis) has a maximum at around 0 T and exhibits a progressive decrease on the approach to saturation, except for the sudden magnetisation reversal jumps at  $\mu_0 H_c \approx 2$  mT. These results indicate that in this area the magnetisation reversal in the  $y$  direction occurs by coherent rotation for a wide range of fields with the additional jumps observed in  $M_x$  consistent with a small  $H$ -misalignment with the hard axis [133].

In order to simulate the MT result later, we first run micromagnetic simulations to obtain the magnetisation switching profile. The actual volume of magnetic material in the 2D section is  $250 \mu\text{m} \times 15 \mu\text{m} \times 20 \text{nm}$  (aspect ratio:  $L/W = 15$ ), which is too large to perform micromagnetic simulations in a reasonable amount of time. Hence, we use a down-scaled model of size  $1024 \text{nm} \times 256 \text{nm} \times 20 \text{nm}$  ( $L/W = 4$ ). The shape anisotropy ( $K_s = \frac{1}{2} M_s^2 N$ , where  $M_s$  is the saturation magnetisation and  $N$  is the demagnetising factor along the long axis direction) of the real 2D track and the down-scaled model are  $760 \text{J/m}^3$  and  $9000 \text{J/m}^3$ , respectively. To compensate for this change of shape anisotropy associated with the changed aspect ratio, we include a uniaxial anisotropy term of  $K_u = 5000 \text{J/m}^3$  which is of the same order of magnitude with the change and gave the best agreement between simulations and experiments. Typical simulation parameters for CoFeB are used as following: mesh size = 5 nm,  $M_s = 8 \times 10^5 \text{A/m}$  and  $A_{ex} = 0.9 \times 10^{-11} \text{J/m}$  [134, 133]. Using this model, we obtain the  $M_y$  and  $M_x$  profiles as shown in **Figure 5.13 d, e** that qualitatively agree well with the experiment. This agreement confirms our understanding that the 2D track under  $H_y$  is switched primarily via coherent rotation.

After understand the switching process of the 2D track, we now consider its corresponding MT signal during reversal as shown in **Figure 5.14 a**. The peak we see at 0 T is consistent with the  $M_x$  measured since AMR is proportional to  $M_x^2$  (from Equation 5.1), given that CoFeB has a positive AMR ratio [133]. To simulate the MT signal we solve the electrical potential across the 2D track section using a FEM method with the mesh shown in **Figure 5.14 b** which takes into account both the Pt (deposited before FEBID to reduce charging effects) and CoFeB layers. For the Pt layer, we use a constant resistivity  $\rho_{Pt} = 30 \mu\Omega\text{cm}$  [135] and for the CoFeB layer, we use a magnetisation dependent resistivity tensor reformulated from Equation 5.1:

$$\rho_{CoFeB}(\mathbf{m}) = \begin{pmatrix} \rho_{\perp} + (\rho_{\parallel} - \rho_{\perp})m_x^2 & (\rho_{\parallel} - \rho_{\perp})m_x m_y & (\rho_{\parallel} - \rho_{\perp})m_x m_z \\ (\rho_{\parallel} - \rho_{\perp})m_x m_y & \rho_{\perp} + (\rho_{\parallel} - \rho_{\perp})m_y^2 & (\rho_{\parallel} - \rho_{\perp})m_y m_z \\ (\rho_{\parallel} - \rho_{\perp})m_x m_z & (\rho_{\parallel} - \rho_{\perp})m_y m_z & \rho_{\perp} + (\rho_{\parallel} - \rho_{\perp})m_z^2 \end{pmatrix} \quad (5.2)$$

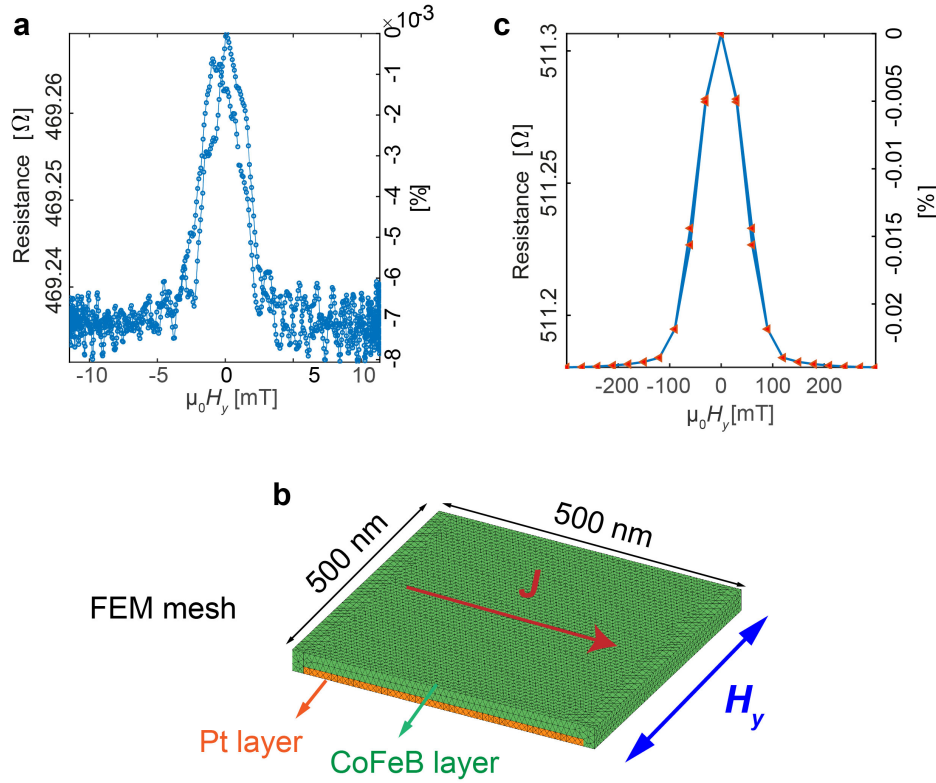


Fig. 5.14 Magnetotransport results of the 2D track section. (a) Magnetoresistance measured across the 2D track section (V2-V1). Error= $\pm 2$  mΩ. (b) The simulated MT result based on the combination of Mumax3 and FEM simulation. (c) The FEM mesh used for the 2D track section.

$m_x$ ,  $m_y$  and  $m_z$  are the x,y and z component of the magnetisation vector  $\mathbf{m}$  which are obtained from the previous simulation and we use  $\rho_{\perp}=230 \mu\Omega\text{cm}$  [133] and an AMR ratio of 0.15% [133]. Again to save computational time, the size of the FEM model was decreased ( $500 \text{ nm} \times 500 \text{ nm}$ ,  $L/W = 1$ ). To obtain a resistance that is comparable to the experimental results of the 2D track section, we scale up the quantitative FEM simulation results by a factor of 15 which accounts for the difference in aspect ratio between the real structure and the model.

The simulation results are shown in (Figure 5.14 c). The simulated resistance is around 510 Ω which agrees well with the data ( $\approx 469 \text{ Ω}$ ) and the peak we see at 0 T is also reproduced. The maximum percentage drops seen in the simulation and experiment are  $20 \times 10^{-3}\%$  and  $8 \times 10^{-3}\%$ , respectively. The drop in the simulation is about 2 times larger which may be due to the fact that we ignore the Ta layers in our FEM model. These layers will lead to a further reduction of the percentage change. Other factors such as the differences of AMR ratio between CoFeB alloys with different stoichiometry or microstructure may

also play a role. The good agreement between the simulation and experiments confirms our understanding of the switching process of the 2D section and the AMR contribution to the MT signal.

### 3D bridge section: magnetotransport results and simulations

After successfully reproducing the 2D track results, we move onto the 3D magnetic nanobridge. This section includes a 2D thin film track similar to the one studied in the preceding section, but with a FIB milled trench in the middle and a 3D nanobridge which essentially acts as a constriction [66] between two planar microwires. The MOKE signal from a 3D nanostructure such as the bridge is very challenging to obtain in comparison to a planar system and requires recently-developed techniques that exploit dark-field effects (see **section 5.1.2**). Furthermore, in our case, diffuse reflection originating from the FIB milled trench with a curved profile makes this approach unfeasible. Hence, we mainly interpret the MT results from the 3D section through its comparison with the 2D track and also the use of micromagnetic and FEM simulation.

The MT measurement of this section is shown in **Figure 5.15 a**. By comparing with the results obtained from the 2D track section (**Figure 5.14**), we see that by including a 3D bridge into the circuit, the hysteresis loop becomes asymmetric with non-saturating resistance at high fields and distinctive jumps observed around -5 mT. The non-saturating resistance indicates that the system is not fully switched by the applied magnetic field. Based on the results in the previous section, we know the 2D track section is saturated by these fields. Therefore, we infer that the 3D nanobridge is not fully switched due to the shape anisotropy. Furthermore, the jumps in the hysteresis loop are due to the formation of a domain wall between these two sections.

To assist our understanding of the MT results of the 3D section, we create an FEM model (**Figure 5.15 b**) that considers contributions from three parts: the 3D nanobridge (pink region), the 2D track (green) and the transition region between the 2D track and 3D bridge (purple). To obtain the corresponding resistivity tensor  $\rho(\mathbf{m})$  needed for each part of the FEM model, we again employ micromagnetic simulations. Specifically, for the 2D track section, the magnetisation profile that was confirmed in the previous section is used. The 3D bridge and transition region is modelled together as a nanowire with a square pad attached at the end, as shown in **Figure 5.15 c**. The same mesh size,  $M_s$  and  $A_{ex}$  are used for CoFeB as in the previous section [134, 133]. The AMR signal we studied in this experiment measures how much magnetisation deviates from the current direction. With a 12 mT in-plane field

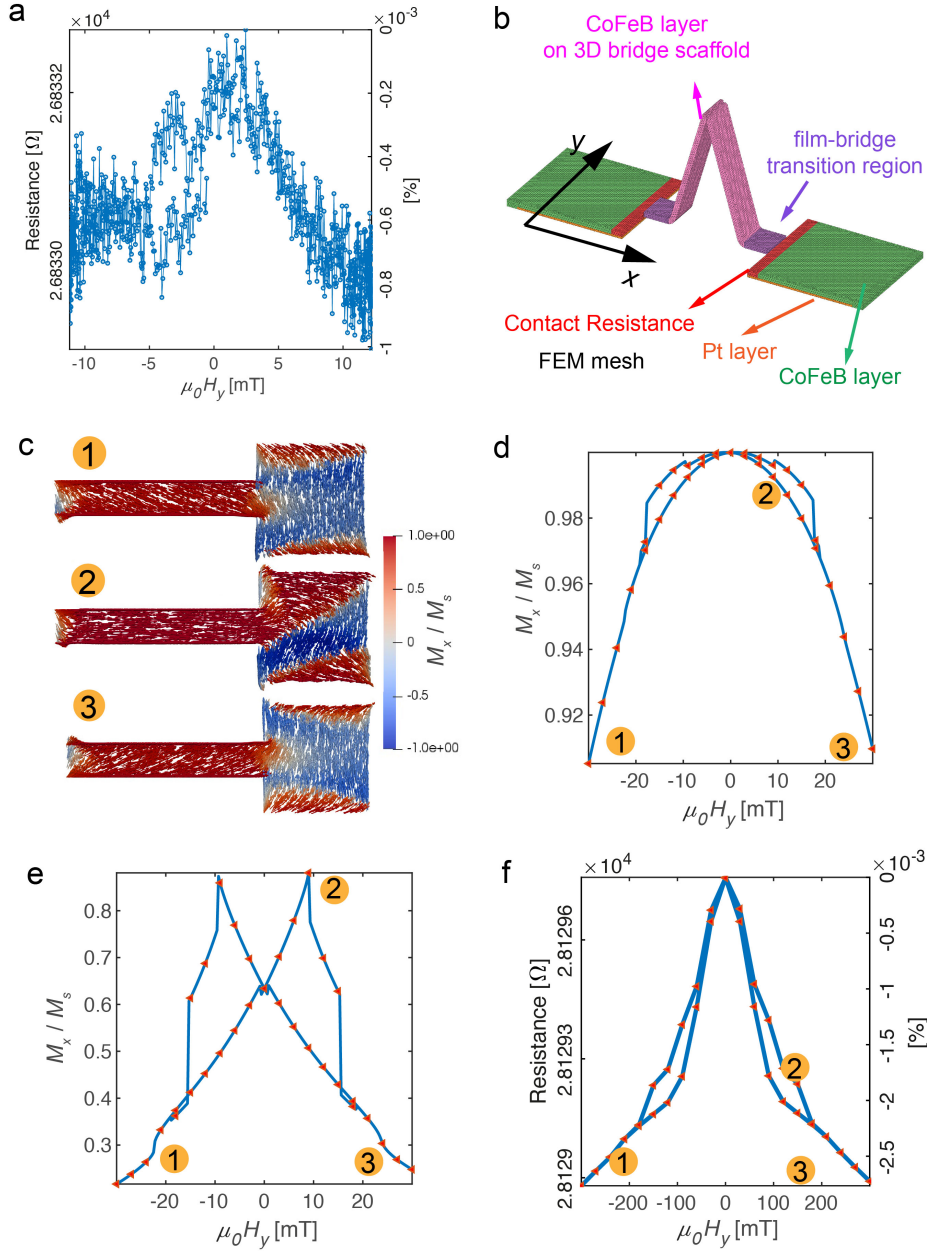


Fig. 5.15 3D bridge section: magnetotransport results and simulations. **(a)** Resistance measured across the 3D section (V3-V2). **(b)** FEM model of the 3D section that consists: 2D track, 3D bridge and 2D to 3D transition region. **(c)** Three magnetization states from the micromagnetic simulation for the combination of the 3D bridge and the transition region ( $M_x/M_s$  is plotted). **(d)** Simulation result of  $M_x/M_s$  for the nanowire section. **(e)** Simulation result of  $M_x/M_s$  for the transition section. **(f)** Simulated MT result based on the combination of Mumax3 and FEM simulation.

applied in the y-direction, the magnetisation remains aligned along the film plane due to shape anisotropy, which is also the current plane. Thus, the measured AMR only depends on the x-component of the magnetisation. **Figure 5.15 c** shows three magnetisation states at different fields with the x-component coloured, and the full simulated  $M_x/M_s$  hysteresis loops with a maximum  $H_y$  of 30 mT applied are plotted for the nanowire and pad section separately as shown in **Figure 5.15 d** and **Figure 5.15 e**. From **Figure 5.15 d**, we see the normalised  $M_x$  of the nanowire sections changes from 0.9 to 1, indicating that the wire has not been switched. On the other hand, from state 1 and state 3 shown in **Figure 5.15 c**, the transition area has mostly switched and the maximum  $M_x$  appears when two 90 degree domain walls are pinned in this region. By substituting these magnetisation profiles into the corresponding resistivity tensors, we obtain the magnetotransport simulation shown in **Figure 5.15 f**. This simulation result qualitatively reproduces the features from the data suggesting that the main drop in the signal is caused by the switching of the 2D film with low coercive fields. Furthermore, the non-saturating AMR is due to the wire not being fully switched and the small additional drop at  $\approx 5$  mT is a result of DW pinning in the transition area. The asymmetrical loop seen in the results could be potentially due to local stress-induced anisotropy caused by the 3D bridge during the deposition of thin films[136, 137].

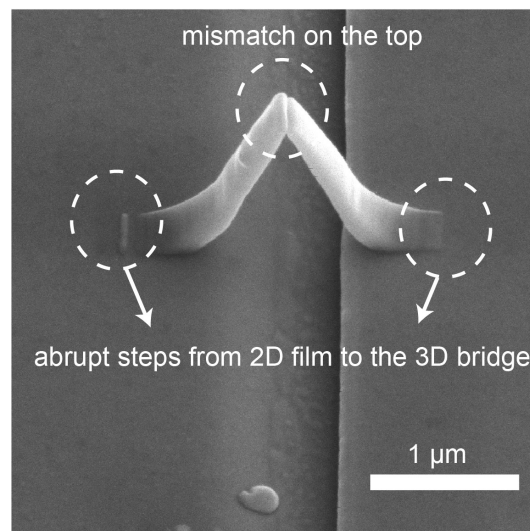


Fig. 5.16 The SEM image of the 3D nanomagnet created where the imperfections caused by Pt-C are shown in white circles.

We note that the measured resistance is about 28 k $\Omega$ , while the expected resistance of these sputtered materials is around 1 k $\Omega$ . The measured resistance is significantly higher which is most likely owing to imperfections in the Pt-C scaffold where a mismatch in the top region of the bridge is observed. In addition to the mismatch, there are abrupt changes in

surface height at the transition region between the 2D film and 3D bridge as shown in **Figure 5.16**. These abrupt steps lead to non-uniform step coverage and likely result in defects[131] in the sputtered thin films and hence a large contact resistance[138]. We have included a constant contact resistance of 27 k $\Omega$  in the FEM model to compensate this discrepancy in the measured and simulated resistance. The maximum percentage change due to AMR from the simulation is  $2.5 \times 10^{-3}\%$  and is  $1 \times 10^{-3}\%$  from the experiment. The percentage change simulated is the same order of magnitude with the experiment, which indicates that this unexpected large resistance is not from a magnetic source, and also that the 2D micromagnetic model is adequate to capture the essence of the switching process.

### 5.3 Chapter Summary

In this chapter, we employ a 'scaffold+sputtering' strategy to incorporate high quality multilayered materials into 3D nanomagnetic systems. We first used this method to create a simple nanoramp geometry and characterised it using the well established dark-field MOKE setup. By comparing the switching fields of the system's 2D and 3D components, we have demonstrated a functional 3D nanomagnetic device made with sputtered multilayered materials that allows domain wall movement between different planes.

Additionally, we developed a fabrication method for prototyping 3D spintronic devices with complex geometries and multi-layered materials. Specifically, to address the long-standing 'current shunt' issues related to PVD techniques, FIB milling and double-layered resist have been employed. We demonstrated this new method through the creation of a 3D nanomagnetic circuit that integrates sputtered Ta/CoFeB/Ta multilayer onto a 3D nanobridge. By comparing the magnetotransport results from both the 2D and 3D sections aided by micromagnetic and FEM simulations, we verified that the 3D nanomagnet has been connected into the 2D circuits successfully and observed domain wall pinning at the 2D and 3D transition area. The principle of this method can be extended to other materials and geometries, leading to a wide range of opportunities for the exploitation of the interplay between 3D geometry, multilayered materials and magnetotransport.



# Chapter 6

## Conclusions and Outlook

The aim of this thesis was to provide the first steps to address some major challenges in the study of 3D spintronics, including the integration of 3D nanomagnets into circuits, the development of magnetotransport (MT) characterisation strategies for 3D circuits, and of new protocols for the understanding of complex experimental results. Toward this end, we presented the realisation of two types of 3D nanomagnetic circuits, emphasising the inclusion of complex geometries and advanced materials, respectively, as well as the investigation of both types of 3D circuits using MT measurements and various simulation tools, and finally, some insights into the influence of a 3D geometry on the MT effects.

The first type of nanomagnetic circuit, as illustrated in **chapter 3**, was created by exploiting the direct-writing capability of focused electron beam induced deposition to 3D-print high purity ferromagnetic nanostructures onto pre-patterned planar electrical contacts directly. This method not only allows for greater flexibility in the design of 3D geometries, but it also eliminates the need for an extra step for the electrical connection, and hence is ideal for the exploration of 3D geometrical effects on magnetoelectrical signals. Using this method, a 3D cobalt nanobridge was integrated into a microelectronic circuit with an efficient design of contacts that allowed simultaneous measurements of longitudinal and transverse signals, and for the first time, this circuit demonstrated how the combination of a non-trivial 3D geometry and electrical contacts with respect to it plays a key role in the behaviour of MT measurements.

**In chapter 3**, through a detailed angular dependence study of MT signals on high magnetic fields and the aid of macrospin and finite element modelling (FEM), we have disentangled and understood key magnetotransport effects including Hall effects and magnetoresistance signals, and obtain a clear understanding of their magnitudes and angular

dependencies as a function of the field direction. Furthermore, we discovered that the 3D geometry of the magnetic nanostructure influenced the magnetoelectrical signals in two major ways. First, the 3D vector nature of both magnetisation and current induces deviations of the Hall effects' signal from the standard angular dependence observed in planar geometries. The reason behind this is signals that, e.g., cancel out in planar geometries may add up in 3D. Second, there is a significant angular-dependent magnon magnetoresistance contribution due to varying magnetostatic interactions throughout a 3D circuit which are not present in a standard planar magnetic device.

In **chapter 4**, building upon the understanding of the various magnetotransport effects obtained from the high-field study (**chapter 2**), we investigated the magnetisation reversal processes of the same nanobridge at low magnetic fields. We observed both deterministic and stochastic switching events on the same structure for fields applied in different directions. With the combination of micromagnetic and FEM simulations, we were able to identify the potential types of magnetic states involved. In this study, we saw how 3D geometries could lead to unexpected magnetoelectrical signals through the complex internal magnetic configurations that are only available in 3D structures due to the higher degrees of freedom. The magnetoelectrical responses of these states are of technological interest in sensing and information processing applications.

**Chapter 5** focused on the second type of 3D nanomagnetic systems investigated in this thesis, where high quality multilayered materials are introduced using a 'non-magnetic scaffold + sputtering' strategy. First, a functional 3D nanomagnetic ramp using multilayered materials that allows domain wall movements between different planes under external fields was demonstrated using a dark-field MOKE setup. Then, a multi-technique fabrication method for prototyping 3D spintronic devices with complex geometries and multilayered materials was developed. Specifically, the long-standing 'current shunt' issues related to the full coverage characteristics of physical vapour deposition techniques were solved with the use of focused ion beam milling and double-layered resist. A 3D nanobridge with sputtered Ta-CoFeB-Ta on top was successfully connected into a circuit, which was verified by comparing the MT results of both the 2D and 3D sections with the aid of micromagnetic and FEM simulations. The principle of this method can be extended to other materials and geometries, leading to a wide range of opportunities for the exploitation of the interplay between 3D geometry, multilayered materials and magnetotransport.

These works represent an important step forward for the field of 3D spintronics, demonstrating the potential of the field and how our technical capabilities now provide the foundation for exploring complex spintronic effects emerging in three dimensions and long term, the realisation of 3D devices. Following on this work, where 3D nanobridges were mainly investigated, there are a number of magnetic systems that would be interesting to study further. The interplay between geometry and magnetotransport could be further explored in a system where curvature and chirality are introduced, such as a double helix. As for the materials aspects, since the incorporation of multilayered materials into 3D circuits is now possible, the introduction of advanced materials such as the one that can support smaller topologically-protected spin textures like Skrymions would be of great interest and trigger new device concepts based on the interaction of such 3D spin textures with 3D shape anisotropy. In addition to developing new systems with more complex geometries or materials, the simulation tools could be improved as well. Throughout this work, a combination of magnetic and finite element modelling was employed to provide a fast and efficient understanding of the MT measurements of the nanobridges which are mainly made up of straight segments. However, to deal with MT study of more complex geometries, a systematic approach to multi-physics extensions of finite-element based micromagnetic simulations is needed. Finally, our 3D nanomagnetic circuits were all investigated under external fields. A natural step forward is to demonstrate the full electrical control of the 3D nanomagnets for their potential implementation in dense and large-scale chips.



# References

- [1] A. Hoffmann and S. D. Bader, “Opportunities at the Frontiers of Spintronics,” Physical Review Applied, vol. 4, no. 4, p. 047001, 2015.
- [2] W. Thomson, “XIX. On the electro-dynamic qualities of metals: Effects of magnetization on the electric conductivity of nickel and of iron,” Proceedings of the Royal Society of London, vol. 8, no. 8, pp. 546–550, 1857.
- [3] C. Tsang, M.-M. Chen, T. Yogi, and K. Ju, “Gigabit density recording using dual-element mr/inductive heads on thin-film disks,” IEEE Transactions on Magnetics, vol. 26, no. 5, pp. 1689–1693, 1990.
- [4] M. N. Baibich, J. M. Broto, A. Fert, F. N. V. Dau, and F. Petroff, “Giant Magnetoresistance of (001)Fe/(001)Cr Magnetic Superlattices,” Physical Review Letters, vol. 61, no. 21, pp. 2472–2475, 1988.
- [5] G. Binasch, P. Grünberg, F. Saurenbach, and W. Zinn, “Enhanced magnetoresistance in layered magnetic structures with antiferromagnetic interlayer exchange,” Physical Review B, vol. 39, pp. 4828–4830, 03 1989.
- [6] E. E. Fullerton and J. R. Childress, “Spintronics, Magnetoresistive Heads, and the Emergence of the Digital World,” Proceedings of the IEEE, vol. 104, no. 10, pp. 1787–1795, 2016.
- [7] S. Bader and S. Parkin, “Spintronics,” Annual Review of Condensed Matter Physics, vol. 1, no. 1, pp. 71–88, 2010.
- [8] B. Dieny, I. L. Prejbeanu, K. Garello, P. Gambardella, P. Freitas, R. Lehnendorff, W. Raberg, U. Ebels, S. O. Demokritov, J. Akerman, A. Deac, P. Pirro, C. Adelman, A. Anane, A. V. Chumak, A. Hirohata, S. Mangin, S. O. Valenzuela, M. C. Onbaşlı, M. d’Aquino, G. Prenat, G. Finocchio, L. Lopez-Diaz, R. Chantrell, O. Chubykalo-Fesenko, and P. Bortolotti, “Opportunities and challenges for spintronics in the micro-electronics industry,” Nature Electronics, vol. 3, no. 8, pp. 446–459, 2020.
- [9] E. Pop, S. Sinha, and K. Goodson, “Heat Generation and Transport in Nanometer-Scale Transistors,” Proceedings of the IEEE, vol. 94, no. 8, pp. 1587–1601, 2006.
- [10] P. Barla, V. K. Joshi, and S. Bhat, “Spintronic devices: a promising alternative to CMOS devices,” Journal of Computational Electronics, vol. 20, no. 2, pp. 805–837, 2021.

- [11] A. D. Kent and D. C. Worledge, “A new spin on magnetic memories,” Nature Nanotechnology, vol. 10, no. 3, pp. 187–191, 2015.
- [12] I. Eichwald, S. Breitzkreutz, G. Ziemys, G. Csaba, W. Porod, and M. Becherer, “Majority logic gate for 3D magnetic computing,” Nanotechnology, vol. 25, no. 33, p. 335202, 2014.
- [13] D. A. Allwood, G. Xiong, C. C. Faulkner, D. Atkinson, D. Petit, and R. P. Cowburn, “Magnetic Domain-Wall Logic,” Science, vol. 309, no. 5741, pp. 1688–1692, 2005.
- [14] T. Fischer, M. Kewenig, D. A. Bozhko, A. A. Serga, I. I. Syvorotka, F. Ciubotaru, C. Adelmann, B. Hillebrands, and A. V. Chumak, “Experimental prototype of a spin-wave majority gate,” Applied Physics Letters, vol. 110, no. 15, p. 152401, 2017.
- [15] T. Brächer and P. Pirro, “An analog magnon adder for all-magnonic neurons,” Journal of Applied Physics, vol. 124, no. 15, p. 152119, 2018.
- [16] R. W. Dawidek, T. J. Hayward, I. T. Vidamour, T. J. Broomhall, G. Venkat, M. A. Mamoori, A. Mullen, S. J. Kyle, P. W. Fry, N. Steinke, J. F. K. Cooper, F. Maccherozzi, S. S. Dhesi, L. Aballe, M. Foerster, J. Prat, E. Vasilaki, M. O. A. Ellis, and D. A. Allwood, “Dynamically Driven Emergence in a Nanomagnetic System,” Advanced Functional Materials, vol. 31, no. 15, p. 2008389, 2021.
- [17] A. Fernández-Pacheco, R. Streubel, O. Fruchart, R. Hertel, P. Fischer, and R. P. Cowburn, “Three-dimensional nanomagnetism,” Nature Communications, vol. 8, no. 1, p. 15756, 2017.
- [18] S. S. P. Parkin, M. Hayashi, and L. Thomas, “Magnetic Domain-Wall Racetrack Memory,” Science, vol. 320, no. 5873, pp. 190–194, 2008.
- [19] A. May, M. Hunt, A. V. D. Berg, A. Hejazi, and S. Ladak, “Realisation of a frustrated 3D magnetic nanowire lattice,” Communications Physics, vol. 2, no. 1, p. 13, 2019.
- [20] R. Lavrijsen, J.-H. Lee, A. Fernández-Pacheco, D. C. M. C. Petit, R. Mansell, and R. P. Cowburn, “Magnetic ratchet for three-dimensional spintronic memory and logic,” Nature, vol. 493, no. 7434, pp. 647–650, 2013.
- [21] J. Torrejon, M. Riou, F. A. Araujo, S. Tsunegi, G. Khalsa, D. Querlioz, P. Bortolotti, V. Cros, K. Yakushiji, A. Fukushima, H. Kubota, S. Yuasa, M. D. Stiles, and J. Grollier, “Neuromorphic computing with nanoscale spintronic oscillators,” Nature, vol. 547, no. 7664, pp. 428–431, 2017.
- [22] P. Fischer, D. Sanz-Hernández, R. Streubel, and A. Fernández-Pacheco, “Launching a new dimension with 3D magnetic nanostructures,” APL Materials, vol. 8, no. 1, p. 010701, 2020.
- [23] R. Streubel, P. Fischer, F. Kronast, V. P. Kravchuk, D. D. Sheka, Y. Gaididei, O. G. Schmidt, and D. Makarov, “Magnetism in curved geometries,” Journal of Physics D: Applied Physics, vol. 49, no. 36, p. 363001, 2016.

- [24] S. D. Col, S. Jamet, N. Rougemaille, A. Locatelli, T. O. Mentès, B. S. Burgos, R. Afid, M. Darques, L. Cagnon, J. C. Toussaint, and O. Fruchart, “Observation of Bloch-point domain walls in cylindrical magnetic nanowires,” *Physical Review B*, vol. 89, no. 18, p. 180405, 2014.
- [25] R. Streubel, L. Han, F. Kronast, A. A. Ünal, O. G. Schmidt, and D. Makarov, “Imaging of Buried 3D Magnetic Rolled-up Nanomembranes,” *Nano Letters*, vol. 14, no. 7, pp. 3981–3986, 2014.
- [26] M. Schöbitz, A. D. Riz, S. Martin, S. Bochmann, C. Thirion, J. Vogel, M. Foerster, L. Aballe, T. O. Mentès, A. Locatelli, F. Genuzio, S. Le-Denmat, L. Cagnon, J. C. Toussaint, D. Gusakova, J. Bachmann, and O. Fruchart, “Fast Domain Wall Motion Governed by Topology and Ørsted Fields in Cylindrical Magnetic Nanowires,” *Physical Review Letters*, vol. 123, no. 21, p. 217201, 2019.
- [27] F. Balhorn, S. Mansfeld, A. Krohn, J. Topp, W. Hansen, D. Heitmann, and S. Mendach, “Spin-Wave Interference in Three-Dimensional Rolled-Up Ferromagnetic Microtubes,” *Physical Review Letters*, vol. 104, no. 3, p. 037205, 2010.
- [28] D. E. Nikonov, S. Manipatruni, and I. A. Young, “Automotion of domain walls for spintronic interconnects,” *Journal of Applied Physics*, vol. 115, no. 21, p. 213902, 2014.
- [29] R. Hertel, “Curvature-induced magnetochirality,” *SPIN*, vol. 03, no. 03, p. 1340009, 2013.
- [30] D. D. Sheka, “A perspective on curvilinear magnetism,” *Applied Physics Letters*, vol. 118, no. 23, p. 230502, 2021.
- [31] D. Sanz-Hernández, A. Hierro-Rodriguez, C. Donnelly, J. Pablo-Navarro, A. Sorrentino, E. Pereiro, C. Magén, S. McVitie, J. M. d. Teresa, S. Ferrer, P. Fischer, and A. Fernández-Pacheco, “Artificial Double-Helix for Geometrical Control of Magnetic Chirality,” *ACS Nano*, vol. 14, no. 7, pp. 8084–8092, 2020.
- [32] C. A. Ross, K. K. Berggren, J. Y. Cheng, Y. S. Jung, and J. Chang, “Three-Dimensional Nanofabrication by Block Copolymer Self-Assembly,” *Advanced Materials*, vol. 26, no. 25, pp. 4386–4396, 2014.
- [33] J. Llandro, D. M. Love, A. Kovács, J. Caron, K. N. Vyas, A. Kákay, R. Salikhov, K. Lenz, J. Fassbender, M. R. J. Scherer, C. Ciorra, U. Steiner, C. H. W. Barnes, R. E. Dunin-Borkowski, S. Fukami, and H. Ohno, “Visualizing Magnetic Structure in 3D Nanoscale Ni–Fe Gyroid Networks,” *Nano Letters*, vol. 20, no. 5, pp. 3642–3650, 2020.
- [34] C. Müller, C. C. B. Bufon, M. E. N. Fuentes, D. Makarov, D. H. Mosca, and O. G. Schmidt, “Towards compact three-dimensional magnetoelectronics—Magnetoresistance in rolled-up Co/Cu nanomembranes,” *Applied Physics Letters*, vol. 100, no. 2, p. 022409, 2012.

- [35] I. M. dotonch, D. Makarov, R. Koseva, L. Baraban, D. Karnaushenko, C. Kaiser, K.-F. Arndt, and O. G. Schmidt, "Rolled-Up Magnetic Sensor: Nanomembrane Architecture for In-Flow Detection of Magnetic Objects," *ACS Nano*, vol. 5, no. 9, pp. 7436–7442, 2011.
- [36] A. Fernández-Pacheco, L. Skoric, J. M. D. Teresa, J. Pablo-Navarro, M. Huth, and O. V. Dobrovolskiy, "Writing 3D Nanomagnets Using Focused Electron Beams," *Materials*, vol. 13, no. 17, p. 3774, 2020.
- [37] L. Skoric, D. Sanz-Hernández, F. Meng, C. Donnelly, S. Merino-Aceituno, and A. Fernández-Pacheco, "Layer-by-Layer Growth of Complex-Shaped Three-Dimensional Nanostructures with Focused Electron Beams," *Nano Letters*, vol. 20, no. 1, pp. 184–191, 2019.
- [38] A. Fernández-Pacheco, J. M. D. Teresa, R. Córdoba, and M. R. Ibarra, "Magnetotransport properties of high-quality cobalt nanowires grown by focused-electron-beam-induced deposition," *Journal of Physics D: Applied Physics*, vol. 42, no. 5, p. 055005, 2009.
- [39] R. Córdoba, R. Lavrijsen, A. Fernández-Pacheco, M. R. Ibarra, F. Schoenaker, T. Ellis, B. Barcones-Campo, J. T. Kohlhepp, H. J. M. Swagten, B. Koopmans, J. J. L. Mulders, and J. M. D. Teresa, "Giant anomalous Hall effect in Fe-based microwires grown by focused-electron-beam-induced deposition," *Journal of Physics D: Applied Physics*, vol. 45, no. 3, 2012.
- [40] J. M. D. Teresa, A. Fernández-Pacheco, R. Córdoba, L. Serrano-Ramón, S. Sangiao, and M. R. Ibarra, "Review of magnetic nanostructures grown by focused electron beam induced deposition (FEBID)," *Journal of Physics D: Applied Physics*, vol. 49, no. 24, p. 243003, 2016.
- [41] C. Donnelly, M. Guizar-Sicairos, V. Scagnoli, M. Holler, T. Huthwelker, A. Menzel, I. Vartiainen, E. Müller, E. Kirk, S. Gliga, J. Raabe, and L. J. Heyderman, "Element-Specific X-Ray Phase Tomography of 3D Structures at the Nanoscale," *Physical Review Letters*, vol. 114, no. 11, p. 115501, 2015.
- [42] M. Albrecht, G. Hu, I. L. Guhr, T. C. Ulbrich, J. Boneberg, P. Leiderer, and G. Schatz, "Magnetic multilayers on nanospheres," *Nature Materials*, vol. 4, no. 3, pp. 203–206, 2005.
- [43] D. Sanz-Hernandez, R. F. Hamans, J.-W. Liao, A. Welbourne, R. Lavrijsen, and A. Fernandez-Pacheco, "Fabrication, Detection, and Operation of a Three-Dimensional Nanomagnetic Conduit," *ACS Nano*, vol. 11, pp. 11066–11073, 11 2017. doi: 10.1021/acsnano.7b05105.
- [44] H. Maurenbrecher, J. Mendil, G. Chatzipirpiridis, M. Mattmann, S. Pané, B. J. Nelson, and P. Gambardella, "Chiral anisotropic magnetoresistance of ferromagnetic helices," *Applied Physics Letters*, vol. 112, no. 24, p. 242401, 2018.
- [45] J. D. Coey and J. Coey, *Magnetism and Magnetic Materials*. Cambridge University Press, 2010.



- [46] W. Heisenberg, “Zur Theorie des Ferromagnetismus,” Zeitschrift für Physik, vol. 49, no. 9-10, pp. 619–636, 1928.
- [47] W. F. Brown, “Theory of the Approach to Magnetic Saturation,” Physical Review, vol. 58, no. 8, pp. 736–743, 1940.
- [48] A. Hubert and R. Schäfer, Magnetic domains: the analysis of magnetic microstructures. Springer Science & Business Media, 2008.
- [49] E. Raymenants, O. Bultynck, D. Wan, T. Devolder, K. Garello, L. Souriau, A. Thiam, D. Tsvetanova, Y. Canvel, D. E. Nikonov, I. A. Young, M. Heyns, B. Soree, I. Asselberghs, I. Radu, S. Couet, and V. D. Nguyen, “Nanoscale domain wall devices with magnetic tunnel junction read and write,” Nature Electronics, vol. 4, no. 6, pp. 392–398, 2021.
- [50] M. Staño and O. Fruchart, “Magnetic nanowires and nanotubes,” in Handbook of Magnetic Materials, vol. 27, pp. 155–267, Elsevier, 2018.
- [51] O. Boulle, G. Malinowski, and M. Kläui, “Current-induced domain wall motion in nanoscale ferromagnetic elements,” Materials Science and Engineering: R: Reports, vol. 72, no. 9, pp. 159–187, 2011.
- [52] R. Hertel, “Computational micromagnetism of magnetization processes in nickel nanowires,” Journal of Magnetism and Magnetic Materials, vol. 249, no. 1-2, pp. 251–256, 2002.
- [53] L. Landau and E. Lifshitz, “On the theory of magnetic permeability dispersion in ferromagnetic solids,” Sov. Phys., vol. 8, pp. 153–166, 1935.
- [54] T. Gilbert, “A phenomenological theory of damping in ferromagnetic materials,” IEEE Transactions on Magnetics, vol. 40, no. 6, pp. 3443–3449, 2004.
- [55] A. Vansteenkiste, J. Leliaert, M. Dvornik, F. Garcia-Sanchez, and B. V. Waeyenberge, “The design and verification of Mumax3,” arXiv, 2014.
- [56] C. Abert, L. Exl, F. Bruckner, A. Drews, and D. Suess, “magnum.fe: A micromagnetic finite-element simulation code based on FEniCS,” Journal of Magnetism and Magnetic Materials, vol. 345, pp. 29–35, 2013.
- [57] J. Leliaert and J. Mulkers, “Tomorrow’s micromagnetic simulations,” Journal of Applied Physics, vol. 125, no. 18, p. 180901, 2019.
- [58] E. C. Stoner and E. Wohlfarth, “A mechanism of magnetic hysteresis in heterogeneous alloys,” Philosophical Transactions of the Royal Society of London. Series A, Mathematical and Physical Sciences, vol. 240, no. 826, pp. 599–642, 1948.
- [59] B. Raquet, M. Viret, E. Sondergard, O. Cespedes, and R. Mamy, “Electron-magnon scattering and magnetic resistivity in 3d ferromagnets,” Physical Review B, vol. 66, no. 2, p. 024433, 2002.
- [60] I. Campbell and A. Fert, “Handbook of Ferromagnetic Materials,” vol. 3, pp. 747–804, 1982.

- [61] F. Meng, C. Donnelly, C. Abert, L. Skoric, S. Holmes, Z. Xiao, J.-W. Liao, P. J. Newton, C. H. W. Barnes, D. Sanz-Hernández, A. Hierro-Rodriguez, D. Suess, R. P. Cowburn, and A. Fernández-Pacheco, “Non-Planar Geometrical Effects on the Magnetoelectrical Signal in a Three-Dimensional Nanomagnetic Circuit,” *ACS Nano*, vol. 15, no. 4, pp. 6765–6773, 2021.
- [62] J. Smit, “Magnetoresistance of ferromagnetic metals and alloys at low temperatures,” *Physica*, vol. 17, no. 6, pp. 612–627, 1951.
- [63] T. McGuire and R. Potter, “Anisotropic magnetoresistance in ferromagnetic 3d alloys,” *IEEE Transactions on Magnetics*, vol. 11, no. 4, pp. 1018–1038, 1975.
- [64] J.-P. Jan, “Galvamomagnetic and thermomagnetic effects in metals,” *Solid State Physics*, vol. 5, pp. 1–96, 1957.
- [65] J.-E. Wegrowe, D. Kelly, A. Franck, S. E. Gilbert, and J.-P. Ansermet, “Magnetoresistance of Ferromagnetic Nanowires,” *Physical Review Letters*, vol. 82, no. 18, pp. 3681–3684, 1999.
- [66] M. Kläui, C. A. F. Vaz, J. A. C. Bland, W. Wernsdorfer, G. Faini, and E. Cambril, “Domain wall pinning and controlled magnetic switching in narrow ferromagnetic ring structures with notches (invited),” *Journal of Applied Physics*, vol. 93, no. 10, pp. 7885–7890, 2003.
- [67] M. Hayashi, L. Thomas, C. Rettner, R. Moriya, X. Jiang, and S. S. P. Parkin, “Dependence of Current and Field Driven Depinning of Domain Walls on Their Structure and Chirality in Permalloy Nanowires,” *Physical Review Letters*, vol. 97, no. 20, p. 207205, 2006.
- [68] N. Nagaosa, J. Sinova, S. Onoda, A. H. MacDonald, and N. P. Ong, “Anomalous Hall effect,” *Reviews of Modern Physics*, vol. 82, no. 2, 2010.
- [69] D. Ravelosona, D. Lacour, J. A. Katine, B. D. Terris, and C. Chappert, “Nanometer Scale Observation of High Efficiency Thermally Assisted Current-Driven Domain Wall Depinning,” *Physical Review Letters*, vol. 95, no. 11, p. 117203, 2005.
- [70] F. Cayssol, D. Ravelosona, J. Wunderlich, C. Chappert, V. Mathet, J.-P. Jamet, and J. Ferré, “Detection of domain wall propagation in a mesoscopic wire,” *Journal of Magnetism and Magnetic Materials*, vol. 240, no. 1-3, pp. 30–33, 2002.
- [71] A. V. Chumak, V. I. Vasyuchka, A. A. Serga, and B. Hillebrands, “Magnon spintronics,” *Nature Physics*, vol. 11, no. 6, pp. 453–461, 2015.
- [72] V. D. Nguyen, C. Naylor, L. Vila, A. Marty, P. Laczkowski, C. Beigné, L. Notin, Z. Ishaque, and J. P. Attané, “Magnon magnetoresistance of NiFe nanowires: Size dependence and domain wall detection,” *Applied Physics Letters*, vol. 99, no. 26, p. 262504, 2011.
- [73] A. P. Mihai, J. P. Attané, A. Marty, P. Warin, and Y. Samson, “Electron-magnon diffusion and magnetization reversal detection in FePt thin films,” *Physical Review B*, vol. 77, no. 6, p. 060401, 2008.

- [74] A. Fernandez-Pacheco, Studies of Nanoconstrictions, Nanowires and Fe<sub>3</sub>O<sub>4</sub> Thin Films: Electrical Conduction and Magnetic Properties. Fabrication by Focused Electron/Ion Beam. Springer Science & Business Media, 2011.
- [75] R. F. Pease and S. Y. Chou, “Lithography and other patterning techniques for future electronics,” Proceedings of the IEEE, vol. 96, no. 2, pp. 248–270, 2008.
- [76] K. Seshan, Handbook of Thin Film Deposition Techniques Principles, Methods, Equipment and Applications, Second Edition. CRC Press, 2002.
- [77] I. Utke, P. Hoffmann, and J. Melngailis, “Gas-assisted focused electron beam and ion beam processing and fabrication,” Journal of Vacuum Science & Technology B: Microelectronics and Nanometer Structures, vol. 26, no. 4, p. 1197, 2008.
- [78] W. F. v. Dorp and C. W. Hagen, “A critical literature review of focused electron beam induced deposition,” Journal of Applied Physics, vol. 104, no. 8, p. 081301, 2008.
- [79] A. D. Dubner, A. Wagner, J. Melngailis, and C. V. Thompson, “The role of the ion-solid interaction in ion-beam-induced deposition of gold,” Journal of Applied Physics, vol. 70, no. 2, pp. 665–673, 1991.
- [80] A. Fernández-Pacheco, J. M. D. Teresa, R. Córdoba, and M. R. Ibarra, “Metal-insulator transition in Pt-C nanowires grown by focused-ion-beam-induced deposition,” Physical Review B, vol. 79, no. 17, p. 174204, 2009.
- [81] J. D. Fowlkes, R. Winkler, B. B. Lewis, A. Fernández-Pacheco, L. Skoric, D. Sanz-Hernández, M. G. Stanford, E. Mutunga, P. D. Rack, and H. Plank, “High-Fidelity 3D-Nanoprinting via Focused Electron Beams: Computer-Aided Design (3BID),” ACS Applied Nano Materials, vol. 1, no. 3, pp. 1028–1041, 2018.
- [82] D. Sanz-Hernández and A. Fernández-Pacheco, “Modelling focused electron beam induced deposition beyond Langmuir adsorption,” Beilstein Journal of Nanotechnology, vol. 8, no. 1, pp. 2151–2161, 2017.
- [83] M. Tanase, D. M. Silevitch, C. L. Chien, and D. H. Reich, “Magnetotransport properties of bent ferromagnetic nanowires,” Journal of Applied Physics, vol. 93, no. 10, pp. 7616–7618, 2003.
- [84] C.-Y. You and S.-C. Shin, “Generalized analytic formulae for magneto-optical Kerr effects,” Journal of Applied Physics, vol. 84, no. 1, pp. 541–546, 1998.
- [85] S. Yamamoto and I. Matsuda, “Measurement of the Resonant Magneto-Optical Kerr Effect Using a Free Electron Laser,” Applied Sciences, vol. 7, no. 7, p. 662, 2017.
- [86] D. A. Allwood, G. Xiong, M. D. Cooke, and R. P. Cowburn, “Magneto-optical Kerr effect analysis of magnetic nanostructures,” Journal of Physics D: Applied Physics, vol. 36, no. 18, p. 2175, 2003.
- [87] A. Fernández-Pacheco, N.-J. Steinke, D. Mahendru, A. Welbourne, R. Mansell, S. L. Chin, D. Petit, J. Lee, R. Dalgliesh, S. Langridge, et al., “Magnetic state of multilayered synthetic antiferromagnets during soliton nucleation and propagation for vertical data transfer,” Advanced Materials Interfaces, vol. 3, no. 15, p. 1600097, 2016.

- [88] J. Fernandez-Roldan, Y. Ivanov, and O. Chubykalo-Fesenko, "Magnetic Nano- and Microwires," pp. 403–426, 2020.
- [89] P. R. Soledade, J. Brandão, A. Mello, and L. C. Sampaio, "Enhanced magnetoresistance and pinning–depinning processes of vortex domain walls in ferromagnetic nanowires," *Materials Research Express*, vol. 4, no. 2, p. 025034, 2017.
- [90] L. Piraux, K. Renard, R. Guillemet, S. Mátéfi-Tempfli, M. Mátéfi-Tempfli, V. A. Antohe, S. Fusil, K. Bouzehouane, and V. Cros, "Template-Grown NiFe/Cu/NiFe Nanowires for Spin Transfer Devices," *Nano Letters*, vol. 7, no. 9, pp. 2563–2567, 2007.
- [91] L. Hirt, A. Reiser, R. Spolenak, and T. Zambelli, "Additive Manufacturing of Metal Structures at the Micrometer Scale," *Advanced Materials*, vol. 29, no. 17, p. 1604211, 2017.
- [92] H. Plank, R. Winkler, C. H. Schwalb, J. Hütner, J. D. Fowlkes, P. D. Rack, I. Utke, and M. Huth, "Focused Electron Beam-Based 3D Nanoprinting for Scanning Probe Microscopy: A Review," *Micromachines*, vol. 11, no. 1, p. 48, 2019.
- [93] M. Huth, F. Porriati, C. Schwalb, M. Winhold, R. Sachser, M. Dukic, J. Adams, and G. Fantner, "Focused electron beam induced deposition: A perspective," *Beilstein Journal of Nanotechnology*, vol. 3, no. 1, pp. 597–619, 2012.
- [94] T. Ono, H. Miyajima, K. Shigeto, K. Mibu, N. Hosoi, and T. Shinjo, "Propagation of a Magnetic Domain Wall in a Submicrometer Magnetic Wire," *Science*, vol. 284, no. 5413, pp. 468–470, 1999.
- [95] V. Gopal, E. A. Stach, V. R. Radmilovic, and I. A. Mowat, "Metal delocalization and surface decoration in direct-write nanolithography by electron beam induced deposition," *Applied Physics Letters*, vol. 85, no. 1, pp. 49–51, 2004.
- [96] L. Reimer and S. E. Microscopy, "Physics of image formation and microanalysis," *Springer*, vol. 45, p. 135, 1985.
- [97] R. Winkler, J. Fowlkes, A. Szkudlarek, I. Utke, P. D. Rack, and H. Plank, "The Nanoscale Implications of a Molecular Gas Beam during Electron Beam Induced Deposition," *ACS Applied Materials & Interfaces*, vol. 6, no. 4, pp. 2987–2995, 2014.
- [98] W. Gil, D. Görlitz, M. Horisberger, and J. Kötzler, "Magnetoresistance anisotropy of polycrystalline cobalt films: Geometrical-size and domain effects," *Physical Review B*, vol. 72, no. 13, p. 134401, 2005.
- [99] Y. M. Lau, P. C. Chee, J. T. L. Thong, and V. Ng, "Properties and applications of cobalt-based material produced by electron-beam-induced deposition," *Journal of Vacuum Science & Technology A: Vacuum, Surfaces, and Films*, vol. 20, no. 4, pp. 1295–1302, 2002.
- [100] G. Bertotti and G. Bertotti, "Chapter 3 - Maxwell's Equations in Magnetic Media," *Electromagnetism*, pp. 73–102, San Diego: Academic Press, 01 1998.

- [101] E. Mutunga, R. Winkler, J. Sattelkow, P. D. Rack, H. Plank, and J. D. Fowlkes, "Impact of Electron-Beam Heating during 3D Nanoprinting," *ACS Nano*, vol. 13, no. 5, pp. 5198–5213, 2019.
- [102] M. V. P. d. Santos, M. Velo, R. D. Domingos, Y. Zhang, X. Maeder, C. Guerra-Nunez, J. P. Best, F. Béron, K. R. Pirota, S. A. Moshkalev, J. A. Diniz, and I. Utke, "Annealing-based electrical tuning of cobalt-carbon deposits grown by focused-electron-beam-induced deposition," *ACS Applied Materials & Interfaces*, 2016.
- [103] J. Pablo-Navarro, C. Magén, and J. M. d. Teresa, "Purified and Crystalline Three-Dimensional Electron-Beam-Induced Deposits: The Successful Case of Cobalt for High-Performance Magnetic Nanowires," *ACS Applied Nano Materials*, vol. 1, no. 1, pp. 38–46, 2017.
- [104] G. J. v. Gorp, "Resistivity, grain size, and structure of vacuum-deposited Co films," *Journal of Applied Physics*, vol. 46, no. 5, pp. 1922–1927, 1975.
- [105] A. K. Pal, S. Chaudhuri, and A. K. Barua, "The electrical resistivity and temperature coefficient of resistivity of cobalt films," *Journal of Physics D: Applied Physics*, vol. 9, no. 15, pp. 2261–2267, 1976.
- [106] J. D. Vries, "Temperature and thickness dependence of the resistivity of thin polycrystalline aluminium, cobalt, nickel, palladium, silver and gold films," *Thin Solid Films*, vol. 167, no. 1-2, pp. 25–32, 1988.
- [107] H. Plank, D. A. Smith, T. Haber, P. D. Rack, and F. Hofer, "Fundamental Proximity Effects in Focused Electron Beam Induced Deposition," *ACS Nano*, vol. 6, no. 1, pp. 286–294, 2011.
- [108] E. Nikulina, O. Idigoras, J. M. Porro, P. Vavassori, A. Chuvilin, and A. Berger, "Origin and control of magnetic exchange coupling in between focused electron beam deposited cobalt nanostructures," *Applied Physics Letters*, vol. 103, no. 12, p. 123112, 2013.
- [109] G. Boero, I. Utke, T. Bret, N. Quack, M. Todorova, S. Mouaziz, P. Kejik, J. Brugger, R. S. Popovic, and P. Hoffmann, "Submicrometer Hall devices fabricated by focused electron-beam-induced deposition," *Applied Physics Letters*, vol. 86, no. 4, p. 042503, 2005.
- [110] P. Sergelius, J. M. M. Moreno, M. Waleczek, T. Böhnert, D. Görlitz, and K. Nielsch, "Magnon contribution to the magnetoresistance of iron nanowires deposited using pulsed electrodeposition," *physica status solidi (RRL) - Rapid Research Letters*, vol. 9, no. 4, pp. 255–258, 2015.
- [111] C. Donnelly, M. Guizar-Sicairos, V. Scagnoli, S. Gliga, M. Holler, J. Raabe, and L. J. Heyderman, "Three-dimensional magnetization structures revealed with X-ray vector nanotomography," *Nature*, vol. 547, no. 7663, p. 328, 2017.
- [112] D. Ruffer, R. Huber, P. Berberich, S. Albert, E. Russo-Averchi, M. Heiss, J. Arbiol, A. F. i. Morral, and D. Grundler, "Magnetic states of an individual Ni nanotube probed by anisotropic magnetoresistance," *Nanoscale*, vol. 4, no. 16, pp. 4989–4995, 2012.

- [113] D. P. Weber, D. Ruffer, A. Buchter, F. Xue, E. Russo-Averchi, R. Huber, P. Berberich, J. Arbiol, A. F. i. Morral, D. Grundler, and M. Poggio, “Cantilever Magnetometry of Individual Ni Nanotubes,” *Nano Letters*, vol. 12, no. 12, pp. 6139–6144, 2012.
- [114] M. Vázquez, *Magnetic nano-and microwires: design, synthesis, properties and applications*. Woodhead Publishing, 2015.
- [115] P. Bouquin, J.-V. Kim, O. Bultynck, S. Rao, S. Couet, G. S. Kar, and T. Devolder, “Stochastic Processes in Magnetization Reversal Involving Domain-Wall Motion in Magnetic Memory Elements,” *Physical Review Applied*, vol. 15, no. 2, p. 024037, 2021.
- [116] M. Muñoz and J. L. Prieto, “Suppression of the intrinsic stochastic pinning of domain walls in magnetic nanostripes,” *Nature Communications*, vol. 2, no. 1, p. 562, 2011.
- [117] J. P. Attané, D. Ravelosona, A. Marty, Y. Samson, and C. Chappert, “Thermally activated depinning of a narrow domain wall from a single defect,” *Phys. Rev. Lett.*, vol. 96, p. 147204, Apr 2006.
- [118] C. Bran, E. Saugar, J. A. Fernandez-Roldan, R. P. d. Real, A. Asenjo, L. Aballe, M. Foerster, A. F. Rodríguez, E. M. Palmero, M. Vazquez, and O. Chubykalo-Fesenko, “Stochastic vs. deterministic magnetic coding in designed cylindrical nanowires for 3D magnetic networks,” *Nanoscale*, vol. 13, no. 29, pp. 12587–12593, 2021.
- [119] E. Muñoz-Sandoval, J. J. Torres-Heredia, and F. López-Urías, “Micromagnetic simulations of hysteresis loops in ferromagnetic Reuleaux’s triangles,” *Journal of Applied Physics*, vol. 97, no. 10, p. 10E318, 2005.
- [120] A. Fernández-Pacheco, J. M. D. Teresa, A. Szkudlarek, R. Córdoba, M. R. Ibarra, D. Petit, L. O’Brien, H. T. Zeng, E. R. Lewis, D. E. Read, and R. P. Cowburn, “Magnetization reversal in individual cobalt micro- and nanowires grown by focused-electron-beam-induced-deposition,” *Nanotechnology*, vol. 20, no. 47, p. 475704, 2009.
- [121] Y. P. Ivanov, M. Vázquez, and O. Chubykalo-Fesenko, “Magnetic reversal modes in cylindrical nanowires,” *Journal of Physics D: Applied Physics*, vol. 46, no. 48, p. 485001, 2013.
- [122] C. Donnelly, K. L. Metlov, V. Scagnoli, M. Guizar-Sicairos, M. Holler, N. S. Bingham, J. Raabe, L. J. Heyderman, N. R. Cooper, and S. Gliga, “Experimental observation of vortex rings in a bulk magnet,” *Nature Physics*, vol. 17, no. 3, pp. 316–321, 2021.
- [123] C. A. Ross, M. Hwang, M. Shima, J. Y. Cheng, M. Farhoud, T. A. Savas, H. I. Smith, W. Schwarzacher, F. M. Ross, M. Redjal, and F. B. Humphrey, “Micromagnetic behavior of electrodeposited cylinder arrays,” *Physical Review B*, vol. 65, no. 14, p. 144417, 2002.
- [124] Y. P. Ivanov, A. Chuvilin, L. G. Vivas, J. Kosel, O. Chubykalo-Fesenko, and M. Vázquez, “Single crystalline cylindrical nanowires – toward dense 3D arrays of magnetic vortices,” *Scientific Reports*, vol. 6, no. 1, p. 23844, 2016.

- [125] H. Mohammed, E. V. Vidal, Y. P. Ivanov, and J. Kosel, "Magnetotransport Measurements of Domain Wall Propagation in Individual Multisegmented Cylindrical Nanowires," IEEE Transactions on Magnetism, vol. 52, no. 7, pp. 1–5, 2016.
- [126] A. Hirohata, K. Yamada, Y. Nakatani, L. Prejbeanu, B. Diény, P. Pirro, and B. Hillebrands, "Review on spintronics: Principles and device applications," Journal of Magnetism and Magnetic Materials, vol. 509, p. 166711, 2020.
- [127] S. Iihama, S. Mizukami, H. Naganuma, M. Oogane, Y. Ando, and T. Miyazaki, "Gilbert damping constants of Ta/CoFeB/MgO(Ta) thin films measured by optical detection of precessional magnetization dynamics," Physical Review B, vol. 89, no. 17, p. 174416, 2014.
- [128] S. Ikeda, K. Miura, H. Yamamoto, K. Mizunuma, H. D. Gan, M. Endo, S. Kanai, J. Hayakawa, F. Matsukura, and H. Ohno, "A perpendicular-anisotropy CoFeB–MgO magnetic tunnel junction," Nature Materials, vol. 9, no. 9, pp. 721–724, 2010.
- [129] F. Meng, C. Donnelly, L. Skoric, A. Hierro-Rodriguez, J.-w. Liao, and A. Fernández-Pacheco, "Fabrication of a 3D Nanomagnetic Circuit with Multi-Layered Materials for Applications in Spintronics," Micromachines, vol. 12, no. 8, p. 859, 2021.
- [130] A. Aziz, S. J. Bending, H. Roberts, S. Crampin, P. J. Heard, and C. H. Marrows, "Artificial domain structures realized by local gallium focused Ion-beam modification of Pt-Co-Pt trilayer transport structure," Journal of Applied Physics, vol. 98, no. 12, p. 124102, 2005.
- [131] K. Wasa and T. Matsushima, "Handbook of Sputtering Technology (Second Edition)," Part III: Sputtering Technology for Nanomaterials and Thin Film MEMS, pp. 597–622, 2012.
- [132] D. Sanz-Hernández, R. F. Hamans, J. Osterrieth, J.-W. Liao, L. Skoric, J. D. Fowlkes, P. D. Rack, A. Lippert, S. F. Lee, R. Lavrijsen, and A. Fernández-Pacheco, "Fabrication of Scaffold-Based 3D Magnetic Nanowires for Domain Wall Applications," Nanomaterials, vol. 8, no. 7, p. 483, 2018.
- [133] J. Teixeira, R. A. Silva, J. Ventura, A. Pereira, F. Carpinteiro, J. Araújo, J. Sousa, S. Cardoso, R. Ferreira, and P. Freitas, "Domain imaging, MOKE and magnetoresistance studies of CoFeB films for MRAM applications," Materials Science and Engineering: B, vol. 126, no. 2-3, pp. 180–186, 2006.
- [134] X. Qiao, B. Wang, Z. Tang, Y. Shen, H. Yang, J. Wang, Q. Zhan, S. Mao, X. Xu, and R.-W. Li, "Tuning magnetic anisotropy of amorphous CoFeB film by depositing on convex flexible substrates," AIP Advances, vol. 6, no. 5, p. 056106, 2016.
- [135] J. S. Agustsson, U. B. Arnalds, A. S. Ingason, K. B. Gylfason, K. Johnsen, S. Olafsson, and J. T. Gudmundsson, "Electrical resistivity and morphology of ultra thin Pt films grown by dc magnetron sputtering on SiO<sub>2</sub>," Journal of Physics: Conference Series, vol. 100, no. 8, p. 082006, 2008.

- [136] X. Sun, J. Huang, J. Jian, M. Fan, H. Wang, Q. Li, J. L. M. Manus-Driscoll, P. Lu, X. Zhang, and H. Wang, “Three-dimensional strain engineering in epitaxial vertically aligned nanocomposite thin films with tunable magnetotransport properties,” Materials Horizons, vol. 5, no. 3, pp. 536–544, 2018.
- [137] O. A. Tretiakov, M. Morini, S. Vasylykevych, and V. Slastikov, “Engineering Curvature-Induced Anisotropy in Thin Ferromagnetic Films,” Physical Review Letters, vol. 119, no. 7, p. 077203, 2017.
- [138] A. Sidhwa, C. Spinner, T. Gandy, M. Goulding, W. Brown, H. Naseem, R. Ulrich, S. Ang, S. Charlton, V. Prasad, and T. Cale, “Study of the Step Coverage and Contact Resistance by Using Two-Step TiN Barrier and Evolve Simulation,” IEEE Transactions on Semiconductor Manufacturing, vol. 18, no. 1, pp. 163–173, 2005.